STUDIES ON LOW-ENERGY, MASS-SEPARATED ION BEAM DEPOSITION AND REACTIVE ION BEAM ETCHING

September 1981

KIYOSHI MIYAKE

STUDIES ON LOW-ENERGY, MASS-SEPARATED ION BEAM DEPOSITION AND REACTIVE ION BEAM ETCHING

September 1981

Kiyoshi MIYAKE

Contents

Chapter 2 A LOW-ENERGY, MASS-SEPARATED ION BEAM DEPOSITION AND ETCHING SYSTEM

Chapter 3 ION BEAM DEPOSITION

Chapter 4 REACTIVE ION BEAM ETCHING

Preface

The idea of using low-energy, metal ions for film formation has been proposed for many years ago. For example, in 1961 Flynt proposed their use for electronic component fabrication. However, little systematic study was done in the 1960s. It wasn't until 1971 that Aisenberg and Chabot showed that diamond-like carbon films could be formed by ion beam deposition. Moreover, other methods, such as "ion plating" (Mattox(1963), Murayama(1975), Teer(1978), and so on) and "ionized cluster beam deposition" (Takagi(1972)) were being intensively studied by many researchers. The use of these ionized beam or plasma methods led to dramatic improvements in film qualities.

For further controllability of deposition and fundamental studies on film growth mechanism, mass-analysed ion beam deposition has been investigated by the author and many other researchers. Epitaxial growth of Si, Ge , or Ag films at relatively low-temperature (< 800°C) has recently been reported.

The use of chemically reactive plasma, called plasma etching in semiconductor microfabrications has also been developed by many researchers. At present, this technique is thought to be one of the essential technologies for VLSI fabrication. In plasma etching, the effects of ion bombardment are thought to enhance the surface chemical reactions. However, the mechanism for these enhancement effects has not yet been fully understood.

Recently, many people have begun to relate plasma discharge conditions to the properties of the deposited films, or etching properties. However, the phenomena occuring in a plasma or on a depositing surface are so complicated that there are yet many unresolved, cross-contradictory facts.

In both deposition and etching, the interaction of low-energy ion beams with solid surfaces becomes the basis for the interpretation of these complicated phenomena.

The purpose of this thesis is to investigate the fundamental effects of ion bombardment on ion beam deposition and etching. This thesis also describes the development of a low-energy, high-current ion beam accelerator used in the experiments necessary for the thesis.

The concepts obtained in developing the present experimental equipment and in the investigations of ion beam deposition and etching mechanisms can be applied to similar studies in other fields, such as plasma wall interaction in fusion reactors, or surface chemical reactions, including oxidation, nitridation, sulfuration and carbonization, in an activated plasma.

With future development of finely focused ion beam technologies, maskless ion beam deposition or etching methods, which have long been many people's dreams, should become possible.

Acknowledgements

The author wishes to express his sincere appreciation to Professor Toshinori Takagi of Kyoto University for his invaluable adivice and encouragement throughout this work. He also wishes to thank Professors Rhyohei Itatani and Akira Kawabata of Kyoto University for their stimulating discussions. In addition, he wishes to thank his supervisor, Dr. Takashi Tokuyama and his manager, Dr. Kikuji Satoh, for their thoughtful advice and continuing encouragement during the present research.

Grateful thanks are also due to Dr. Kunihiro Yagi, Dr. Shin'ichi Tachi and Shozo Tamura for their co-operation and stimulating discussions and criticisms in accomplishing this work; and to Assistant Professors Isao Yamada, and Kakuei Matsubara of Kyoto University and Professor Kumetaro Kaneko (INS, University of Tokyo) for their fruitful discussions on thin film formation and ion beam physics.

It is a pleasure to thank Drs. Fumio Nagata, Eisuke Mitani and Hiroshi Kakibayashi (Analytical Center, Hitachi CRL) for their technical assistance in SIMS and RHEED measurements. Finally, the author wish to thank to Dr. Masao Tamura and Nobuyoshi Natsuaki for their valuable discussions on radiation effects in solids and thin film formation mechanisms.

List of figures

Chapter 2

Chapter 3

Chapter 4

List of tables

Chapter 3

Chapter 1 INTRODUCTION

Thin film formation is becoming one of the key technologies for the fabrication of electronic and optical devices. Such topics as the precise control of stoichiometry and deposition parameters and improvement of film qualities have been invesitigated for many years[1].

Conventional high temperature chemical reaction techniques are not essentially suitable for such highly precise applications, and new techniques of a more physical nature are being widely investigated. Among these physical deposition techniques, those using ions have attracted the increasing interest of many investigators[2,3]. When some ion content is included in vacuum evaporation or sputtered particle deposition process, remarkable improvements in the qualities of the deposited film have been reported[4,5].

The simultaneous irradiation of vacuum-deposited germanium films by Ar^+ ions reported by Hirsh and Varga [6] has demonstrated dramatic film quality improvement compared to conventional vacuum evaporated films. Since argon is not a constituent element in the germanium lattice, some kinetic effects from the accelerated argon ions are presumed to be involved in this improvement of the film qualities and film/substrate interface properties.

This process, in which ionized and neutral constituent elements are simultaneously depositied, is generally called ion plating[7]. Many reports have indicated improvements in the quality of various films, whereas few papers have tried to elucidate the effects ions have on film qualities.

Dry etching is another key technology for VLSI (Very Large Scale Integration) fabrication. Conventional wet chemical etching using a liquid solution is inadequate for obtaining finely patterned profiles of about 1 μm because of excessive undercutting[8]. Therefore, etching methods which make use of chemically activated species generated in a plasma have been developed[9,10]. This technique is now being called "dry etching" or "plasma etching".

This thesis investigates both film formation and etching to determine the effects ions have on these techniques.

The structure of the thesis is as follows: The experimental apparatus is described in considerable detail in Chapter 2. It contains some special features which were designed especialy for this work. Two sub-sections are devoted to the ion source characteristics and to the ion deceleration method.

In Chapter 3, ion beam deposition is investigated in detail. Several effects relating to ion beam deposition are discussed with stress on ion induced atomic mixing and sputtering and implantation effects.

Chapter 4 is devoted to a plasma etching mechanism study by using the mass-separated ion beam system described in Chapter 2. Special emphasis is placed on the individual roles of physical and chemical sputtering in Si etching.

Chapter 2

A LOW-ENERGY, MASS-SEPARATED ION BEAM DEPOSITION AND ETCHING SYSTEM

2.1 Introduction

The "low-energy ion accelerator" has drawn increasing interest as a means of studying low energy ion beam interactions with solid surfaces, such as material build up phenomena, or plasma chemical etching reactions, etc. However, there are few reports on successful techniques to obtain high-current ion beams at an extremely low energy (1 ~ 1000 eV) level.

Several low energy ion accelerators have been reported as experimental equipment for use in ion-molecule reaction studies. Well-collimated, small-energy-spread ion beams are required for those purposes. The multi-lens type ion deceleration method developed by E. Lindholm[1] has been commonly used. However, this type of accelerator seems to be unsuitable for our purposes because of the limited ion current ($< 1\ \mu A$).

Simple deceleration methods have been described in experiments on isotope separation by A. Fontell[2], K. Chida[3], T. Tortschanoff[4], etc.. This approach seems more suitable for the present purposes.

Several types of mass-separated, low-energy ion accelerators have been developed by K. Yagi[5], J.H. Freeman[6], K. Miyake[7], J. Amano[8], J.S. Colligon[9], T. Tsukizoe[10], G.E. Thomas[11], I. Yamada[12], etc.. In this chapter, a high current, low-energy ion beam system developed by the author will be discribed in detail. Section 2.2 discusses a few fundamental concepts for the design of a high-current, low-energy ion accelerator. In section 2.3 the features of the equipment used throughout this work are presented. Then, the ion source and the ion deceleration lens system are discussed in more detail in sections 2.4 and 2.5. Section 2.6 draws several conclusions.

2.2 System Design Concepts

2.2.1 Ion current density and vacuum pressure

In an ion beam deposition system, the ion source is usually operated under considerable gas pressure. Therefore, it is necessary to consider the deposition atmosphere. The design of the deposition chamber must satisfy the following condition:

$$S_i \Gamma_i \gg S_n \Gamma_n \qquad (2.1),$$

where Γ_i is the depositing ion beam flux on the target surface and Γ_n is the residual gas atom flux that hit the target surface. Here, S_i and S_n denote the sticking probabilities of deposited ions and of residual gas atoms, respectively. This relationship (2.1) represents the "worst case" criterion, where depositing ions are assumed not to sputter the adsorbed residual gas atoms. The general residual gas concentrations will be lower than those predicted from arrival rate consideration alone. Here Γ_i and Γ_n are expressed as:

$$\Gamma_i = 6.25 \times 10^{12} J_i \ (\mathrm{cm}^{-2}\ \mathrm{s}^{-1}) \qquad ,(2.2),$$

$$\Gamma_n = 5.3 \times 10^{20} P \ (\mathrm{cm}^{-2}\ \mathrm{s}^{-1}) \qquad ,(2.3),$$

where J_i (μA/cm^2) is the ion beam current density impinging the target and P(Torr) is the residual gas pressure in the deposition chamber.

The relations of p and J_i to Γ_i and Γ_n are shown in Fig. 2.1. From that figure it can be seen that, if the deposition is carried out in a 10^{-8} Torr vacuum, an ion beam intensity of at least 100 $\mu A/cm^2$ is necessary when S_i and S_n are of the same order. In this case, contamination effects due to residual gas particles are considered to be negligible since the ion beam flux is about two orders higher than the residual gas atom flux.

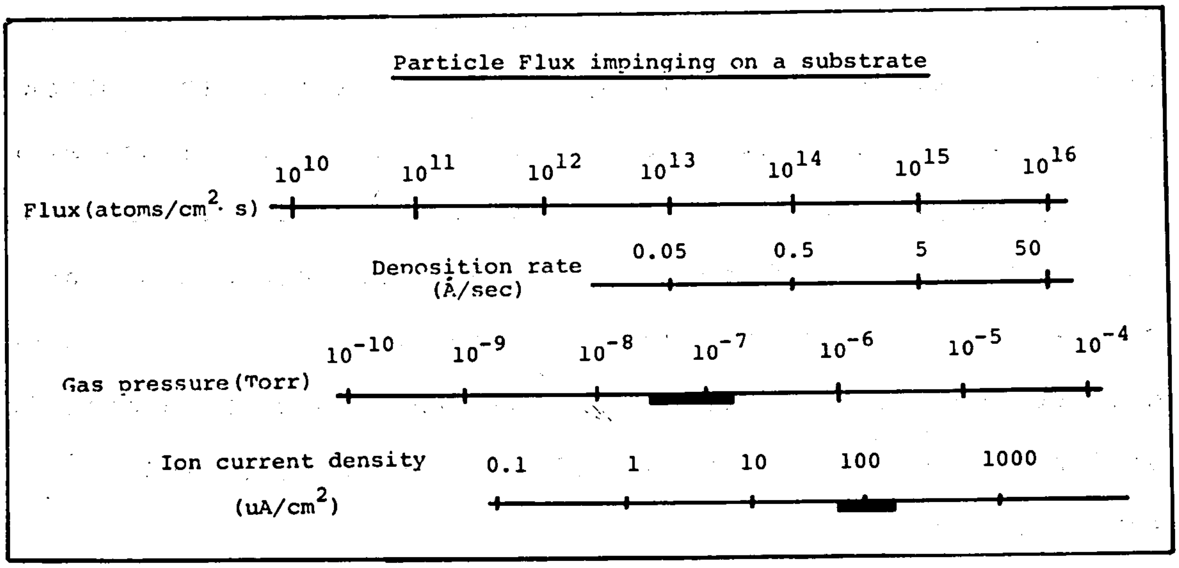

Fig. 2.1 Relationship of pressure and ion current density to ion flux.

The deposition time, T, and dose, D, required for build up in a film of thickness, d, can be calculated from the following:

$$T\ (\mathrm{sec}) = 3.2 \times 10\ \frac{d(\text{Å})}{J_i\ (\mu A/cm^2)}\ , \qquad (2.4)$$

$$D\ (\mathrm{ions/cm^2}) = 2.0 \times 10^{14}\ d(\text{Å}) \qquad (2.5).$$

Here, one monolayer is assumed to have a density of 10^{15} atoms/cm^2 and a thickness of 5 angstroms, assuming the surface to be Si(100) plane. The relationship of dose and thickness to deposition time are shown in Fig. 2.2 with ion current density as a parameter.

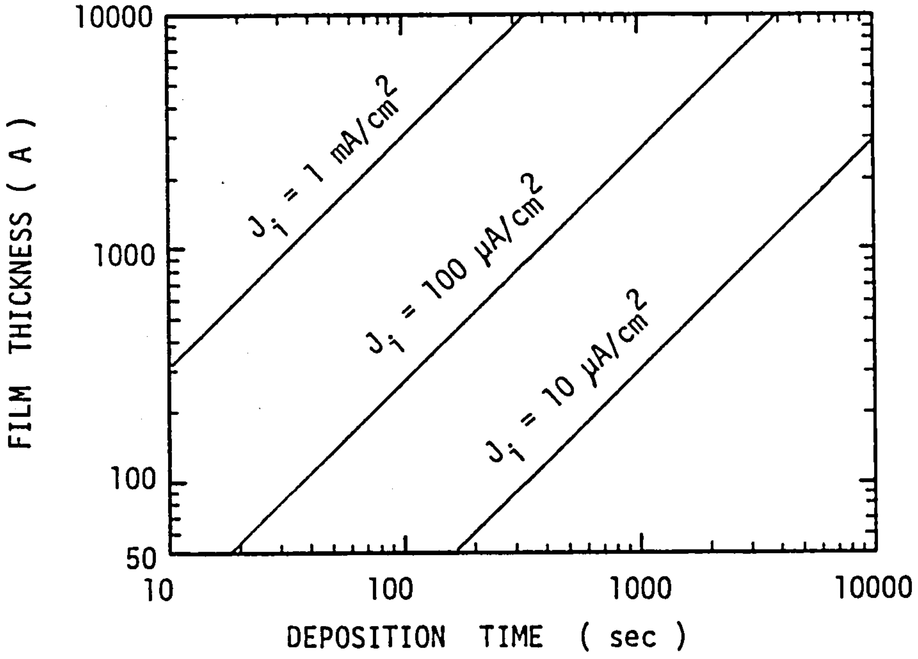

Fig. 2.2 Dependence of film thickness and dose on deposition time.

2.2.2 Ion energy range

Bombardment by energetic metal ions causes the deposition of metal atoms on a solid surface in the low energy region. An increase in energy above the threshold energy causes sputtering of both the substrate and the deposited materials to occur. A further increase in the ion energy causes implantation of ions into the substrate surface. Therefore, the energy range for film growth to occur should be low enough for a self-sputtering yield of less than unity. Typically, 1 to 500 eV is employed for ion beam deposition.

For etching experiments a higher energy (up to 3 keV) ion beam is necessary to simulate the surface phenomena.

Ion bombardment is considered to have several effects on film growth and material etching. Surface cleaning effects due to physical and chemical sputtering are thought to occur. The surface chemical reaction is also thought to be enhanced by the atom migration due to ion bombardment. Defects produced by ion bombardment become nucleation centers for crystal growth. Figure 2.3 summarizes these probable effects of ion bombardment during ion beam deposition and etching.

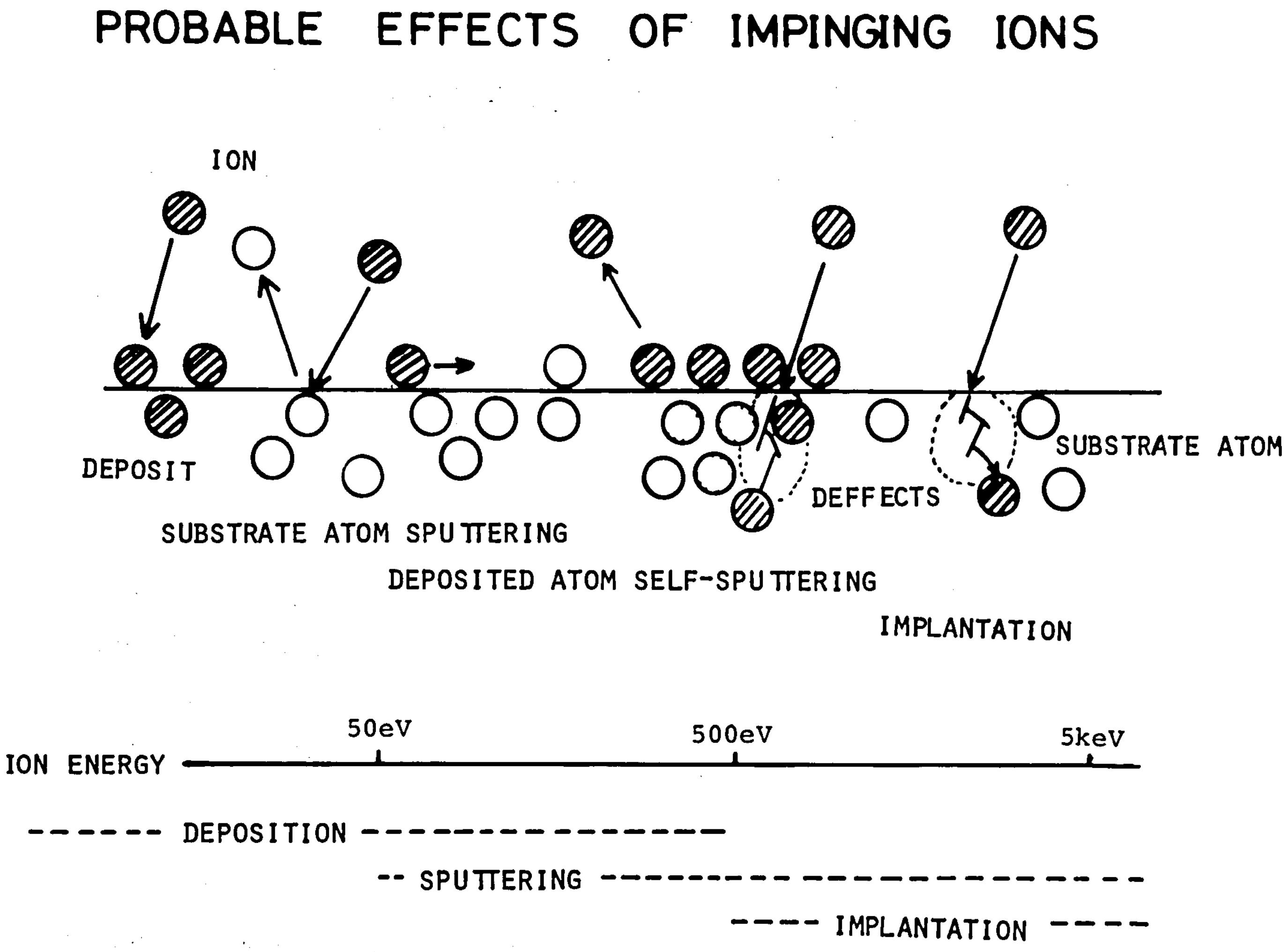

Fig. 2.3 Roles of ion bombardment on thin film formation and etching processes.

2.2.3 Space charge effect on ion beam transport

The charges within an unneutralized ion beam create a radial electric field. This force will cause the beam to expand in diameter. Let us evaluate here this space charge force for a solid cylindrical ion beam moving at uniform axial velocity, v_i, as shown in Fig. 2.4.

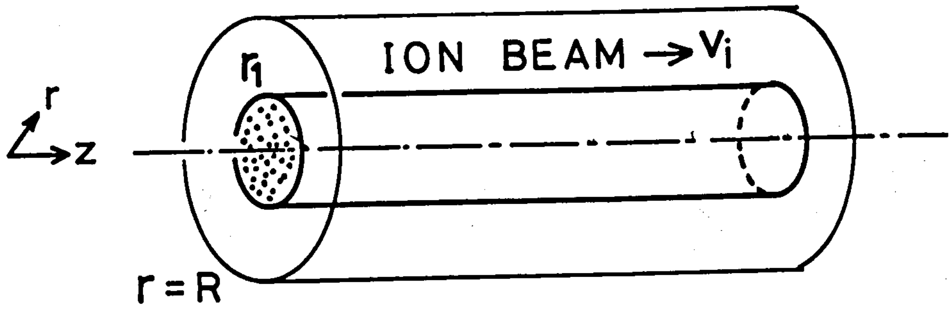

Fig. 2.4 Ion beam in cylindrical coordinate system.

The charges within the beam give rise to an electric field in the radial direction only. This is denoted by E(r). This field can be evaluated using Gauss's law by which it can be shown that the electric field at radius r is proportional to the total electric charges per unit length within the volume bounded by radius r. Here, uniform charge distribution is assumed over the ion beam region ($0 \leqslant r \leqslant r_1$) as shown in Fig. 2.5. The charge density per volume is denoted by ρ . Then, the electric field E(r) and the potential $\phi(r)$ can be calculated as follows:

(i) $0 \leqslant r \leqslant r_1$

$$E(r) = \frac{\rho}{2\varepsilon_0} r, \tag{2.6}$$

$$\phi(r) = \frac{\rho}{4\varepsilon_0} \left\{ 2 r_1^2 \log\left(\frac{R}{r_1}\right) - (r^2 - r_1^2) \right\} \tag{2.7}$$

(ii) $r_1 \leqslant r \leqslant R$

$$E(r) = \frac{\rho r_1^2}{2\varepsilon_0} \frac{1}{r} \tag{2.8}$$

$$\phi(r) = -\frac{\rho r_1^2}{2\varepsilon_0} \log\left(\frac{r}{R}\right) \tag{2.9}$$

Here, it is assumed that the ion beam is laminar along the axis (z-direction) and the beam is located in the center of the grounded drift tube. The charge density ρ can be derived by the equation:

$$\rho = \frac{I_i}{\pi r_1^2 \sqrt{2\eta U}} \tag{2.10}$$

where I_i, η, U denote the ion current, charge to mass ratio of an ion and the kinetic energy of the beam in an axial direction, respectively. The potential distribution is also shown in Fig. 2.5.

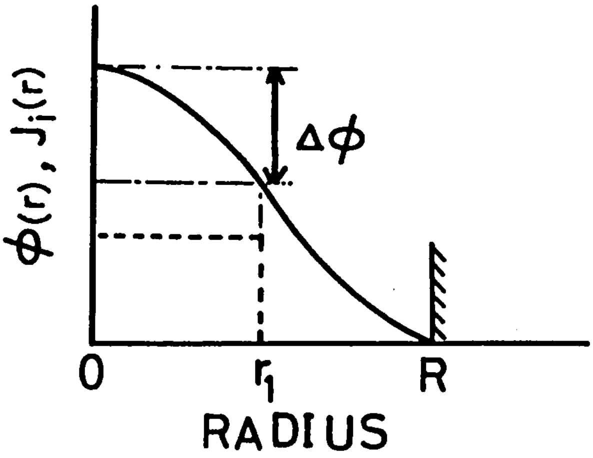

Fig. 2.5 Radial distribution of ion current density and electrical potential.

From Eq. 2.4, the space charge potential $\Delta\phi$, which is defined as the potential difference between $\phi(0)$ and $\phi(r_1)$, can be calculates as:

$$\Delta\phi = \frac{\rho r_1^2}{4\varepsilon_0} = \frac{I_i}{4\pi\varepsilon_0\sqrt{2\eta U}} \tag{2.11}$$

Let us evaluate the beam divergence of the ion beam using an outermost ion trajectory. This assumes that the beam is laminar, i.e. there is no ion cross over. The axial velocity is also assumed to be influenced by space charge potential as a first approxiamation.

The equation of motion for an outer most ion, which has an initial energy U along the axis can be formulated in cylindrical coordinates as,

$$\frac{d^2r}{dt^2} = \frac{\eta I_i}{2\pi\varepsilon_0\sqrt{2\eta U}} \cdot \frac{1}{r} \tag{2.12}$$

$$\frac{d^2z}{dt^2} = 0 \tag{2.13}$$

Let us normalize the variables r and z using the initial beam radius r_1 as

$$y = r/r_1 \quad \text{and} \quad x = z/r_1. \tag{2.14}$$

Then, the equation of motion can be simplified to yield

$$\frac{d^2y}{dx^2} = \frac{\lambda}{y} \tag{2.15}$$

where λ represents the ratio of "radial potential energy due to space charge" to "axial kinetic energy of the ion beam", i.e.,

$$\lambda = \frac{e\Delta\phi}{eU} \tag{2.16}$$

Equation (2.15) can be analytically integrated to yield

$$\sqrt{\frac{\lambda}{2}}\cdot x = \int_0^{\sqrt{\log y}} e^{t^2} dt \tag{2.17}$$

with the initial conditions $y(x=0) = 1$ and $dy/dx\Big]_{x=0} = 0$. The integral on the right side of Eq. (2.16) can be obtained by tabular solution [13]. The final result is shown as a universal trajectory curve with the normalized beam radius r/r_1 and the normalized distance $\sqrt{\frac{\lambda}{2}}\cdot\frac{z}{r_1}$ as variables in Fig. 2.6.

Let us evaluate the beam divergence of an unneutralized ion beam that contain Ar^+ with the initial axial energy U =40 keV and the ion current I_i = 10 mA. Then, the space charge potential $\Delta\phi$ can be calculated from Eq. (2.11) to give $\Delta\phi$ = 200 Volt. In this case, the space charge effect parameter λ is 5×10^{-3}. If the initial beam radius is assumed to be r_1 = 1 cm, the universal curve indicates that the ion beam radius after passing through 100 cm along the axis, would be as large as 30 cm. This result cannot be acceptable for the design of a high-intensity ion beam transport and suggests the necessity for some kind of space charge neutralization of the ion beam.

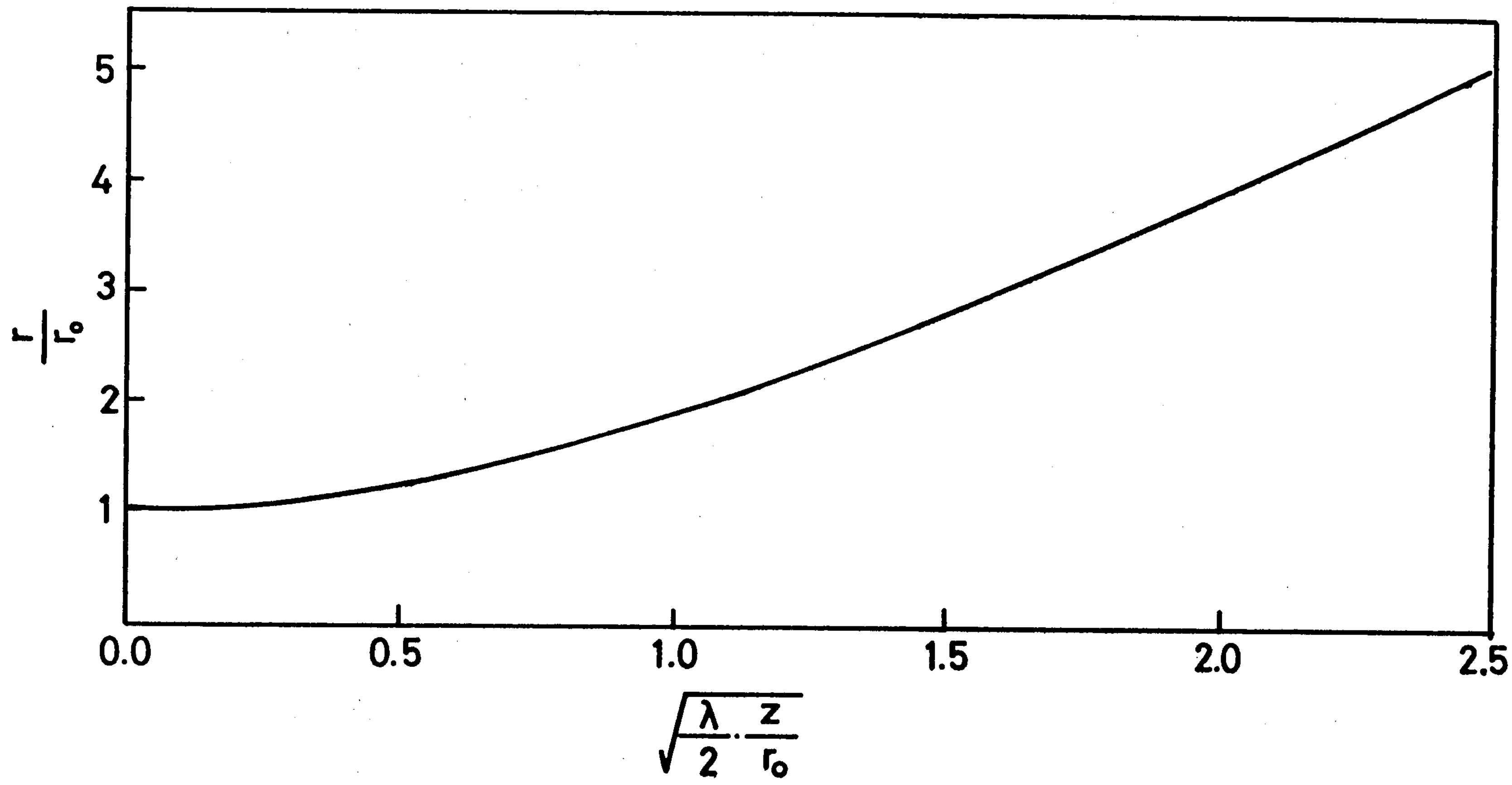

Fig. 2.6 A universal curve representing the outermost ion trajectory.

Next, let us evaluate space charge potential of a neutralized ion beam with electrons according to Gabovich et al.[14]. Let a cylindrical ion beam be space-charge neutralized by an electron gas characterized by electron density n_e and electron temperature kT_e. The ion beam has an axial velocity v_i and is assumed to be moving along the z-axis with beam radius r_1.

Electric potential $\phi(r)$ is determined by Poisson's equation:

$$\frac{1}{r}\frac{d}{dr}\left(r\frac{d\phi}{dr}\right) = -4\pi e(n_i - n_e) \, . \tag{2.18}$$

If uniform distribution of ion density and electron density is assumed, the electric field, E, at the beam boundary ($r = r_1$) can be calculated by integrating Eq. (2.18) as

$$E = -\left.\frac{d\phi}{dr}\right|_{r=r_1} = 2\pi e(n_i - n_e) r_1 \, . \tag{2.19}$$

In a steady state both the electrostatic field and the electron kinetic pressure should be in equilibrium, which can be represented as

$$\frac{E^2}{8\pi} = n_e k T_e \tag{2.20}$$

Equations (2.19) and (2.20) can be combined to yield

$$2\pi e(n_i - n_e) r_1 = \sqrt{8\pi n_e k T_e} \tag{2.21}$$

Since the ion beam current, I_i, is represented as $I_i = \pi r_1^2 \cdot e n_i v_i$, Eq. (2.21) can be transformed into

$$\frac{n_e}{n_i} = 1 - \sqrt{\frac{2kT_e}{e} \cdot \frac{v_i}{I_i} \cdot \frac{n_e}{n_i}} \tag{2.22}$$

Since the electron thermal energy is much smaller than the ion kinetic energy for an intense ion beam, i.e. $\sqrt{\frac{kT_e}{e} \cdot \frac{v_i}{2I_i}} \ll 1$, Eq. (2.22) can be approximated as follows:

$$\frac{n_e}{n_i} \cong 1 - \sqrt{\frac{2kT_e}{e} \cdot \frac{v_i}{I_i}} \tag{2.23}$$

Integrating Eq. (2.16) from r = 0 to the beam boundary $r = r_1$, the space charge potential difference, $\Delta\phi$, between the center of the ion beam and the ion beam boundary can be obtained:

$$\Delta\phi = \pi e r_1^2 \cdot (n_i - n_e) \tag{2.24}$$

Equation (2.22) can be trasformed using Eq. (2.21) to

$$\Delta\phi = \sqrt{\frac{2I_i}{v_i} \cdot \frac{kT_e}{e}} \tag{2.25}$$

This is the final result for space charge potential for an electron neutralized ion beam.

2.2.4 Mass resolution

The mass resolution required for ion beam deposition is not needed to be so high because the inclusion of several isotopes does not affect one metal deposition. Resolution up to $M/\Delta M$ = 100 are sufficient for the deposition of silicon or germanium. For special purposes, it is expected that one single isotopes, such as ^{28}Si or ^{30}Si, will be deposited as "isotope markers".

2.2.5 Contamination effects and the pumping system

It is well known that oil vapor in a vacuum system decomposes and is deposited as an organic film on a solid surface when the surface is subjected to ion or electron particle bombardment. Yagi el al.[5] showed that carboneous films are easily formed on a silicon surface by irradiating 100 eV He^+ ions in an oil diffusion pumped vacuum systen at a pressure of 1×10^{-5} Torr. Therefore, it is necessary to realize an oil-free pumping system and to deposit in an ultra-high vacuum to obtain contamination free films. In-situ observation of the deposited surface or etched quantity measurements are also necessary.

2.3 The Low-Energy, Mass-Separated Ion Beam Deposition and Etching System.

2.3.1 The complete system

Taking the design criteria described in Sec. 2.2 the following low energy accelerator was developed for the experiments of mass-separated ion beam deposition and etching. Fig. 2.7. shows the complete system. The schematic diagram for ion beam transport is shown in Fig. 2.8. The system consists of three major parts: an ion source, a mass-separating magnet, and an ultra-high vacuum (UHV) chamber.

One of the features of this accelerator is that the substrate is held at ground potential. As a result, the major portion of the system, including the beam drift tube, the mass-separation magnet, and the ion beam monitoring controllers, must be floated on a negative potential of 10 to 40 kV. This is quite different from the other IBD systems reported previously[5,6,8,9,10]. Although this potential layout makes ion beam handling quite dangerous, it makes in-situ observation much easier because the substrate can be nearly at the same potential as the measurement controllers. Furthermore, the kinetic energy of the depositing ions can be precisely controlled using a high-precision power supply for ion acceleration.

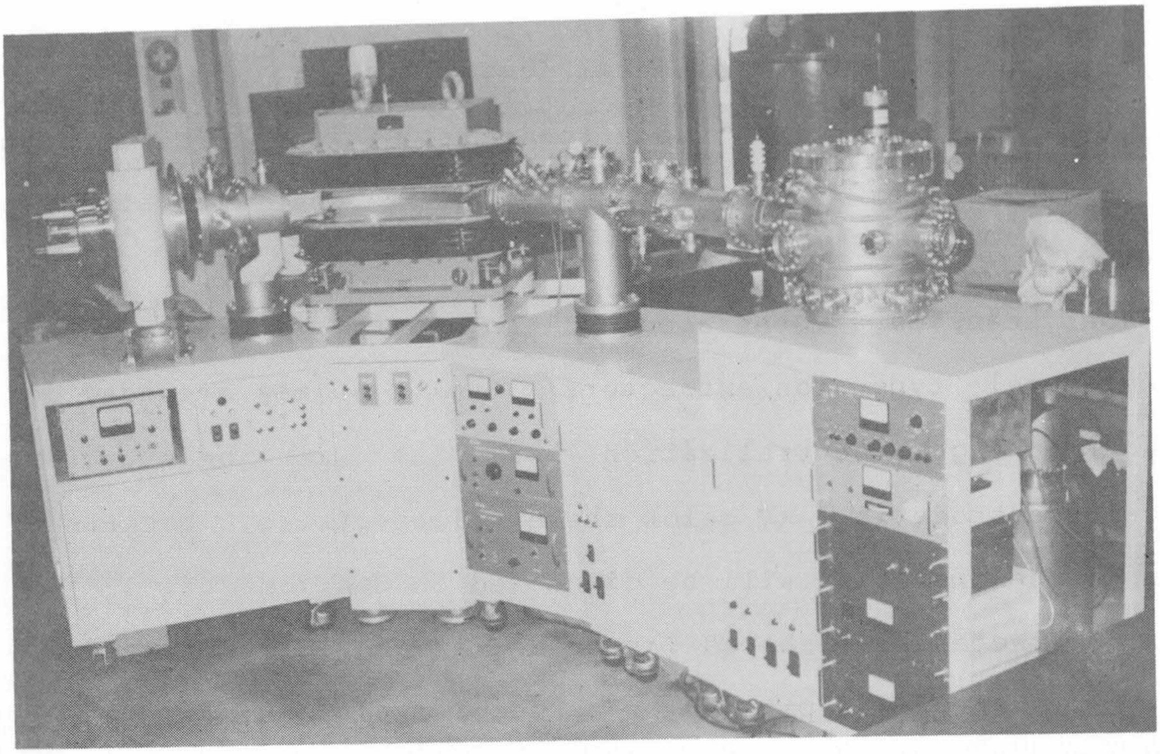

Fig. 2.7 Low-energy, mass-separated ion beam accelerator.

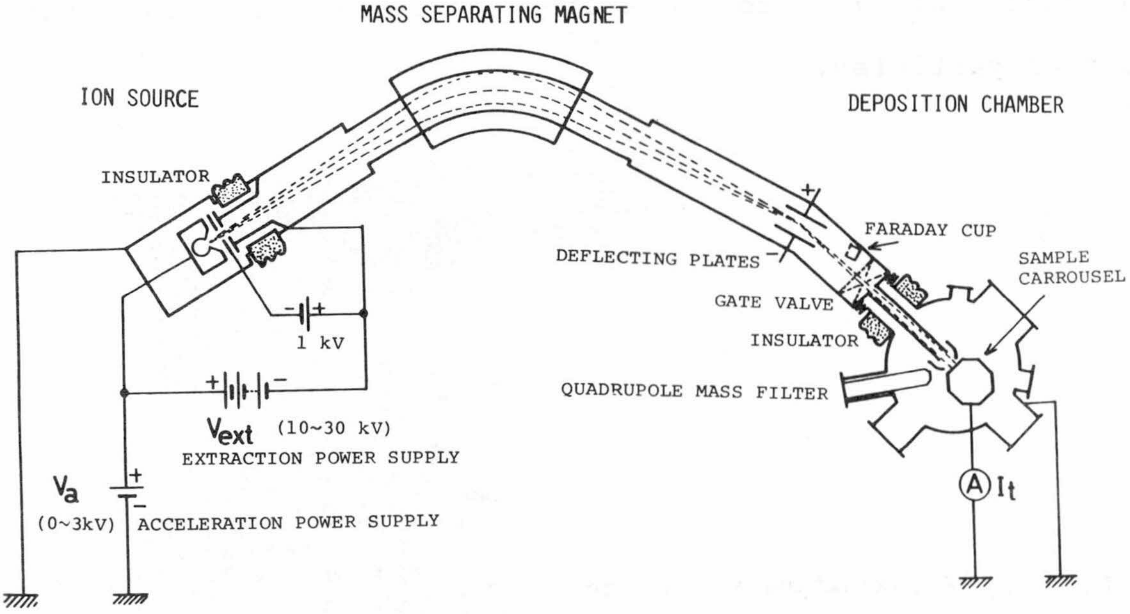

Fig. 2.8 Schematic of a low-energy, mass-separated ion beam accelerator.

For the deposition of metal ions, such as Si or Ge, $SiCl_4$ or $GeCl_4$ gases are fed into a Freeman-type ion source through a variable leak valve. Figure 2.9 shows the fabricated ion source.

Ion beams are generated at an energy of 10 ~ 40 kV. Accel-decel type ion extractors(10 mm x 40 mm) are used for space charge neutralization of the ion beams. The accel-electrode is 1 kV below the decel-electrode. Details of ion source operation will be discussed in Section 2.4.

The rectangular-shaped ion beams, at an ion current of 3 - 10 mA, are mass-separated by a sector type magnet($\theta_D = 60^\circ$, $r_D = 48$ cm, gap length = 40 mm) with rotatable shims. The mass-selected ion beam is horizontally focused by this magnet. At the focal point of the magnet, the ion beam is deflected by an angle of 15° to separate charge exchanged high energy neutral particles.

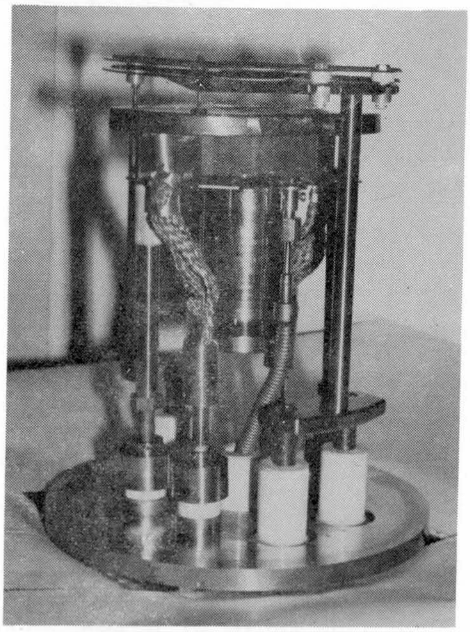

Fig. 2.9 Freeman-type ion source

2.3.2 Space charge neutralization

It is well known that space charge neutralization of an ion beam containing electrons is necessary for the transport of high intensity ion beams[15]. In this apparatus, the effects of space charge neutralization were examined by observing ion beam profiles for the two cases shown in Fig. 2.10. In (a), space charge neutralization becomes deficient because of neutralizing electrons escaping through the periphery of the extractor electrode to the grounded vacuum vessel walls. In (b), the loss of electrons is stopped and the ion beam is fully space-charge neutralized. Figure 2.11 shows the ion current density distributions (horizontal) for these two cases. In (a), the ion density distribution diverges over a region 50 mm wide and the maximum intensity is less than 0.1 mA/cm^2. In (b), the ion beam shows a sharply focused distribution with a beam width of 3 mm and a maximum intensity one order higher than that for (a). Therefore, space charge neutralization is essential for mA-class ion beam transport. In the present study the (b)-type configuration was used.

Although electrostatic lenses, which disturb space charge neutralization, are not suitable for high intensity ion beam transport, electrostatic deflectors (horizontal) are used to cut neutral particles in this system because magnetic deflectors are troublesome to use when different masses of ions are present. The electrostatic deflecting plates are 40 mm W x 80 mm H, with 60 mm spacing. Experimental results show

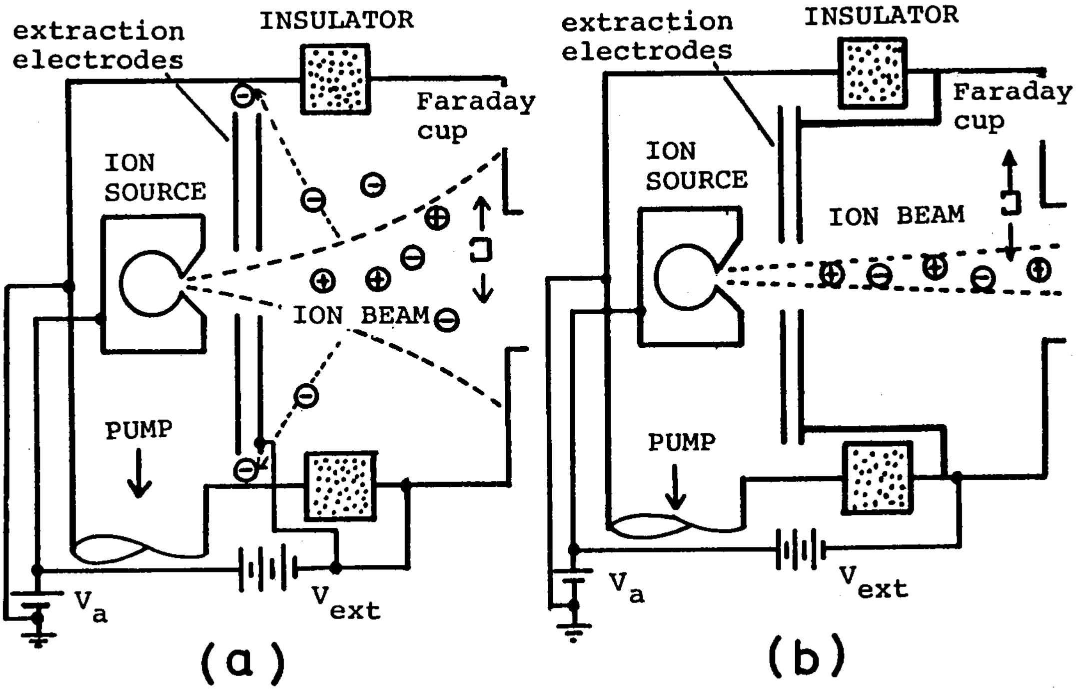

Fig. 2.10 Two ion extraction configurations.

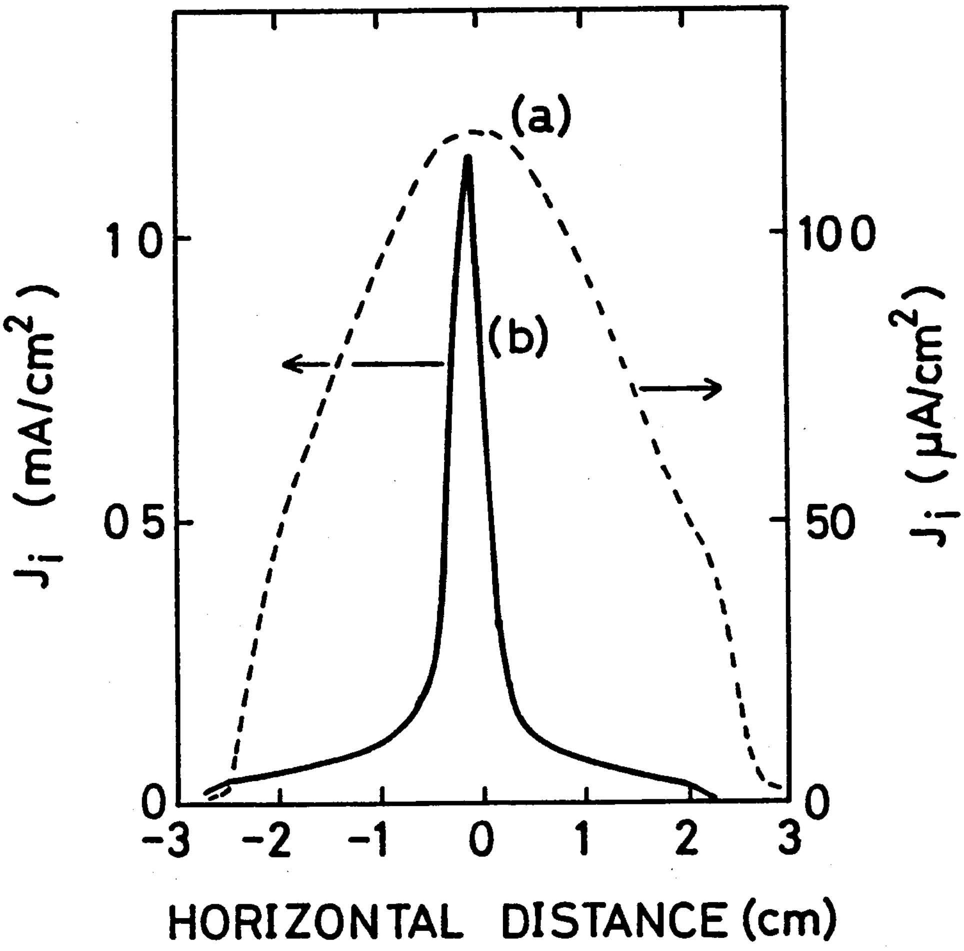

Fig. 2.11 Two ion current density profiles. The dotted curve shows the case partial space charge neutralization. The solid curve shows full space charge neutralization.

that there is no appreciable deformation of the ion beam using this deflection method. This is because few of the ions can hit the largely-spaced electrodes after passing through the collimating slit (10 mm in diameter) in front of the deflectors.

2.3.3 Mass spectra of the ion beams

The mass spectra of extracted ion beams with kinetic energies of 10 - 40 keV were measured. A small Faraday cup with a 3 mm$^{\phi}$ aperture, which is shown in Fig. 2.12, was used to detect the mass spectra. Fig. 2.13 shows the mass spectra for ion beams generated from N_2 and Ar gases. At the focal point of the magnet, ion densities of 100 $\mu A/cm^2$ to 1 mA/cm^2 were obtained.

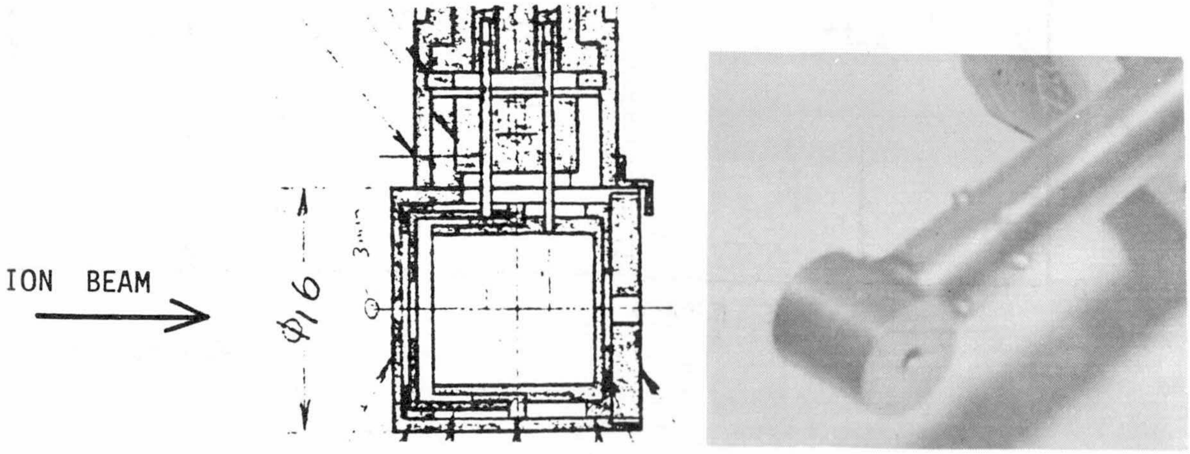

Fig. 2.12 The small Faraday cup used for ion beam profile monitoring. Entrance aperture is 3 mm in diameter.

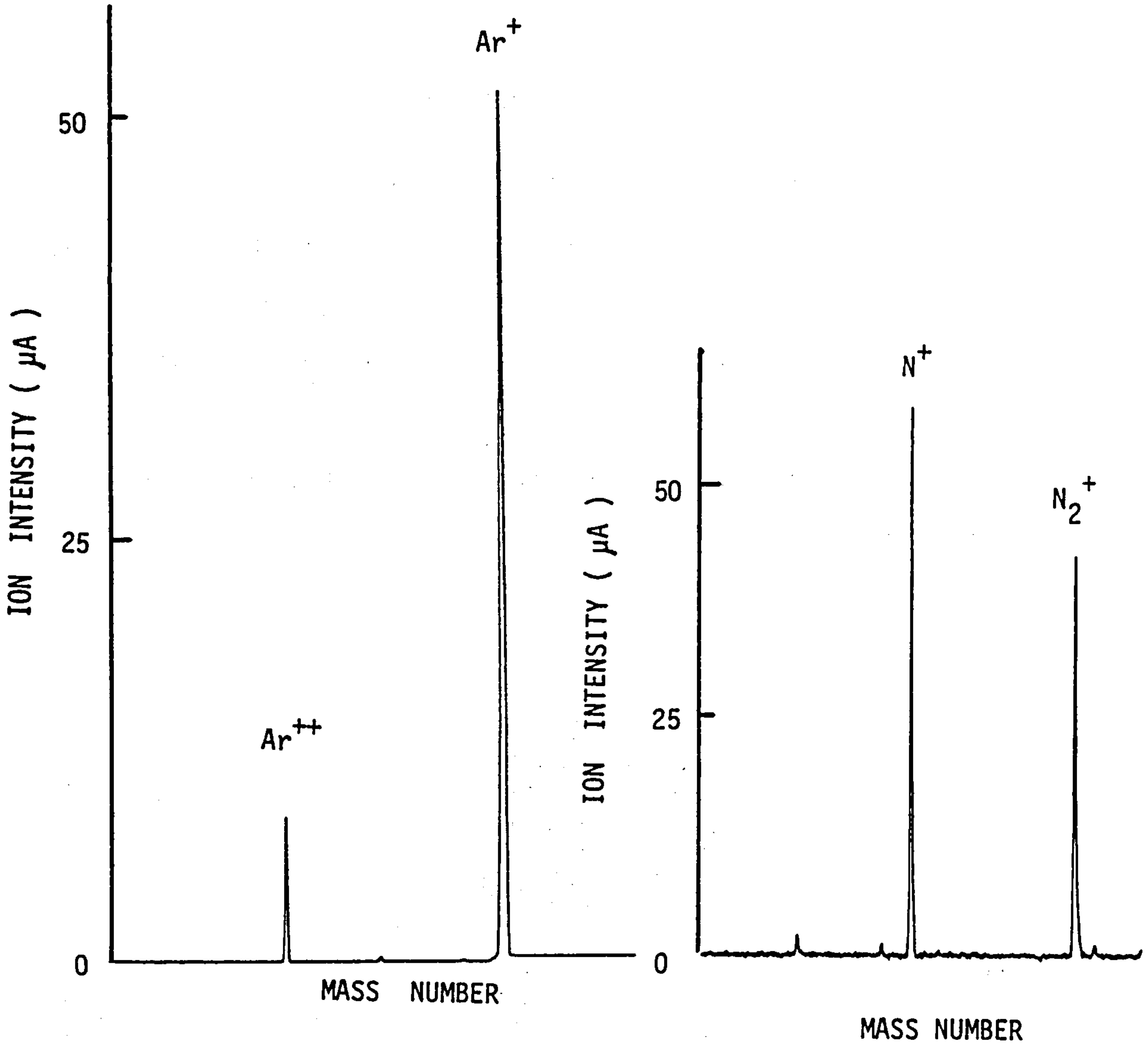

Fig. 2.13 Mass spectra for ion beams generated from (a) argon and (b) nitrogen gases.

2.3.4 Ion deceleration system

The mass-selected, high-energy ion beams are guided into a constrictor tube, which acts as a differential pump. The diameter of the constrictor is 20 mm. The ion beam is collimated to a 10 mm diameter by an aperture located in the constrictor tube. The ion beam is decelerated down to the final kinetic energy for deposition or etching, typically 0 to 3000 eV by an E x B type ion deceleration lens system. The details of this deceleration system are described in Section 2.5.

2.3.5 Vacuum pumping system

The vacuum pumping system for the present system is shown in Fig. 2.14. Two pumping ports are opened in the ion source section. One is at ground potential and the other is connected to the beam drift tube through a ceramic break. There are three oil diffusion pumps (1200 l/sec) backed with Liq. N_2 cold traps, water cooling baffles and rotary pumps. Viton O-ring seals are used on all flanges before the mass-analysis section. After the mass-analysis section, metal gaskets are used and all vacuum vessels are bakable up to 450 $^{\circ}$C, except for the gate valve seals which use viton O-rings.

After mass separation in the beam drift tube, a turbomolecular pumping unit is used. The beam drift tube can be isolated from the ion source section and the UHV chamber by two gate valves (V1, V2).

The UHV deposition chamber is pumped down using a conventional ion pump at a speed of 1000 l/sec.

The second vacuum chamber is connected to the first deposition chamber by a metal sealed straight-through valve (V3). Pumping is accomplished using gas helium type cryogenic pump, an ion pump, and a Ti-sublimation getter pump.

Typical base pressure for these deposition chambers are 5 x 10^{-10} Torr and 1 x 10^{-10} Torr, respectively. The present study was done in the first deposition chamber. The operating pressure during deposition was typically 5 x 10^{-8} Torr to 1 x 10^{-7} Torr due to the gas load from the ion source.

Therefore, the residual gas atom flux on the depositing surface could be estimated from the vacuum pressure (5 x 10^{-8} Torr) as

$$\Gamma_n = 3 \times 10^{13} \text{ (molecules/cm}^2\text{ s)}. \qquad (2.26)$$

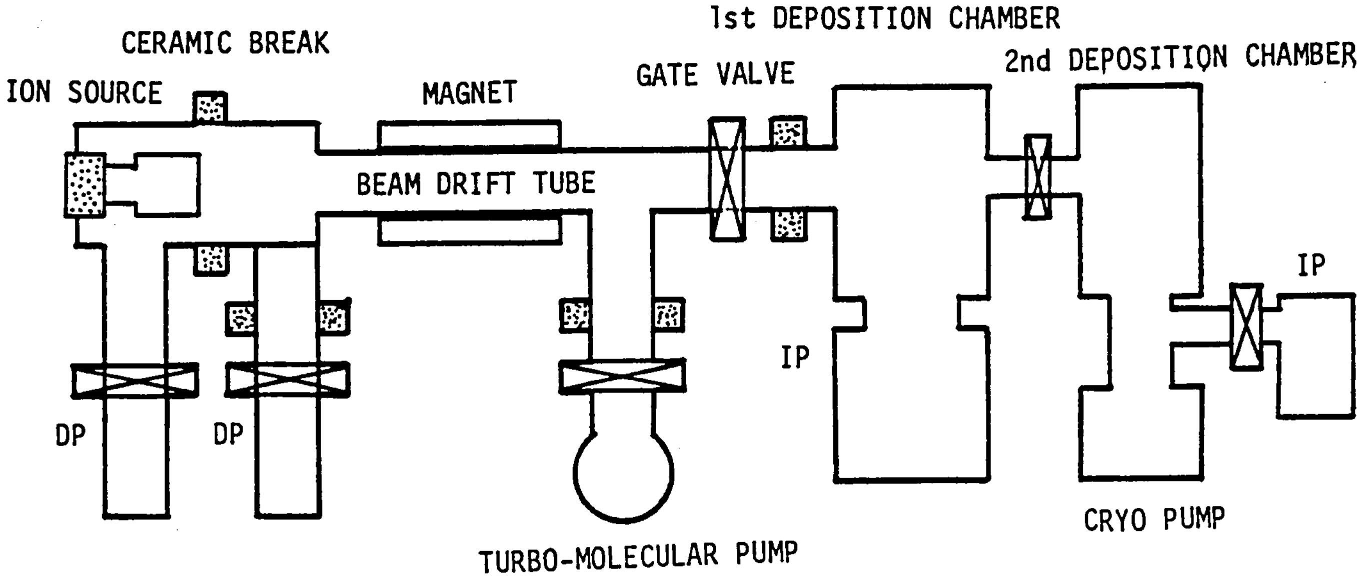

Fig. 2.14 Schematic of the vacuum pumping system.

2.4 The High Current Metal Ion Source

2.4.1 Introduction

A Freeman-type ion source was firstly developed for an isotope separator by J.H. Freeman[16] and has recently been widely used for high current ion implantation system. It has also been utilized in an ion beam deposition system, in which low-energy (10 - 500 eV), high-current metal ion beams are employed for thin film deposition. Minimal energy spread of the ion beam, uniform beam intensity and stable operation in a low-pressure region are required for various applications. The discharge characteristics of this type of ion source were firstly investigated by Freeman, who reported that it was hash-free and gave good mass resolution for isotope separation. However, study of the arc discharge in the ion source has not yet been completed, and only a few reports have appeared on energy dispersion of the ion beam uniformity of the beam's intensity, instabilities in the plasma in a low-pressure arc region, etc.

This section details a study of the discharge characteristics of the Freeman-type ion source. The diode characteristics of the source are investigated, and arc discharge characteristics are shown to be dependent on magnetic field configurations in the arc plasma. The energy spread of the ion beam is also discussed in connection with instabilities in the arc plasma.

2.4.2 Structure of the ion source

In principle, a Freeman-type ion source consists of an arc chamber and a rod filament located parallel to the arc chamber axis. A cross sectional view of the ion source is shown in Fig. 2.15. The arc chamber ($d = 25.4$ mmϕ, $H = 80$ mm) is made of graphite, and a tungsten rod filament ($d = 2$ mmϕ) is located off-axis in the chamber. The distance from the filament to the ion exit slit is 4 mm, and the slit is 1 mm wide by 40 mm long.

A weak magnetic field (0.01 T) is applied externally in the discharge region. This vertical magnetic field is parallel to the filament rod. Ions are extracted by accel/decel-type electrodes. The accel-electrode is Pierce-type shape and is kept 1 kV below the decel-electrode in order to obtain space-charge neutralization of the formed ion beam.

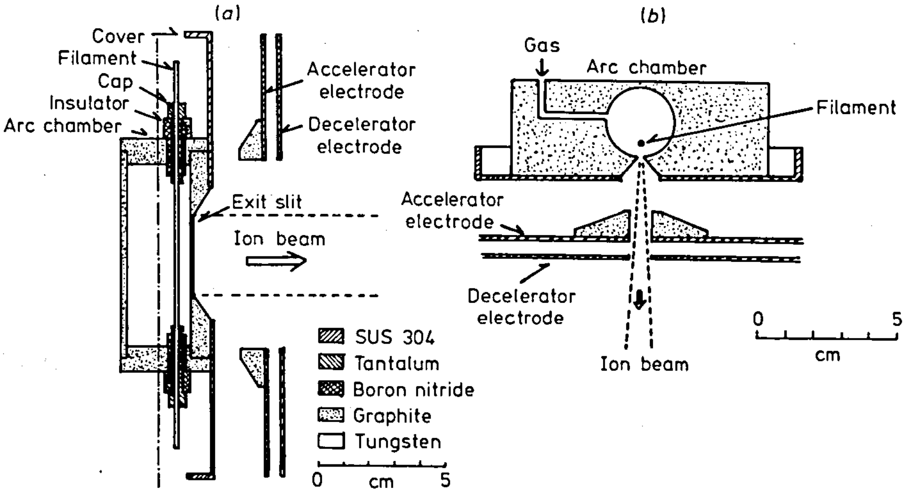

Fig. 2.15 Cross sectional views of Freeman-type ion source. (a) vertical plane, (b) horizontal plane.

2.4.3 Experimental

Experiments were carried out using the IBD machine described in Section 2.2. The diode characteristics were measured, with the ion source regarded as a vacuum tube. First, the gas feed was disconnected to prevent discharge in the arc chamber. The electron emission current, I_e, was measured as a function of the anode voltage, V_a, the filament heating current, I_{fil}, and the vertical magnetic field, B_z. The arc discharge was then initiated by introducing argon or nitrogen gas into the ion source. The pressure during ion source operation was from 7.8×10^{-4} to 5.2×10^{-2} Pa. The arc current was stabilized by the power supply. Changes in arc voltage and extracted ion current for a fixed extraction voltage of - 20 kV were measured by changing I_{fil} and B_z. The current density distribution of the ion beam was measured by moving two small Faraday cups vertically and horizontally at extraction energies of 15 - 30 keV. The Faraday cups were located 30 cm from the ion exit slit.

Energy analysis of the Ar^+ beam was carried out by retardation method with the extraction voltage as low as 500 eV. The energy analyzer has a small aperture (1 mmϕ) to exclude obliquely incident ions and to give good energy resolution. In order to detect any hash in the ion source, AC-components in the arc current, arc voltage and extracted ion current were observed by synchroscope.

2.4.4 Results and discussion

(a) Diode characteristics

Fig. 2.16 shows the diode characteristics of the ion source. Unlike in conventional diode tubes, the electron emission current, I_e, is proportional to the fifth power of the anode voltage, V_a. I_e reaches a maximum as filament current increases and then is cut off by the excess filament current. The application of vertical magnetic field B_z reduces the emission current.

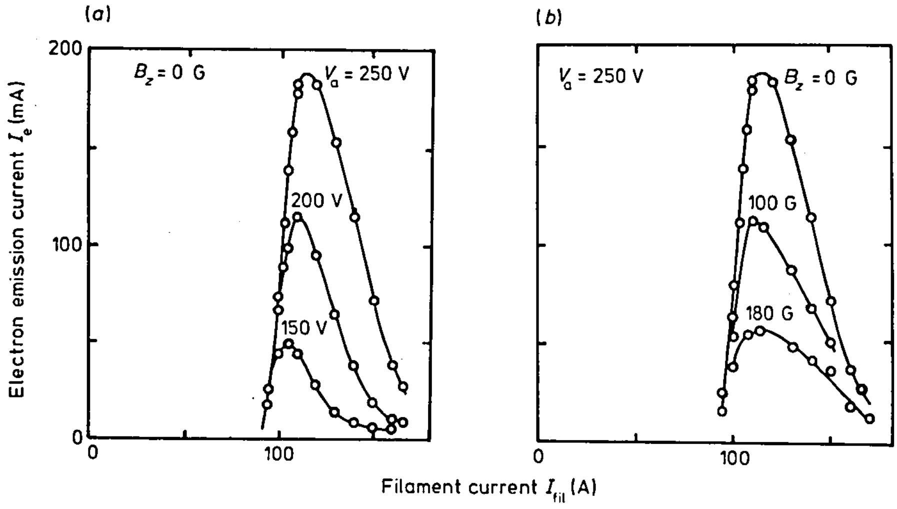

Fig. 2.16 Diode characteristics. Electron emission current versus filament current with (a) anode voltage, and (b) vertical magnetic field as parameters.

These diode characteristics can be explained in terms of the magnetic field produced by the filament current, as pointed out by Hull[17]. According to Hull, the electrons emitted from the filament follow a linear magnetron motion along the filament rod. This is caused by an azimuthal magnetic field generated by the filament current. In the low filament current region, the electron emission current is limited by the number of electrons emitted by the filament. This is the "temperature-limited region". When the filament current is increased, however, most of the emitted electrons are trapped by the magnetic field and cannot reach the anode. This is the "magnetically-limited region". Furthermore, the electrons will follow a circular magnetron motion caused by an externally applied vertical magnetic field. Therefore, a helical magnetic field exists in the ion source region. It is generated from the constant vertical magnetic field, B_z, and the azimuthal magnetic field, B_θ , whose strength is inversely proportional to the distance from the filament. Therefore, the geometric configuration of the magnetic field in the ion source can be the one shown in Fig. 2.17. Similar diode characteristics were also reported by Cobic et al.[18] and by Hinkel[19].

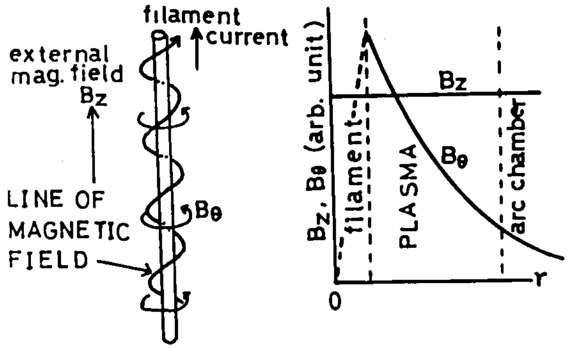

Fig. 2.17 Magnetic field configuration in Freeman-type ion source.

(b) Arc discharge characteristics

Figure 2.18 (a) shows that a change in the vertical magnetic field causes hysteresis of both the arc voltage and the ion current. Although the arc voltage increases greatly with a decrease in the vertical magnetic field, the ion current does not change so drastically. In Fig. 2.18 (b) it can be seen that a smaller filament current gives a larger ion current under a constant arc current(5.6 A). However, a decrease in filament current below 105 A quenched discharge because of the deficiency of emitted electrons. The steep increase in ion current can be explained in terms of the reduction in magnetic forces for electron trapping, due to the filament current decrease. That is, the arc voltage is raised to sustain the arc current against the reduction in magnetic forces for electron trapping, and, as a result, the ion current increases.

On the other hand, if the filament current is increased over 180 A, the discharge is again quenched because of excessive magnetic trapping of electrons. Arc current-voltage characteristics show hysteresis in most of the experiments.

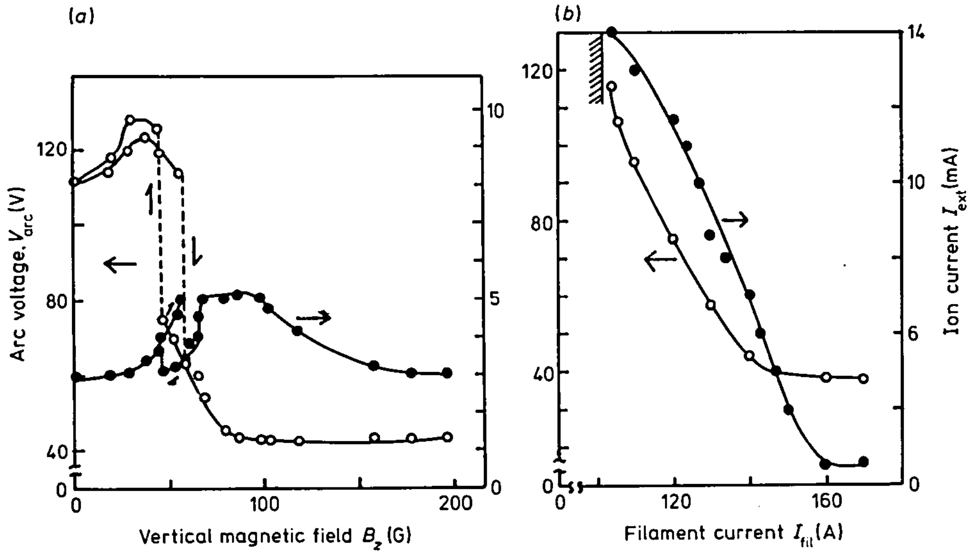

Fig. 2.18 Dependences of arc voltage and extracted ion current on (a) vertical magnetic field (gas : N_2, p= 6.1 x 10^{-3} Pa, I_{arc}= 5.6 A, I_{fil}= 144 A, and V_{ext}= 20 kV) and (b) filament current (gas : N_2, p= 6.2 x 10^{-3} Pa, I_{arc}= 5.6 A, B_z = 100 G, and V_{ext} = 20 kV).

(c) Beam uniformity and filament deterioration

Figure 2.19 shows the ion current density distribution of the ion beams. Horizontally, the ion beam is sharply focused and the current density distribution is symmetric. However, vertically, the distribution is asymmetric and beam uniformity is not good. The position of maximum intensity shifts from the center to the positive potential side of the filament. Filament rods were always thinned at the positive end as shown in Fig. 2.20. If the voltage polarity is reversed, the location of filament deterioration is also reversed. It seems, therefore, that plasma density is inhomogeneous along the filament rod, and the positive side of the rod is the location for intense plasma density because of the linear magnetron motion of the electrons.

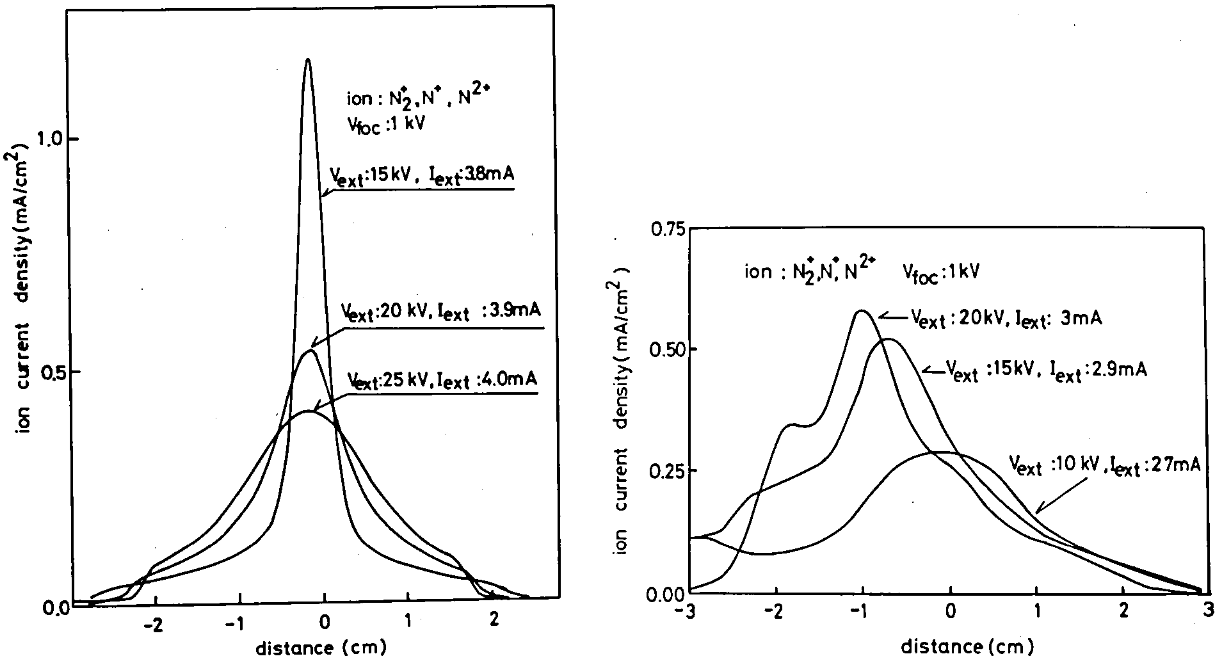

HORIZONTAL ION CURRENT DENSITY DISTRIBUTION. VERTICAL ION CURRENT DENSITY DISTRIBUTION

Fig. 2.19 Ion current density profiles: (a) horizontal and (b) vertical.

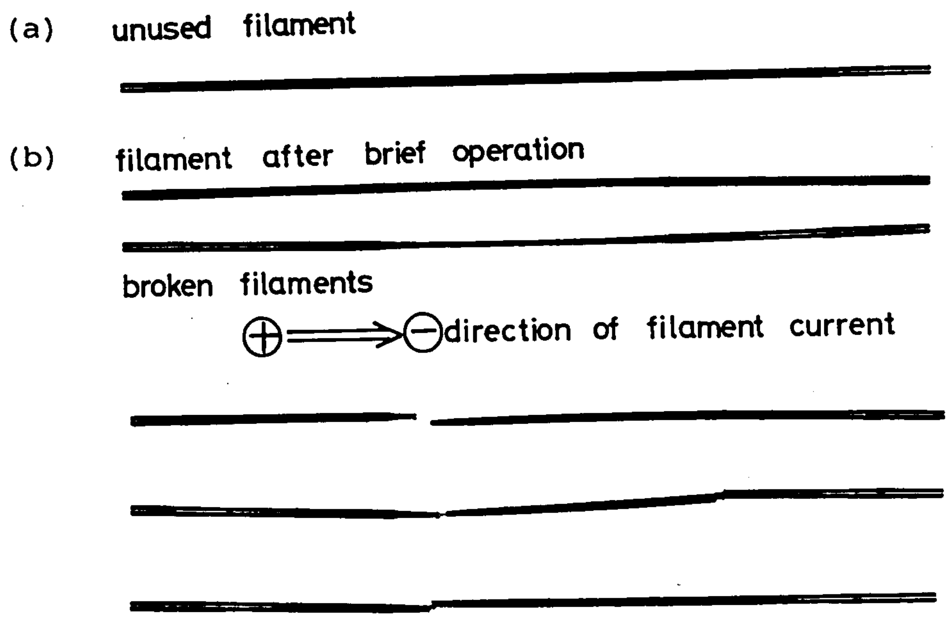

Fgi. 2.20 Tungsten filaments used in the ion source; (a) unused, (b) after argon gas discharge for 10 hours.

(d) Energy spread and plasma instabilities

The energy spectrum of an argon ion beam is shown in Fig. 2.21 (a), with the acceleration voltage kept at 500 eV. The energy spectrum is symmetric about the drift energy, 506 eV, which is a little greater than the extraction energy, 500 eV. The energy spread is 32 eV at halfwidth. This small difference (6 eV) seems to represent a fall in the anode voltage in the plasma. The observed values of the energy spread were 30 - 50 eV for these experimental conditions. These values are larger than those previously reported[16].

Fluctuations in the ion current are shown in Fig. 2.21 (b). The dc component of the ion current is 6 mA, and the overlapping peak-to-peak fluctuation amplitude is nearly 3 mA. A small-amplitude 100 Hz ripple and a large amplitude high-frequency fluctuation of several tens of kHz are superposed on the dc component. The amplitude of the fluctuation increases as filament current decreases, so that the fluctuation amplitude increases in the large ion current region.

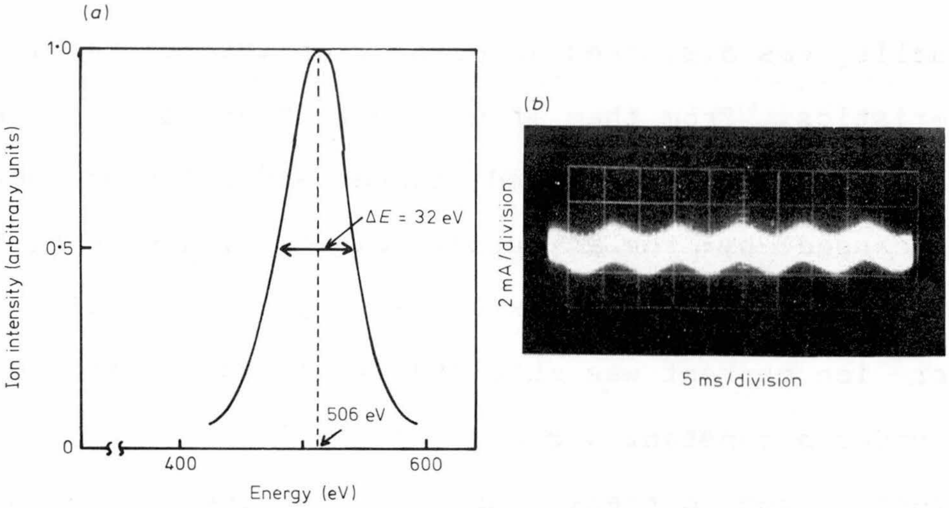

Fig. 2.21 Energy distribution of an argon ion beam: (a) Extraction energy is 500 eV. (b) AC fluctuations in the extracted ion current.

In general, the energy of an extracted ion represents the space potential in the plasma where the ion is created, if the ion is extracted without collision. In this experiment, it is hardly possible for ions to be charge-exchanged in the extraction region since the vacuum pressure in the extraction region is 10^{-3} Pa, or less. Therefore, high-frequency oscillations in the space potential of a plasma are thought to be the reason why an energy spread of several tens of eV was observerd. This is because in the retardation method measurement energy spectra are time-averaged ones of the instantaneous spectrum over many oscillation periods.

2.4.5 Conclusions

The discharge characteristics of a Freeman-type ion source were examined in some detail in a low-pressure region, and the beam quality was discussed in connection with those discharge characteristics. From them it was shown that the electrons in the ion source follow mixed linear and circular magnetron motions caused by the azimuthal magnetic field generated by the filament current and an externally applied magnetic field. A larger ion current was obtained by decreasing the filament current under a constant arc current.

Horizontal ion current density distribution is sharply focused and symmetric, although in the vertical direction the beam intensity is not uniform because of the inhomogeneity in plasma density along the filament rod. The energy spread of the ion beam is large (30 - 50 eV in halfwidth) compared with previously reported values[16]. The observed large energy spread can be explained in terms of high-frequency fluctuation in the space potential of the arc plasma.

2.5 The Ion Beam Deceleration Lens System

2.5.1 Introduction

Studies of the interactions between low-energy ion beams and solid surfaces, such as sputtering, deposition, etc., have become of great importance in many fields. These studies include such topics as plasma-wall interaction problems in fusion reactors[20], and ion based film formation techniques[21].

For these, it is necessary to produce high intensity ion beams in an extremely low-energy region, typically below 3000 eV. In addition, an ultra-high vacuum environment is often required for ion irradiated surface observations. The most commonly used method to produce such a low-energy ion beam is to decelerate a high-energy intense ion beam from an isotope separator to a low energy state.

Several studies have already been reported[2-10,22-28] on ion beam deceleration. It is empirically well known that an electrostatic bi-potential lens system can focus the ion beams strongly during deceleration[4]. Recently, Alton, et al.[28] calculated the focal properties of these lens systems. However, there have been few experimental studies on ion beam deceleration techniques in which practical considerations have been taken into account.

It is well known that space-charge neutralization using electrons is essential for the transport of high-intensity ion beams. Therefore, in the case of electrostatic ion retardation, acceleration of the electrons would take place simultaneously, which would cause serious heat-up damage to the deposited films or irradiation targets[29]. In most cases, it becomes impossible to measure the precise ion current because of the large current drain due to the electrons.

The vacuum pressure in the ion decelerating region might cause degradation of the decelerated ion beam since the cross section for charge exchange becomes quite large as the ion energy decreases to below a few hundred eV[30]. Reflection of the ion beam before a target surface might cause sputtering of the electrodes by re-accelerated high-energy ions.

This section describes a method for directly observing ion beam trajectories during deceleration using an N_2^+ ion beam as a test beam. The focusing characteristics of the E x B type ion decelerator used in the IBD apparatus is examined using this method.

2.5.2 The E x B type ion deceleration lens system

For retardation of high intensity ion beams, it is essential to separate the space charge neutralizing electrons from the ion beam trajectories. An electrostatic electron suppressor method often results in high tension breakdown because of electron multiplication phenomenon in the decelerating field.

Here, an E x B type ion deceleration system[7] has been developed to overcome this difficulty. It makes use of the fact that a weak magnetic field applied perpendicular to the ion beam axis causes the electrons to drift across the ion beam trajectories by linear magnetron motion, whereas the ion beam trajectories are not appreciably influenced by this crossed-electromagnetic field. Fig. 2.22 shows a schematic of the system. Two permanent magnets (not shown) are used to generate a 300 gauss magnetic field. The target is held at ground potential so that the kinetic energy of the decelerated ions is determined by the ion source potential, eV_a. V_{ext} indicates the ion extraction voltage for the ion source.

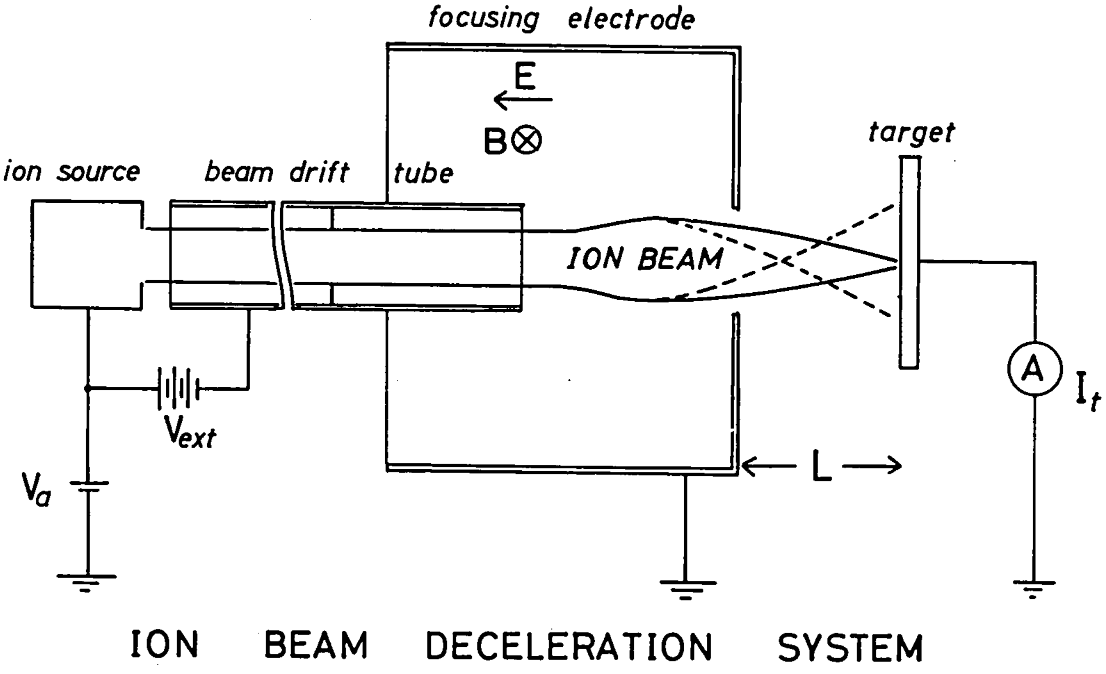

Fig. 2.22 Schematic of an E x B type ion beam deceleration lens system. A magnetic field of strength of 300 G is applied perpendicular to the ion beam trajectory axis using two permanent magnets (not shown).

The cylindrical electrode shown in Fig. 2.23 focuses the decelerating ion beams on a small spot. This focusing electrode also acts as a collector for the drifting electrons. At the side of the electrode, a tungsten mesh (#80) has been spot-welded to allow observation of the ion beam trajectories inside the electrode.

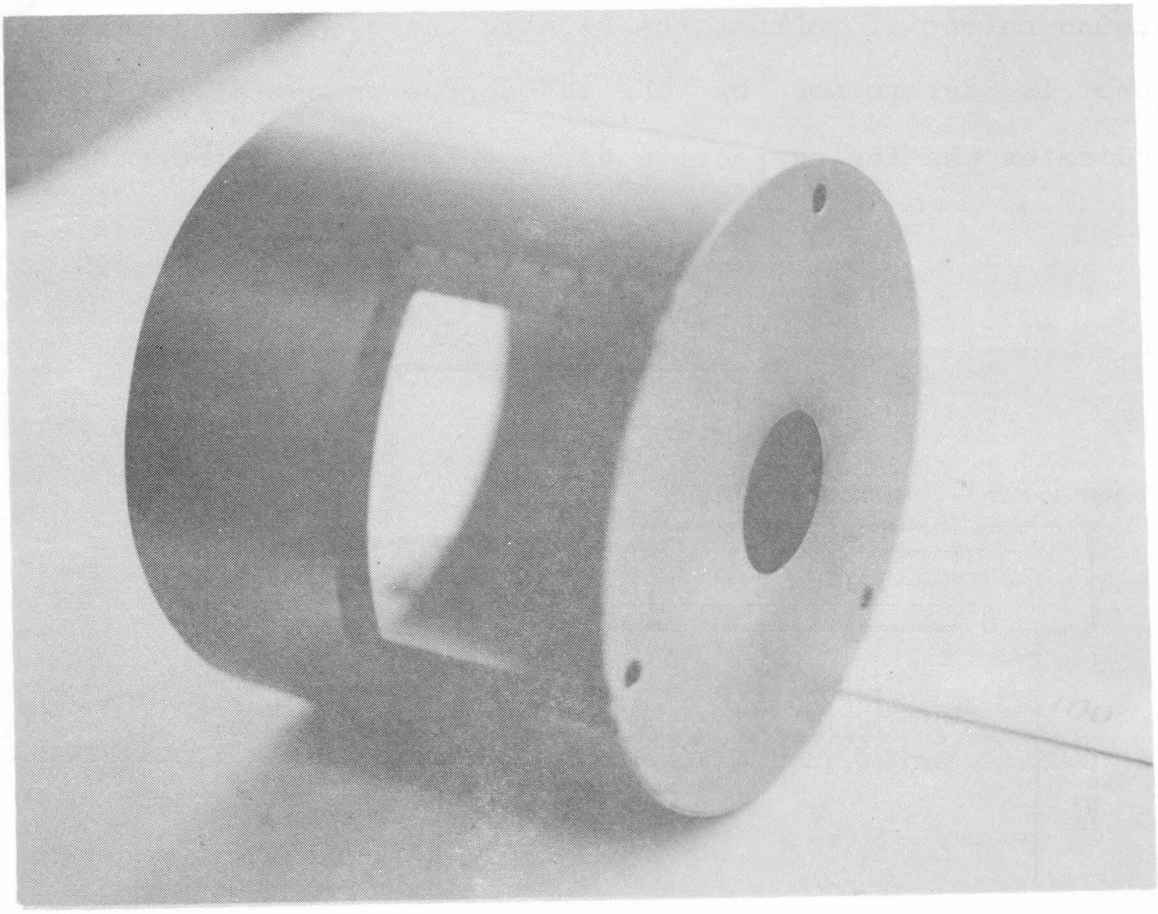

Fig. 2.23 Cylindrical focusing electrode. A rectangular window made of tungsten mesh(#80) is spot welded to one side to observe the ion beam shape inside the focusing electrode.

2.5.3 Experimental

The experiments in this study were carried out in an Ion Beam Deposition (IBD) machine, the details of which has been described in Section 2.3. A molecular nitrogen ion beam, N_2^+, was chosen as the test ion beam for observation of the decelerating ion beam. This is because optical emissions from an N_2^+ ion beam are in the visible wavelength region.

The hot-cathode, arc-type ion source described in Section 2.2. was used to produce the N_2^+ ion beam. The ions were extracted at an extraction energy of 25 keV and mass-analyzed using a magnet. Space charge neutralization of the ion beam with electrons was automatically performed in the beam drift tube at vacuum pressures of 10^{-4} to 10^{-6} Pa. The mass-selected N_2^+ ion beam was guided into a constrictor tube (ID = 20 mmϕ) and collimated to 10 mmϕ by a slit. It was then decelerated down to the final kinetic energy, eV_a, by the E x B type ion deceleration lens system mentioned above.

The cylindrical focusing electrode, as shown in Fig. 2.23, was located at 40 mm from the exit of the constrictor tube. The shapes of the decelerated N_2^+ ion beams were photographed from a horizontal angle with a camera using ASA 3000 polaroid films. Exposure times over 30 minutes were needed.

The relation of the target ion current, I_t, to the final kinetic energy, eV_a, was measured for three target locations. The diameter of the target was 40 mm.

The effect of poor vacuum conditions on the I_t - eV_a characteristics were examined by turning the vacuum pumps off.

The mass spectrum for decelerated ion beams from $SiCl_4$ gas discharge was obtained at an extraction energy of 18 keV.

2.5.4 Results and Discussion

(a) Direct observation of ion beam trajectories

Fig. 2.24 shows the trajectory of an N_2^+ ion beam which was decelerated from eV_{ext} = 25 keV down to eV_a = 1 keV inside the focusing electrode. The ion current was 100 μA and the vacuum pressure was 1.3×10^{-4} Pa. The target is not shown. It can be seen that the 10 mm collimated ion beam at first diverges slightly and then is focused strongly as it passes through the exit hole of the focusing electrode.

When the ion source potential, V_a, was made to negative, for example, at - 1 kV, the incoming N_2^+ ion beam was repelled inside the focusing electrode. This is shown in Fig. 2.25. A sharp boundary is clearly observed where the ion beam is reflected. Figure 2.26 was obtained by summarizing those beam shapes for several ion acceleration energies with a fixed extraction energy of 25 keV: (a) V_a = - 3 kV, (b) - 1 kV, (c) 0.1 kV, (e) 2 kV, and (f) 3 kV.

It should be noted that in cases of (a) and (b), the reflected ion beam is re-accelerated and focused towards the central axis because of the radially inward electric field. The turning point of the ion beam for (b) is closer to the focusing electrode than for (a). In cases (c) - (f), the focal length increases with ion acceleration energy. These focusing properties are qualitatively in good agreement with the numerical calculations of Alton, et al[28].

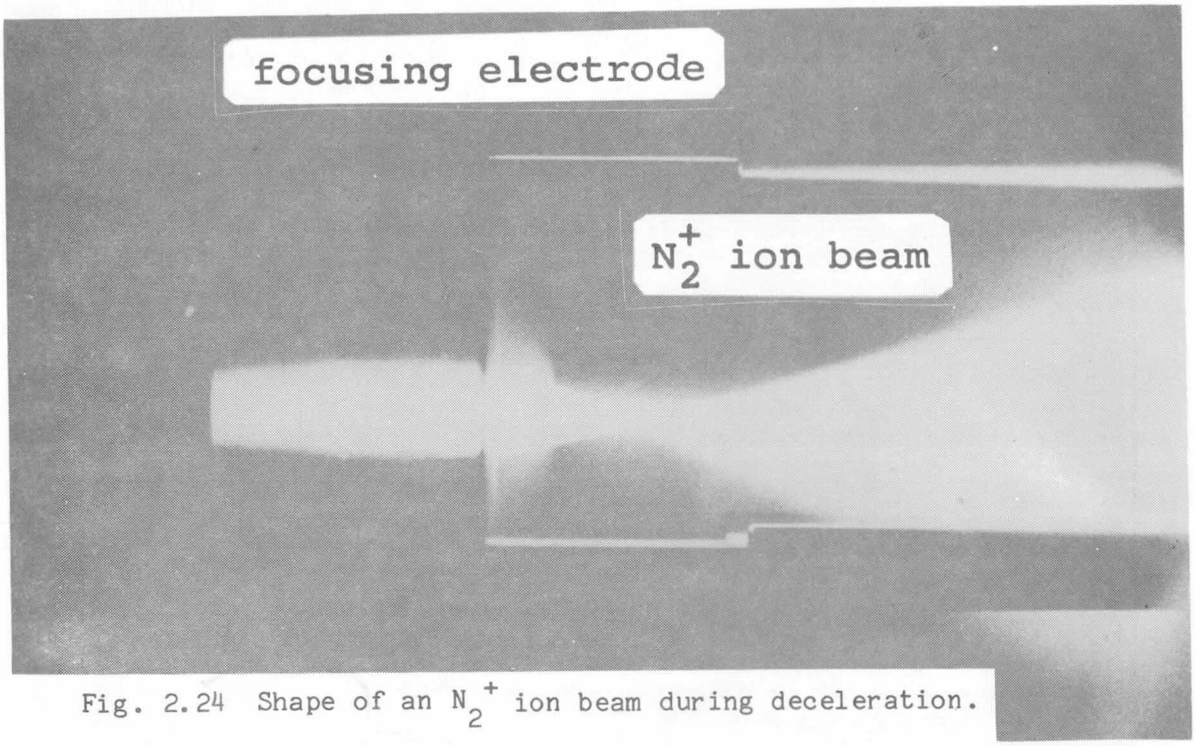

Fig. 2.24 Shape of an N_2^+ ion beam during deceleration. The initial kinetic energy is 25 keV and the final kinetic energy is 1 keV.

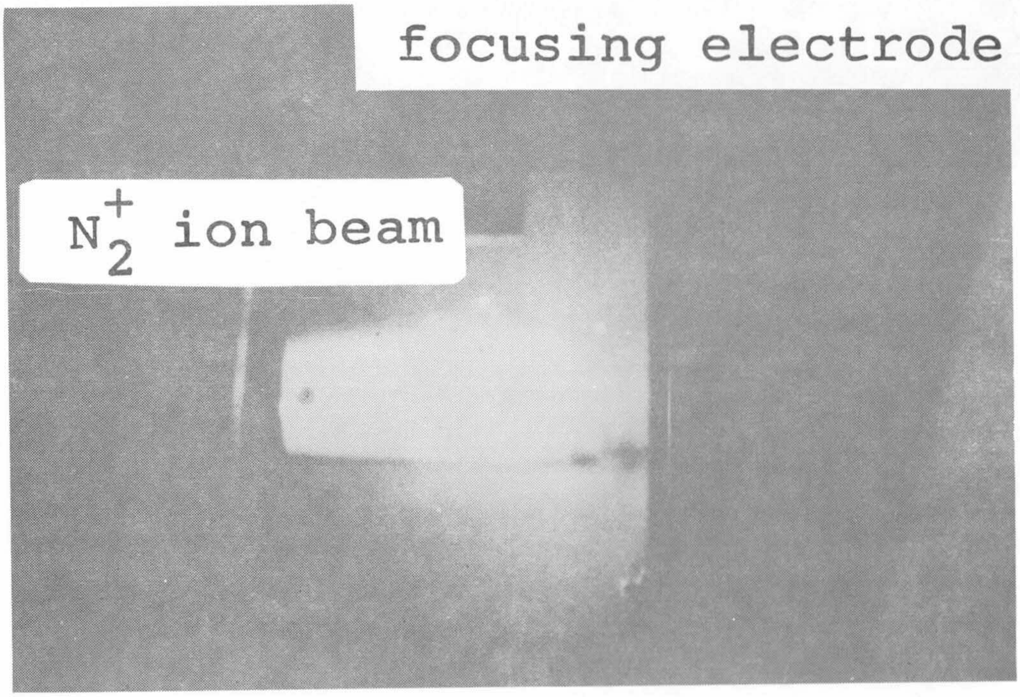

Fig. 2.25 Shape of an N_2^+ ion beam in the case of reflection inside the focusing electrode. eV_{ext} = 25 keV, V_a = − 1 kV.

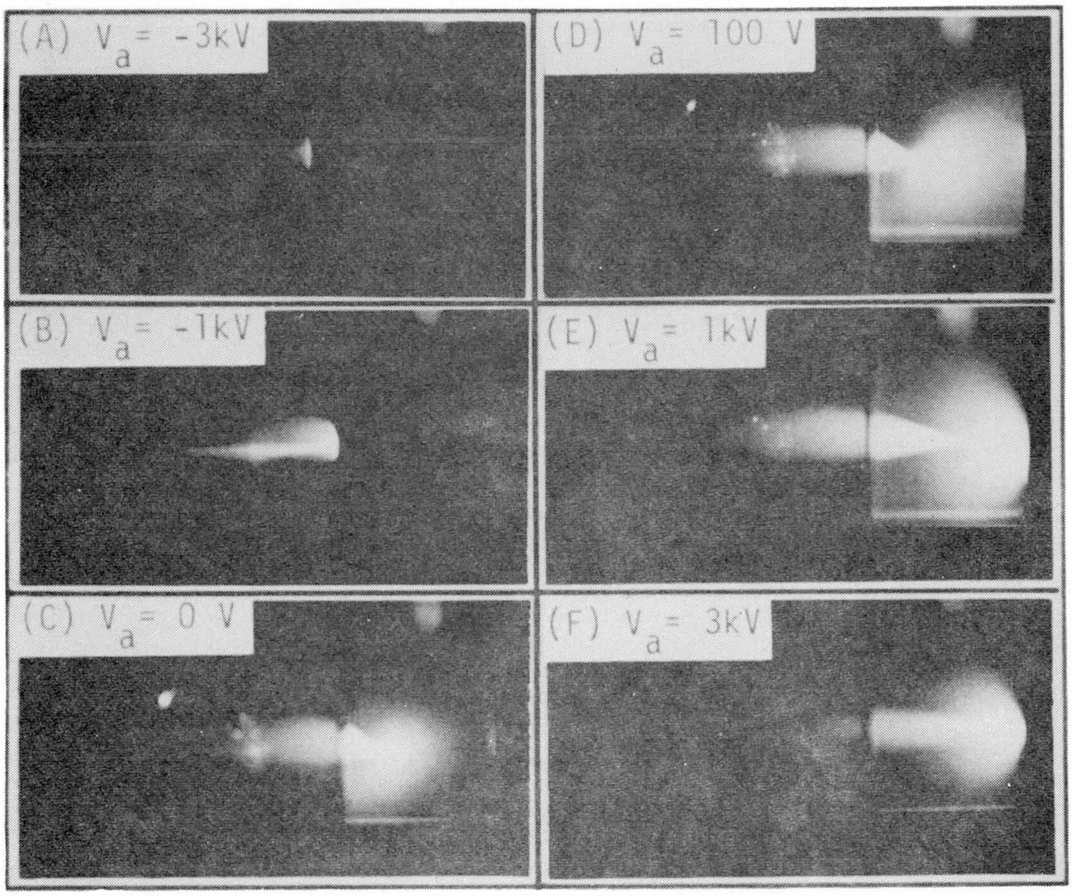

Fig. 2.26 Shapes of N_2^+ ion beam trajectories during deceleration The initial kinetic energy is 25 keV and final ion acceleration veltages is (a)- 3 kV, (b) - 1 kV, (c) 0 V, (d) 0.1 kV, (e) 1 kV, and (f) 3 kV.

(b) Dependence of decelerated ion current on ion energy

The dependence of the target ion current, I_t, on the final kinetic energy of the decelerated ion beam, eV_a, is of practical importance in designing low-energy ion beam accelerators. In Fig. 2.27, target ion current dependences on ion energy are shown for three target locations: l_2 = 3 mm, 40 mm, and 94 mm. The extraction voltage and the ion current were kept at 25 kV and 100 μA, respectively.

When the target is far from the focusing electrode, at l_2 = 90 mm, I_t increases linearly with ion energy. At l_2 = 40 mm, I_t saturates at an ion energy of 1.3 kV. When the target is close to the electrode, at l_2 = 3 mm, I_t shows a constant value above 200 eV. Comparing these results with the ion beam trajectory observations shown in Fig. 2.26, it can be concluded that target ion current is influenced by target location. This is especially so in the low-energy range, because of the cross-over effects of the decelerating ion beam. The decrease in the ion current below 200 eV is thought to result from the energy spread of the incoming ion beam.

It should be noted that space charge repulsion during deceleration cannot be used to explain the decrease in low energy region because the whole content of the ion beam is collected by the target located at l_2 = 3 mm. A small hump at around 200 to 300 eV was frequently observed. This phenomenon is thought to be related to the increased emission of secondary electrons.

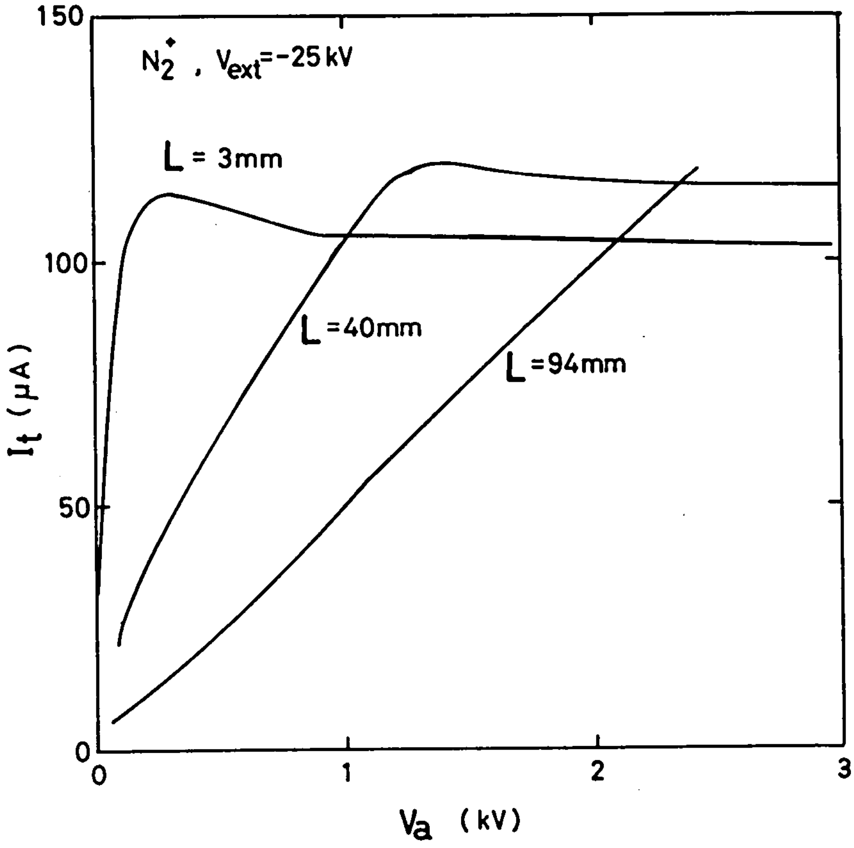

Fig. 2.27 Dependence of target ion current on ion acceleration energy for three different target locations. eV_{ext} = 25 keV, l_1 = 40 mm; l_2 = (a) 3 mm, (b) 40 mm, and (c) 92 mm.

(c) Influence of vacuum pressure

The effects of the vacuum pressure in the ion retardation space on the I_t - eV_a characteristics were examined by shutting the pump off. At a vacuum pressure of 1.3×10^{-3} Pa, an arc shaped glowing plasma was observed near the focusing electrode. Fig. 2.28 (a) shows the I_t verus ev_a relation when the target was immersed in the glowing plasma. The target current was always negative over the entire ion energy range and the step increase was found at $V_a > 0$ volt. In contrast, if the target was separated greatly from the glowing plasma for example, $l_2 = 46$ mm, normal I_t - eV_a characteristics were obtained. This is shown in Fig. 2.28 (b).

These phenomena indicate that, under poor vacuum conditions, the high electric field in the ion retardation space leads to plasma formation in which electron multiplication occurs[29]. Higher gas pressure in this equipment over 10^{-2} Pa caused appreciable charge exchange in the beam and often resulted in high tension breakdown[30]. In the case of vacuum pressure below about 10^{-4} Pa, no plasma formation was observed and only very weak optical emission from the N_2^+ ion beam trajectories was observed.

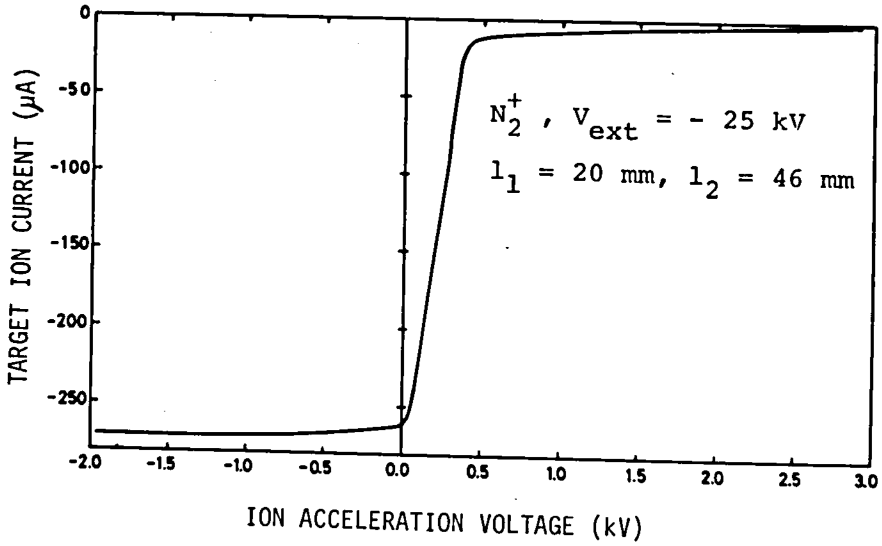

(a)

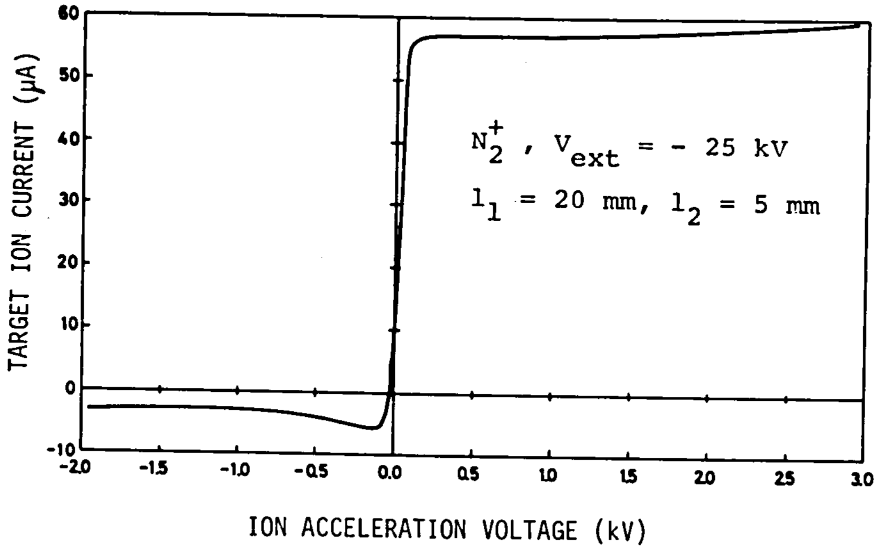

(b)

Fig. 2.28 Target ion current dependence on ion acceleration energy in a poor vacuum. (1.3 x 10^{-3} Pa). In (a), the target is immersed in a glowing plasma and in (b) the target is outside the plasma.

(d) Mass spectrum of the decelerated ion beam

In Fig. 2.29 a typical mass spectrum for an ion beam generated from $SiCl_4$ gas discharge is shown. Here, the ion extraction energy is 18 keV and the final kinetic energy of the decelerated ion beam is 2 keV. The ion beam diameter on the target was 5 mm for l_1 = 20 mm and l_2 = 3mm. By optimizing ion source operation and beam transport $^{28}Si^+$ ion beams have been obtained in 200 to 300 μA ion current range at an ion energy of 100 eV.

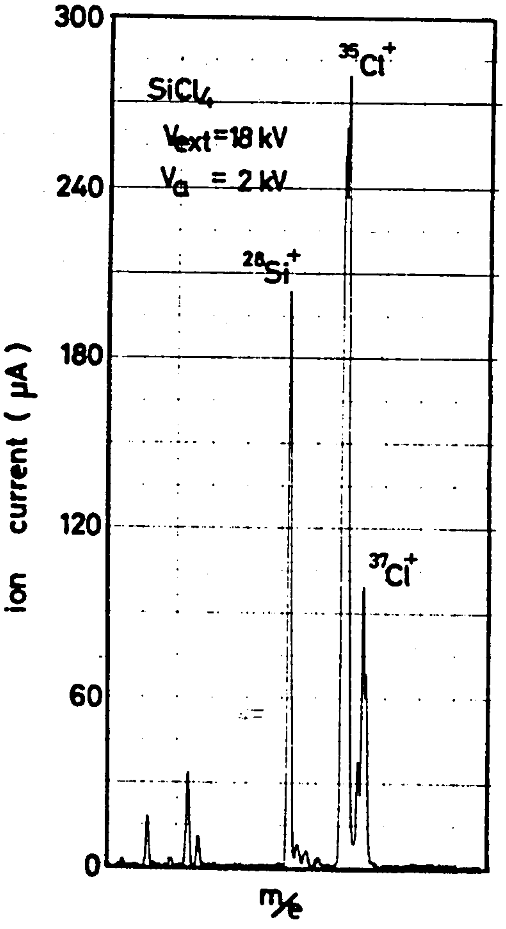

Fig. 2.29 Typical mass spectrum of a decelerated ion beam generated from $SiCl_4$ gas discharge in a Freeman-type ion source. eV_{ext} = 18 keV, eV_a = 2 keV, l_1 = 40 mm, and l_2= 3 mm.

2.5.5 Conclusions

The focusing properties of an E x B type ion beam deceleration lens system were examined by directly observing the visible optical emissions from N_2^+ ion beams. It was demonstrated that a crossed-electromagnetic field is effective in removing space charge neutralizing electrons from the decelerating ion beam. The decelerated ion beam is strongly focused by the lens effects of the E x B type deceleration system. The beam shapes are qualitatively in good agreement with the numerical calculations of Alton, et al.

It was shown that a poor vacuum in the ion retarding space leads to glowing plasma formation. Ion currents of 200 to 300 µA were obtained for $^{28}Si^+$ at an ion energy of 100 eV using this ion deceleration method.

2.6 Summary

In this chapter, a detailed discussions were presented on a low-energy, mass-separated ion beam accelerator for use in ion beam deposition and etching studies. The design criteria for the system were discussed from the viewpoints of ion energy, ion current, and vacuum environmental conditions, etc. It was demonstrated that space charge neutralization of the ion beam is essential for the transport of a high intensity ion beam. At the same time, exclusion of the neutralizing electrons is needed for low-energy ion beam producing when a deceleration method is used. It was shown that a crossed-electromagnetic field ion retardation system can do both, and the detailed features of the system were described. Finally, an ultra-high vacuum ion beam accelerator that can produce mass-separated ion beams with an ion current of up to 300 μA at an ion energy as low as 100 eV was introduced. The apparatus was successfully utilized for the ion beam deposition and etching studies described in Chapters 3 and 4.

５４ 項欠

Chapter 3 ION BEAM DEPOSITION

3.1 Introduction

Thin film formation technology applications have ranged from small-scaled electronic devices to large-scaled machinary products such as aircraft. In many cases, high controllability for film formation technology and, at the same time, high deposited film quality have been required[1].

For example, in VLSI (Very Large Scale Integration) semiconductor fabrication applications, the increase in intergration has made it necessary to control film composition, stoichiometry, thicknesses, crystalline structure, and the doping profiles of implanted impurites with submicron dimensional precision[2]. For these purposes, the deposition temperature must be kept low enough to ensure that well-defined material profiles are not influenced by solid phase interdiffusion.

Due to this need for precise controllability, conventional high temperature chemical reaction type techniques are essentially no longer suitable for these highly precise applications. Other newer techniques of a physical nature are being widely investigated. Among these physical deposition techniques, ion beam deposition(IBD) has attracted the increasing interest of many investigators[3,4].

This deposition technique employ a low-energy ion beam in a high-vacuum region. The idea of IBD was reported by W.E. Flynt in 1961 for the fabrication of microminiaturized electronic circuits[5]. However, he only discussed ion source characteristics. Conductive and resistive film deposition using ion beams was reported by A.W. Wolter in 1965[6]. Cr^+ ion beam deposition on a glass substrate was carried out by B.A. Probyn in 1968 using a specially designed ion retardation system[7]. The optimum conditions achieved in this experiment were a 0.5 mm diameter for a beam current of 2 μA, and an energy of 230 eV. The condensation efficiency was found to be approximately 25 %, which gives a deposition rate of 100 Å/min.

These studies in 1960's were done with non-mass-analysed equipment and some inclusion of evaporated neutral particles was observed.

In the 1970's, S. Aisenberg and R.W. Chabot described the deposition of silicon and carbon films[8]. They obtained Si epitaxial films on Si substrates at an ion energy of 40 eV and a substrate temperature of 300°C and the diode characteristics of the deposited p-n junctions were reported. Also, diamond-like carbon films were obtained using a sputter ion source. The carbon films were optically transparent and hard enough to be used for cutting tools.

E.G. Spencer, et al. discussed the crystalline structure of ion beam deposited carbon films using X-ray and electron-diffraction analysis[9]. They showed that the films consist of a polycrystalline background of cubic diamond with particle sizes of 50 - 100 Å and single crystal regions up to 5 μm in diameter. These experiments proved that materials at metastable state can be obtained at low temperatures using IBD.

Since the beginning of the 1970's, film deposition using mass- and energy-selected ion beams in high vacuum regions have also been developed. In these methods, a pure ion beam, without neutral particles, is used after deceleration to provide suitable incident energy for film fomation.

The Pb oxidation process was studied using a low energy O_2^+ ion beam by J. Geerk and O. Meyer[10]. However, the sputtering of Pb atoms by O_2^+ ions restricted the maximum beam energy for oxide formation to about 50 eV.

J.S. Colligon et al. investigated the deposition of thin films by retardation of an isotope separator beam using Pb^+ and Cu^+ ions which were deposited onto Si single crystal substrates[11]. The 20 keV ion beam of the selected isotope was deflected by the potential on the deflector plates and retarded to 60 eV with a collected ion current of 15 μA, while keeping the substrate at high potential. This retarded ion current allowed deposition of Pb films at a rate of 100 Å/h over an area of about 3 cm^2. Additionally, the further deposition of Cu^+ ions followed by Pb^+ ions was carried out to produce a sandwich structure of Si-Cu-Pb.

A retardation technique for high energy ion beam to very low energies in an ion implantation accelerator was studied by K. Miyake[12], and J.H. Freeman[13] in 1976 in order to utilize high current ion beams from the low-energy ion implanter to obtain uniform deposited layers. The final ion energy could be adjusted to from 10 to 3000 eV. A weak magnetic field was applied to suppress the acceleration of secondary electrons inside the acceleration and retardation lens structure. Recently, epitaxial synthesis of diamond-like carbon films by carbon ion deposition at low energy was announced by J.H. Freeman et al[14].

Further studies on thin film deposition using low energy ion beams have been carried out by J. Amano et al.[15-18]. The deposition of Pb^+ ions on carbon and NaCl substrates were carried out with a 24 - 256 eV, 9 - 12 μA ion beam, in a 1 x 10^{-8} Torr vacuum. 50 eV ion energy was the optimum energy for deposition when parameters such as space charge expansion, self-sputtering, film thickness, and surface coverage were taken into account. As the deposition energy was increased to above 50 eV, the crystalline structure of the deposits grown on NaCl substrates became more ordered, with a strongly preferred (111) orientation. The deposition of Mg^+ ions on carbon substrates was also studied in a range of energies between 24 and 500 eV. The adhesion of the film improved at high energies.

G.E. Thomas et al. studied the deposition of Ag^+ ions on polycrystalline Pd and single-crystal Si(111) substrates[19]. They named this type of deposition "Epiplantation". Ions extracted from the source at 10 keV were formed into a beam by an Einzel lens and were decelerated from 10 keV to 20 eV after mass selection. Ag^+ ion currents in the range of 5- 25 μA were deposited onto the substrates in a 2 x 10^{-9} Torr vacuum.

The collection efficiencies of Ag^+ ions on a polycrystalline Pd substrate was obatained as a function of energy. In the energy range 25 - 100 eV, Ag layer deposited on the Si(111) surface at room temperature showed epitaxial growth as Ag(111)//Si(111).

K.Yagi et al. discussed the epitaxial growth of Ge^+ on Ge and Si substrates using an improved ion implantation facility[20,21]. Ge films were epitaxially grown on Si(111) and Ge(111) substrates at a substrate temperature of 300°C. Films deposited below 200°C were amorphous, and crystallized after post annealing at temperatures above 300°C. K. Miyake et al. developed a high current ion beam deposition apparatus and investigated Ge and Si epitaxial growth on Si(100) substrates[22], the details of which are described in this thesis (Chapter 2).

A similar apparatus was developed by T. Tsukizoe et al. in 1976 to study the fundamental deposition mechanism[23]. Zn^+ and Ag^+ ions with energies of from 30 to 300 eV were plated onto single crystal Al, Cu, and stainless steel substrates. The interface layer of the deposited films was observed by TEM and AES analysisis.

Several attempts to investigate the effects of ion inclusion in film formation processes using ion sources combined with vacuum evaporation equipment have been reported.

Itoh and Nakamura used a partially ionized vacuum evaporation technique to deposit a silicon film on a silicon single crystal substrate using the ion-to-neutral atom ratio and substrate temperature as parameters[24]. They observed epitaxial growth of deposited film at relatively low substrate temperatures when higher ion contents were chosen. The ion energy range of their experiments was rather high and, as a result, a higher backscattering yield was observed for the deposited film when the substrate temperature was in the 600°C range.

S. Shimizu and S. Komiya investigated partially ionized evaporation[25]. They described the low temperature epitaxial growth of silicon on Si(111) and sapphire substrates at substrate temperatures as low as 450°C.

Takagi et al. developed a technique called "Ionized Cluster Beam Deposition", in which metal cluster particles composed of 500-1000 atoms with a single electric charge were accelerated through several kV and deposited[26]. The effective energy of each deposited atom was several eV. They obtained epitaxial growth of deposited silicon films on a silicon single crystal substrate under acceleration, whereas amorphous deposits were observed without acceleration.

These experiments clearly show the effectiveness of ion inclusion in a film deposition system and, as a natural consequence, the concept of pure ion beam deposition has been explored by several investigators. In the ion beam deposition(IBD) scheme, deposition parameters, such as incident ion energy and deposition speed, are easily controlled electrically, and the effects of incident energy on film qualities are easy to determine.

This chapter investigates the roles of ion bombardment on film growth, which are listed in Table 3.1. Detailed discussions on the effects of sputtering and ion implantation are given. The interface layer of deposited films is investigated by relating them to an ion induced atomic mixing phenomenon. The heteroepitaxial growth of germanium films and homoepitaxial growth of silicon films on single crystal silicon substrates are also investigated as examples of low temperature crystal growth using IBD techniques.

Table 3.1 Flow chart of ion beam deposition.

Parameters	Mechanism	Applications
• Ion species • Ion current density • Ion beam size • Ion energy • Angle of irradiation • Ratio of ions to neutrals • Substrate temperature • Atmospheric conditions Vacuum pressure etc.	• Deposition Film formation • Sputtering Surface cleaning Strong bond formation Increase in density • Implantation Adhesion Nucleation center formation • Chemical Effect Increase in sticking probability	• Crystal growth Low temperature epitaxy • New material synthesis Diamond film Amorphous formation • Ion doping MBE applications • 3-dimensionally controlled electro-optical new devices • Surface coatings

3.2 Sputtering and Ion Implantation Effects

The deposition of energetic ions usually causes simultaneous sputtering and implantation at the surface of the substrate. Sputtering of both substrate and deposited atoms ("self-sputtering") occurs. Therefore, in order to obtain film deposition, the incident ion energy range has to be set well below that which gives a sputtering yield equal to unity for "self-sputtering".

In Fig. 3.1, deposited germanium film thickness and etched silicon substrate depth are shown as functions of incident ion energy and ion species. In contrast to the simple sputtering results of incident Ar^+, deposition of germanium film is clealy evident at energy levels below 500 eV. At energy levels above 800 eV, film buildup is not observed. On the contrary, the silicon substrate is etched considerably.

The result of calculating the sputtering yield using the Sigmund theory[27] indicates that the sputtering yield reaches unity at incident ion energies of 400 eV for Ge^+/Ge and 700 eV for Ge^+/Si. These values are in good agreement with the experiment.

Fig. 3.2 shows the amount of germanium on the substrate surface. It was measured by XMA as a function of Ge^+ ion incident energy. Throughout this experiment, the electron probe energy was 10 keV. This corresponds to an electron penetration of 500 nm. which is deeper than the deposited film thickness. The amount of germanium (intensity of the Ge-Kα, X-ray line) present on the surface decreased as the

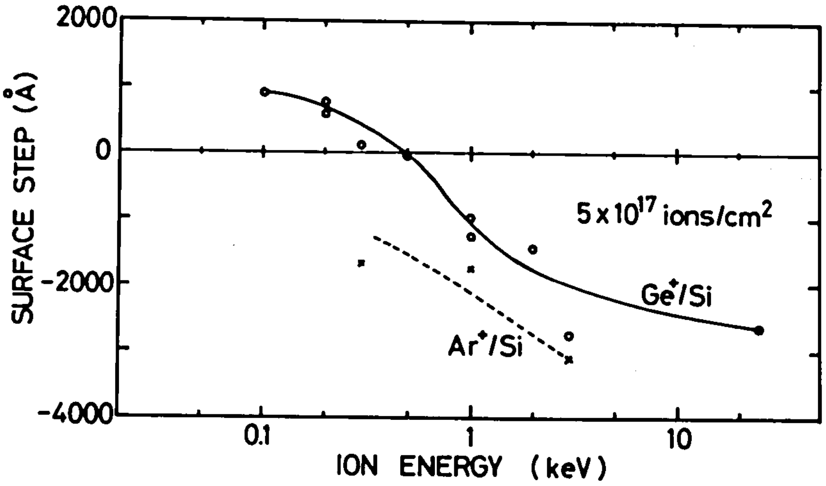

Fig. 3.1 Deposited film thickness or etched substrate depth as a a function of incident ion energy. The substrate is a (111) oriented single silicon crystal. Incident ion species are Ge^+ and Ar^+ at doses of 5×10^{17} ions/cm^2.

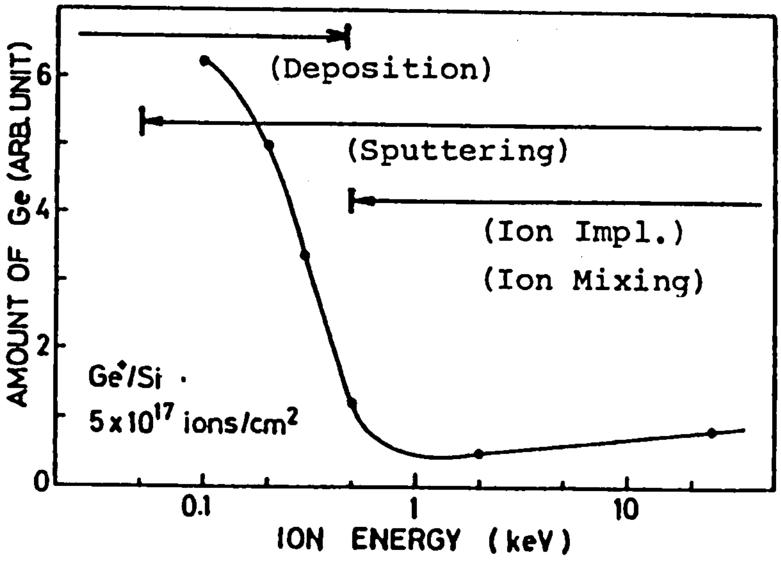

Fig. 3.2 Amount of germanium, measured by XMA, on the surface of a substrate as a function of Ge^+ ion energy at a constant dose of 5×10^{17} ions/cm^2.

incident energy increased. Even at the energy levels above 1 keV, the presence of germanium atoms was still observed. These atoms come from those germanium atoms implanted below the sputter-etched silicon substrate surface. An increase in the amount of germanium in the higher energy range(10 keV) also supports this interpretation.

These results indicate that the incident ion energy at which material buildup will occur is apparently related to self-sputtering. Table 3.2 shows the critical energies at which self-sputterng approaches unity for various incident ions[20,28].

Table 3.2 The critical energy of ions for film build-up.

(Fontell and Arminen [28])

Ion species	Critical energy (keV)
Fe^+	1.5 –2.0
Co^+	1.0 –1.5
Ni^+	0.8 –1.0
Cu^+	0.3 –0.4
Zn^+	0.3 –0.4
Sn^+	0.45–0.5

3.3 Interface Formation by Ion Induced Atomic Mixing

3.3.1 Introduction

In thin film formation, the physics of the interface is very important, from a practical point of view, because film adhesiveness and electrical properties depend on interfacial structures. In thin film formation techniques using ion or plasma methods, the deposited atoms and the substrate atoms are considered to be mutually mixed by ion bombardment at the interface during deposition. However, there has been few reports in which the interfacial structures of ion beam deposited films have been investigated in detail.

In this section the atomic mixing effects of ion beam deposited films are discussed and the thicknesses of interdiffused layers are obtained as a function of ion energy.

3.3.2 Experimental

The experiments were carried out using the IBD machine described in Chapter 2. $^{28}Si^+$ ion beams at ion energies of 50, 100, 200, 300, and 500 eV were deposited onto Al substrates at room temperature. The substrates were each 50 mm x 50 mm and had thicknesses of 30 μm. The ambient vacuum pressure during deposition was 5×10^{-8} Torr. with a deposition rate of about 1 Å/sec and an ion current of 100 μA. The diameter of the ion beam on the substrates was 8 mm. Therefore, the inclusion of residual gas atoms could be neglected. Deposition time of 30 to 60 minutes were necessary to obtain silicon films around 500 - 8000 Å thick.

The composition profiles of the deposited films were analysed by SIMS (Secondary Ion Mass Spectroscopy) using oxygen as the primary ion beam. The etching speed of the deposited film was calibrated by measuring the depth of the etched crater with a Dektak depth monitor which gave an etching speed of 0.6 Å/sec.

3.3.3 Results and Discussion

Figure 3.3 (a) and (b) show the secondary ion mass spectra of the IBD deposited silicon film and the Al substrate, respectively. It can be seen that the Al substrate contains mainly ^{27}Al and the amount of ^{28}Si included is very small. The IBD deposited silicon film were isotopically enriched with ^{28}Si atoms. No isotopes of ^{29}Si and ^{30}Si were recorded.

Figure 3.4 shows a typical depth profile for ^{28}Si and ^{27}Al in IBD films deposited at an ion energy of 100 eV.

Depth-profiles for the IBD deposited films at ion energies of 50, 100, 20, 300 and 500 eV are shown in Fig. 3.5. All curves are normalized in intensity to coincide at the crossing point of the ^{28}Si and ^{27}Al profiles.

It was found that Si atoms and Al atoms interdiffused with each other in the interface layer. Thus, although there is ambiguity in SIMS profiling analysis due to knock-on effect, these curves show that the thickness of the interdiffused layer depends on the ion energy. Therefore, Fig. 3.5 seems to indicate that inter-atomic mixing is enhanced by increased ion

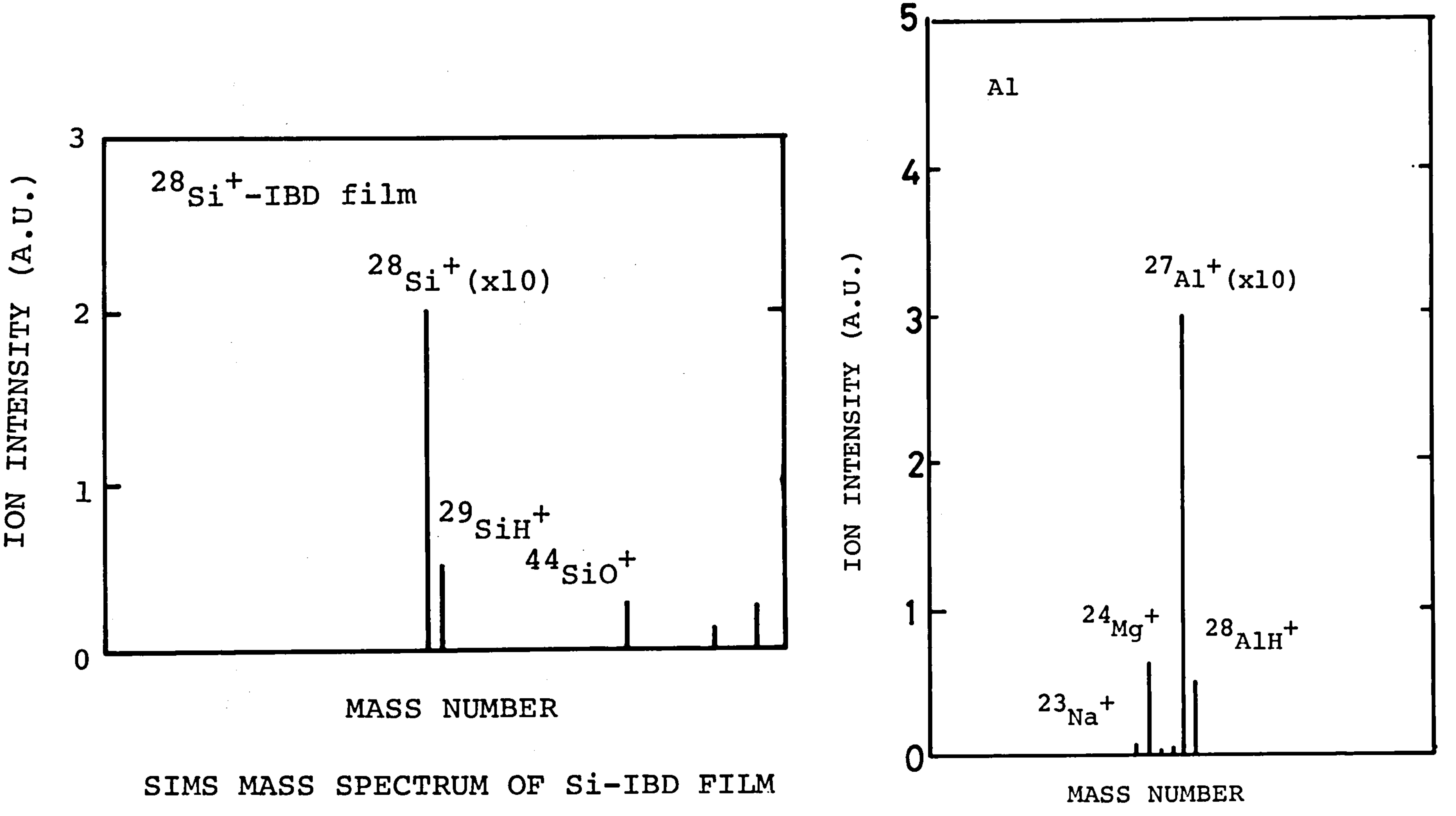

SIMS MASS SPECTRUM OF Si-IBD FILM

SIMS MASS SPECTRUM OF ALUMINUM SUBSTRATE

Fig. 3.3 SIMS mass spectra for (a) Si-IBD film on an Al substrate and (b) Al substrates.

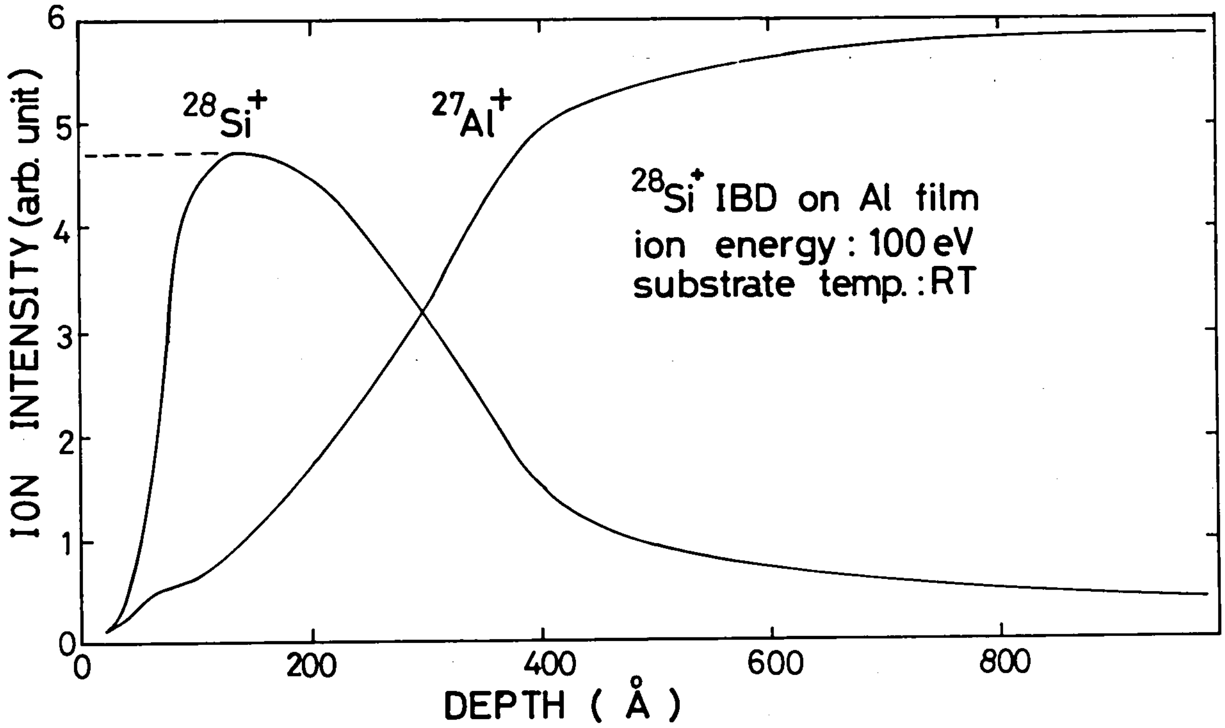

Fig. 3.4 SIMS depth profile of a Si-IBD film on an Al substrate at an ion energy level of 100 eV.

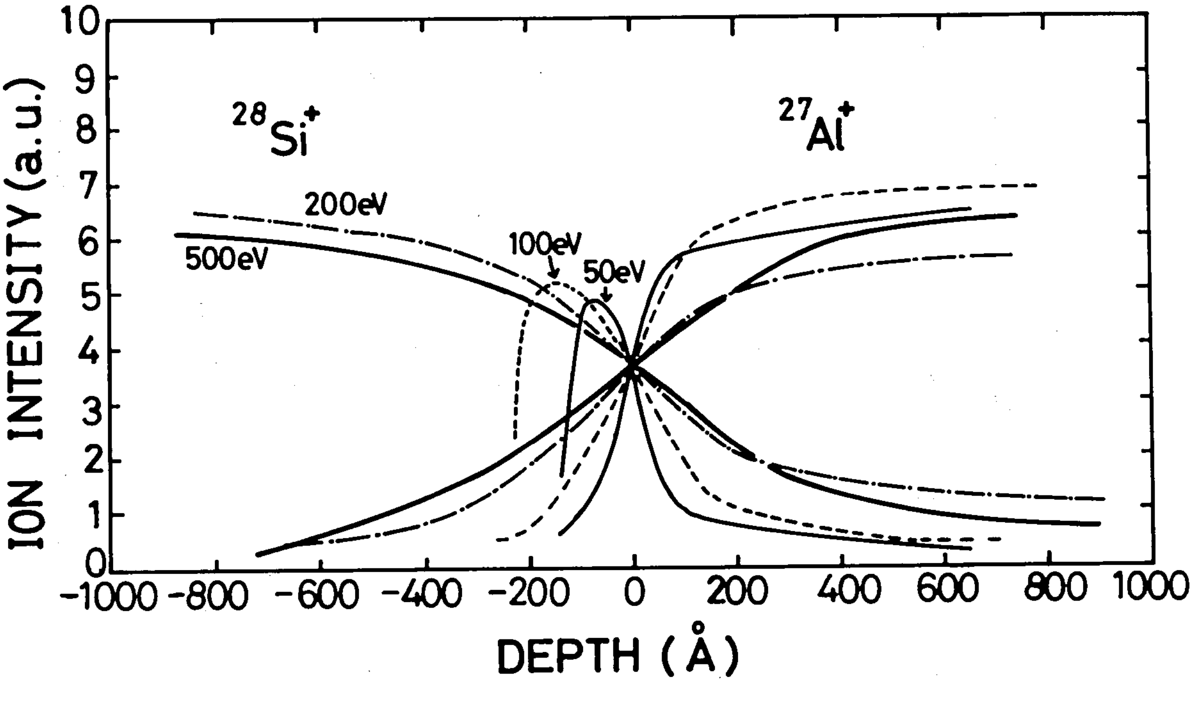

Fig. 3.5 SIMS depth profiles of ^{28}Si ion beam deposited films on Al substrates at ion energy leverls of 50, 100, 200, and 500 eV.

bombardment. With the thickness of the interdiffused layer as defined in Fig. 3.6, the energy dependence of the interface thickness obtained was shown in Fig. 3.7. The depth profile of a vacuum deposited Al film on a Si substrate at a vacuum pressure of 10^{-9} Torr is shown in Fig. 3.8, for reference.

The interface layer thickness of the IBD films is in the order of several hundred angstroms, while that of vacuum deposited films is less than 50 angstroms. (The rather large value is due to limitation in SIMS measurement.) This thick interface layer may be explained by considering that the top few angstroms amounting to the penetration depth of the incoming ions, are steadily intermixed with those ions throughout the deposition period. Therefore, the integration of succesive interdiffused layers produces this relatively thick interface region. The existence of this thicker interface region in IBD deposited films is thought to accout for the strongly adherent film formation found in ion plating and ion beam deposition methods.

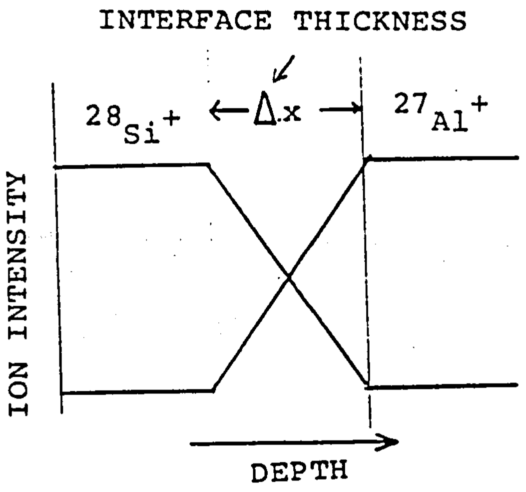

Fig. 3.6 Definition of "interface thickness"

Tsukizoe and Ohmae reported on the interatomic mixing effects in Ag^+ IBD films on Cu crystals substrates[23]. They also pointed out the large interdiffused layers. However, the energy dependence of layer thickness does not qualitatively agree with the present results.

I. Yamada et al.[29] and D.G. Teer et al.[30] reported the interdiffused layer thicknesses to be in the order of several hundred angstroms in ionized cluster beam deposition and ion plating, respectively. Their results are in good agreement with the data obtained in this study.

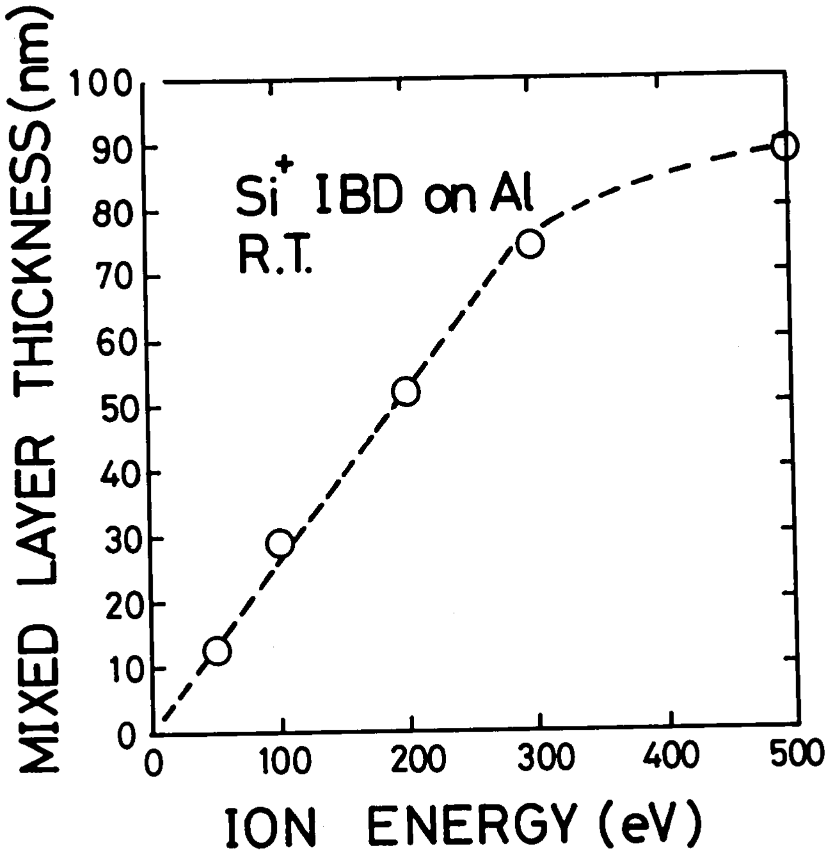

Fig. 3.7 Energy dependence of interface thickness for Si ion beam deposited films.

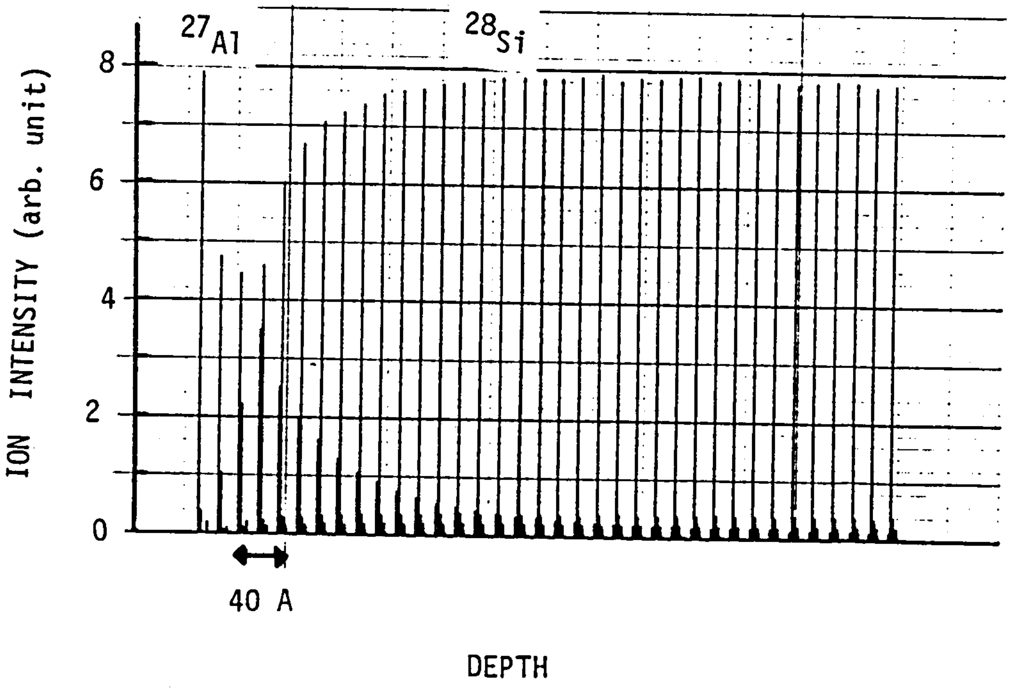

Fig. 3.8 SIMS depth profile of a UHV vacuum deposited Al film on a Si substrate.

3.3.4 Conclusions

Ion induced atomic mixing effect in ion beam deposition has been demonstrated. The thickness of the interface layer is in the order of several hundred angstrom and increases with the level of incoming ion energy. The formation of these interdiffused layers at low temperature seems to be the reason why strongly adherent film can be formed by ion beam deposition and ion plating.

3.4 Germanium and Silicon Ion Beam Deposition on Si(100)

3.4.1 Introduction

Low-temperature thin film formation techniques using plasma or ion beams have been attracting a great deal of interest in the field of electronic and optical device fabrication[1]. Films made by these methods have strong adhesion, surface smoothness, controllability of crystalline orientations, etc.. There is also the possibility of low temperature epitaxial growth of semiconductor materials[20]. Ion plating[30,31], ionized cluster beam deposition[26], and plasma deposition[32,33,34] are examples of these approaches.

Recently, there have been several reports of mass-separated ion beam deposition(IBD) on various materials[11-23]. For example, Yagi et al.[20] have reported deposition of Ge^+ and Si^+. Low temperature epitaxial growth has been observed for many materials, though not for silicon. Silicon deposition in our previous work was not successful. The films obtained were amorphous because they were made in a poor vacuum.

In this section, after briefly describing the experimental conditions, we will discuss in detail the crystalline characterizations of the Ge^+/Si hetero-epitaxial and Si^+/Si homo-epitaxial films.

3.4.2 Experimental

The IBD system used in this study is schematically shown in Fig. 2.5 of Chapter 2. The system consists of three principal parts: an ion source, a mass-separation magnet, and a UHV deposition chamber. Ge^+ and Si^+ ion beams are generated from $GeCl_4$ and $SiCl_4$ gas discharges, respectively, in a Freeman-type source and extracted at an energy level of 10 to 30 keV. After mass separation using a 60° sector-type magnet, the ion beam is deflected toward the horizontal focal point of the magnet by electrostatic deflectors to prevent target irradiation by charge-exchanged high energy neutral particles. The ion beam is then decelerated to an energy of 100 to 200 eV by an E x B type lens system.(see Section 2.4.) The diameter of the deposited region is from 7 to 10 mm. A typical mass-spectrum of decelerated ion beams for $GeCl_4$ gas discharge is shown in Fig. 3.9. An ion current range from 50 to 200 μA for Ge^+ and Si^+ ion beams was obtained.

The silicon substrates to be deposited were (100) oriented single crystals 20 mm x 20 mm x 0.3 mm, which were mounted on heating blocks on a sample manipulator. Before deposition, the silicon substrates were cleaned using conventional cleaning procedures. Neither flash desorption nor Ar^+ ion sputter cleaning was carried out. The base pressure in the chamber was 5×10^{-10} Torr after 8 hours of mild bakeout. During ion beam deposition the ambient vacuum pressure increased to 5×10^{-8} Torr due to the gas load from the ion source.

The substrate temperature was monitored by a Pt,Pt-Rh thermocouple immersed in the heating block, and the ion current flowing through the substrate was recorded by a current monitor during deposition. The thicknesses of the deposited layers were a few hundred angstroms for the Ge^+/Si films and 2000 to 3000 angstrom for the Si^+/Si films. The experimental conditions for Ge^+ and Si^+ ion beam deposition are summarized in table 3.2 and 3.3.

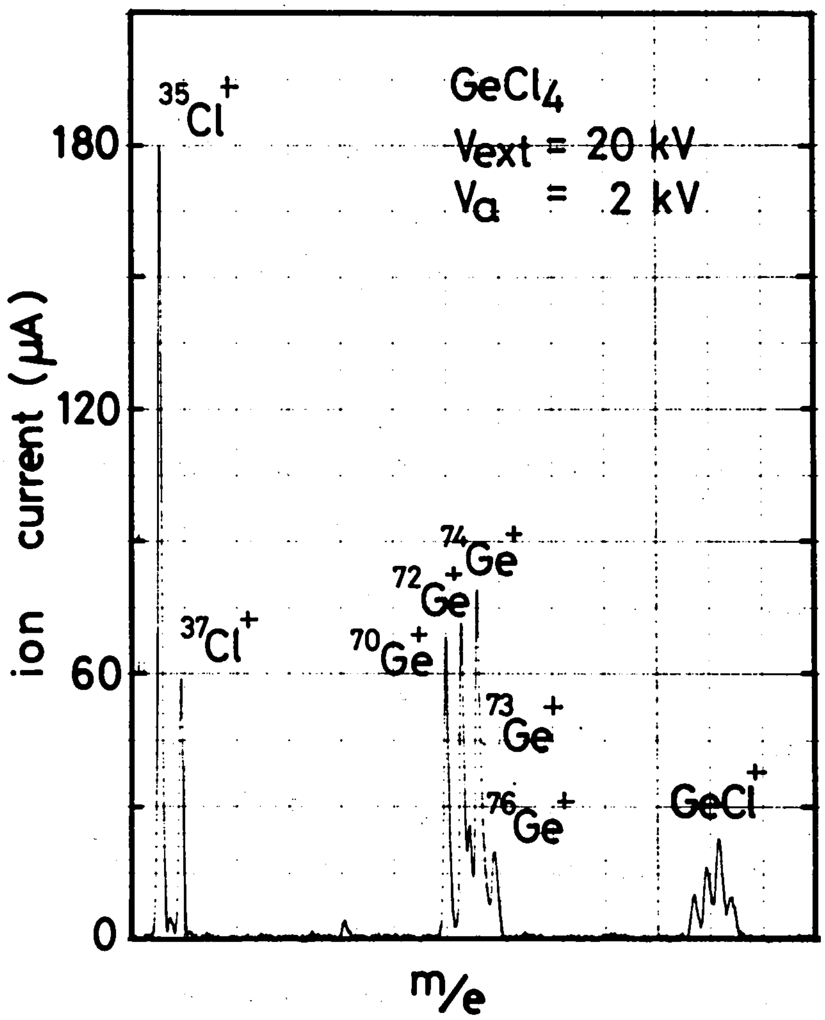

Fgi. 3.9 Typical mass-spectrum of decelerated ion beams generated by $GeCl_4$ gas discharge.

Table 3.3 Experimental conditions for germanium ion beam deposition.

INCIDENT ION SPECIES : $^{74}Ge^{+}$
INCIDENT ION ENERGY : 100 eV
BEAM SPOT SIZE : 8 ~ 10 mm in dia.
ION CURRENT DENSITY : >100 µA/cm^2
DEPOSITION TIME : 60 min.
SUBSTRATE : Si(100) single crystal
SUB. TEMPERATURE : 300 °C
VACUUM PRESSURE : 1×10^{-7} Torr

Table 3.4 Experimental conditions for silicon ion beam deposition.

INCIDENT ION SPECIES : $^{28}Si^{+}$
ION ENERGY : eV_a= 200 eV
BEAM SPOT SIZE : 8 - 10 mm in dia.
ION CURRENT DENSITY : J_i= 100 µA/cm^2
(ION FLUX DENSITY : $\Gamma_i = 6.3 \times 10^{14}$ ions/cm^2·sec)
DEPOSITION TIME : T= 30 - 60 min.
SUBSTRATE : Si(100) single crystal
SUB. TEMPERATURE : T_s= 600°C
FILM THICKNESS : about 5000 Å
DEPOSITION RATE : about 3 - 6 Å/sec
VACUUM PRESSURE : 5×10^{-8} Torr

3.4.3 Results and Discussion

(a) $^{74}Ge^+/Si$ hetero-epitaxial growth

Fig. 3.10 shows the TEM diffraction pattern for the Ge^+/Si hetero-structure. Here, Ge^+ ions were deposited at 100 eV. The substrate temperature was 300°C and the vacuum pressure was 1×10^{-7} Torr. Perfect epitaxial relationship between the deposited germanium lattice (a=5.66 Å) and the substrate silicon lattice (a=5.43 Å) are clearly indicated by the two sets of spots observed.

The crystalline structure for the germanium deposit is shown to be rather defective by this TEM micrograph. Moire patterns were observed in the micrograph and fringe spacing was in good agreement with that deduced from the lattice constant difference. Many small dislocation loops were also found. Since the substrate temperature is not high enough for solid phase epitaxial growth to occur, ion bombarded surface disorders cannot fully recover and are thought to develop into these defects. The amount of lattice mismaching between Ge and Si is thought to be another reason for these defects.

The same structure was examined using Rutherford back-scattering measurements with the results shown in Fig. 3.11. The low yield for the aligned spectrum indicates a good epitaxial relationship. However, the yield from the interface region shows some kind of interatomic mixing or alloy phase formation between the Ge and Si.

The surface smoothness of the deposited germanium film was examined using an electron microscope. The surface replica micrograph shown in Fig. 3.12 indicates a very flat surface structure.

The hetero-epitaxial growth of germanium on silicon (111) substrates has been reported in a previous paper[20] for epitaxial temperature as low as 300°C at an ion energy of 100 eV. The present results are extensions of those found previously to Si(100) substrates. Recently, Kuiper et al.[34] reported that germanium epitaxial growth is possible at 230°C using ionized cluster beam deposition in which the average kinetic energy per atom was as low as 1 eV. Further investigations are necessary to understand the effects of ion bombardment energy on crystalline structure.

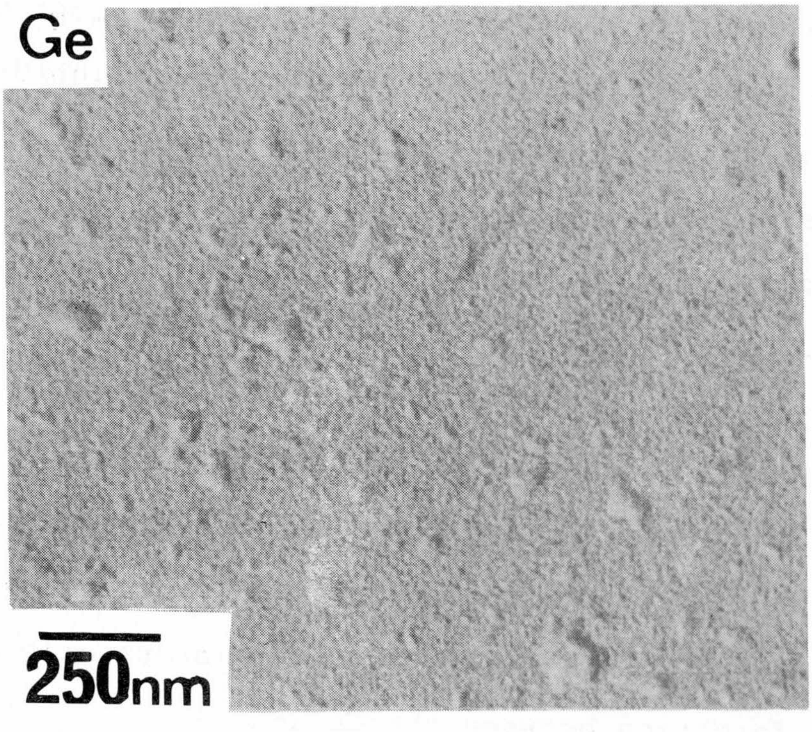

Fgi. 3.12 Surface replica micrograph of a Ge^+/Si film.

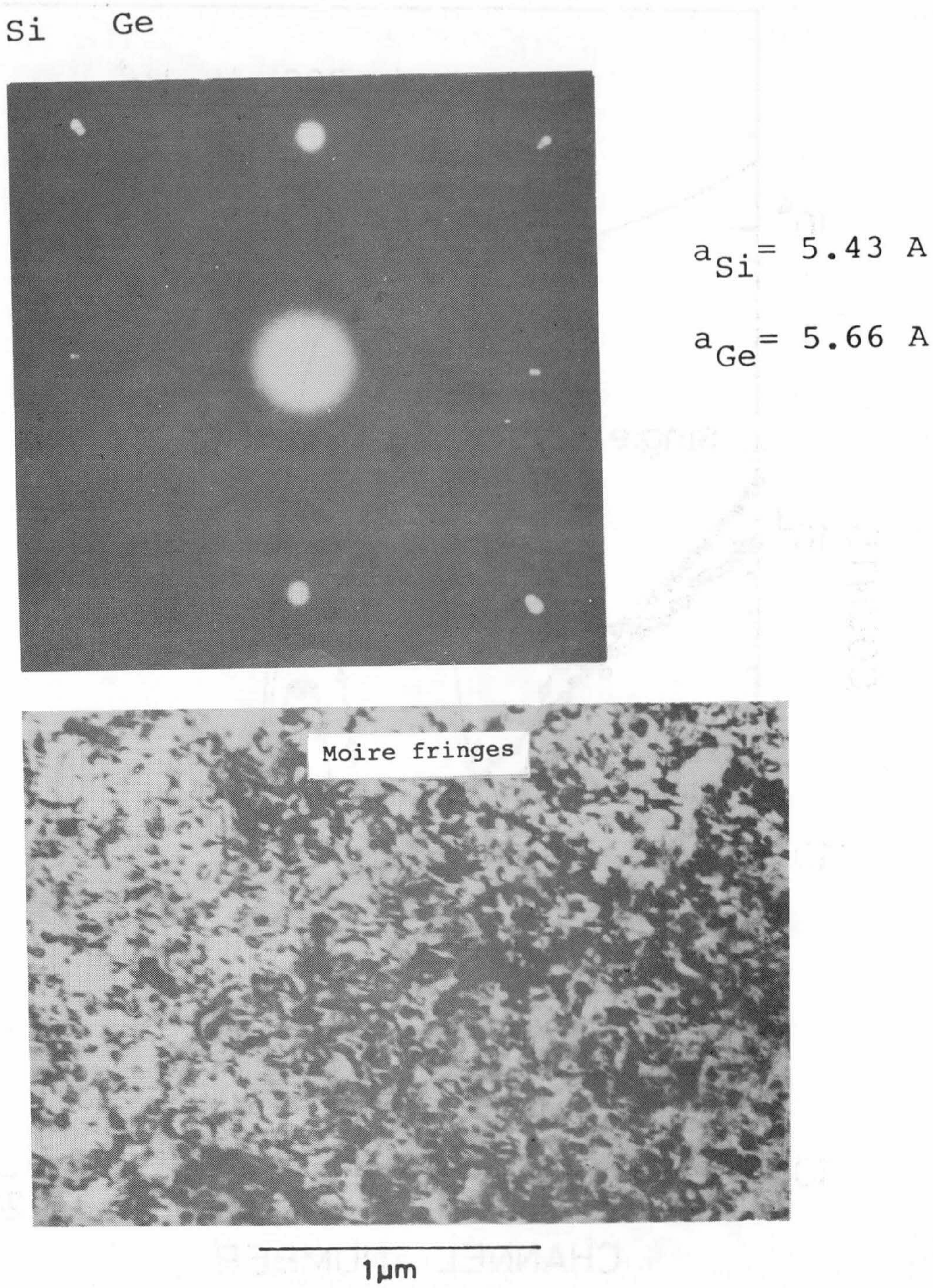

Fig. 3.10 Transmission electron diffraction pattern for germanium deposited on a Si(100) substrate. The ion kinetic energy is 100 eV, and the substrate temperature is 300°C.

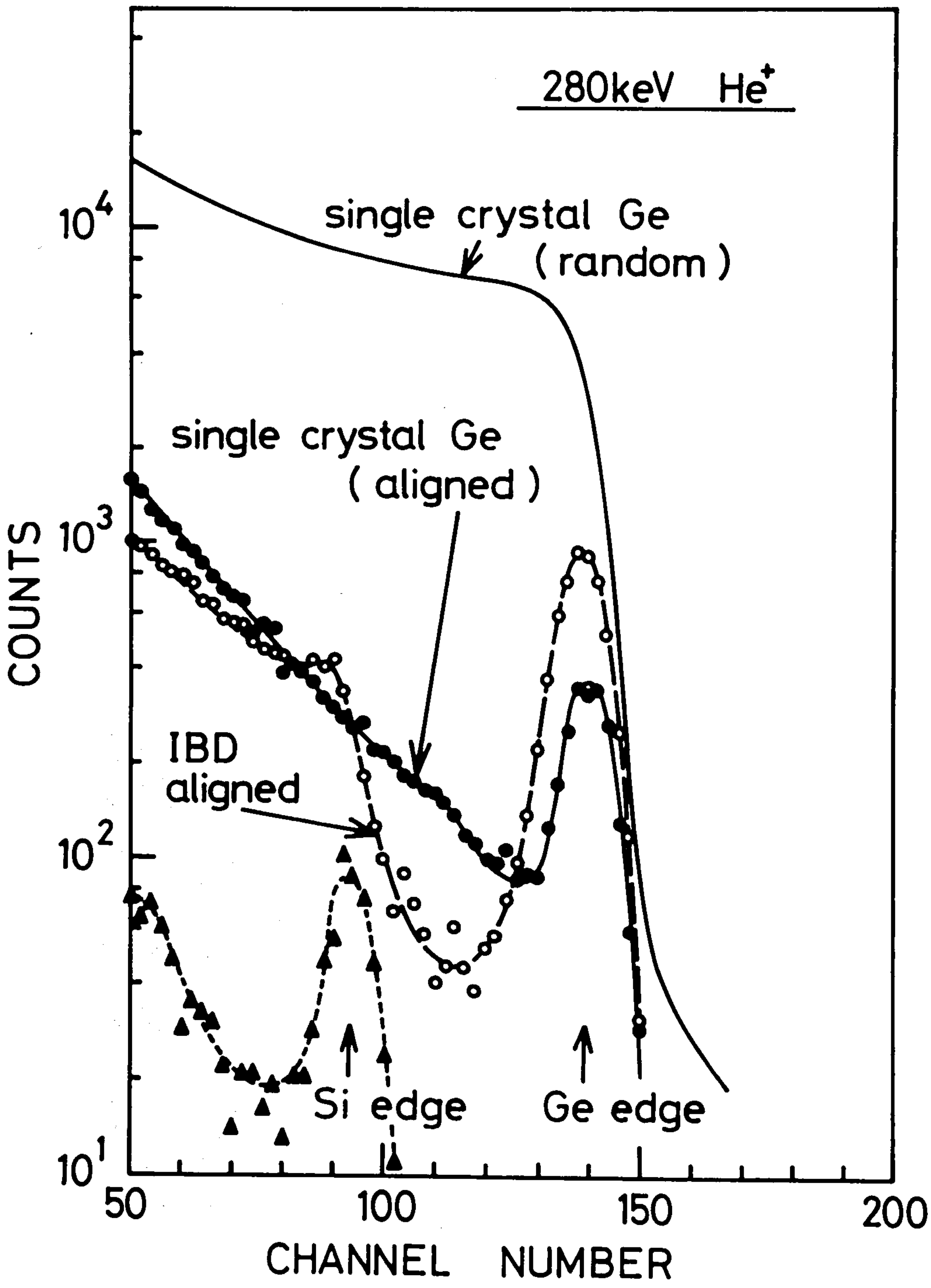

Fig. 3.11 Rutherford back-scattering spectrum for germanium deposited films. Deposition conditions are the same for in Fig. 3.10.

(b) $^{28}Si^+/Si(100)$ homo-epitaxial growth

Si^+ ion beam deposition was carried out using the procedure described above. The ion acceleration energy was 200 eV and the ambient vacuum pressure during deposition was 5×10^{-8} Torr.

SIMS mass spectra for the silicon deposited films and the silicon substrates are shown in Fig. 3.13 (a) and (b), respectively. It should be noted that the IBD films contain only a single isotope of ^{28}Si. That is, the films are isotopically enriched. Carbon content included in the film was very small compared with previous results on silicon IBD films where vacuum pressure was 1×10^{-5} Torr and ion current was 5 μA.

The films deposited at room temperature were amorphous, as shown in the RHEED pattern in Fig. 3.14. As the substrate temperature was increased to 600°C, (110) preferentially oriented polycrystalline films were obtained. At a substrate temperature of 740°C, the deposited films exhibited a single crystalline in structure, as shown in the RHEED patterns in Fig. 3.15. The azimuthal directions of the probe electron beam were (a) <001> and (b) <011>. The three major spots in Fig. 3.15, which originate from the [220], [2$\bar{2}$0], and [400] planes, indicate that the deposited layer is grown epitaxially from the Si(100) substrate. The weak spot patterns suggest the existence of twin structures.

The same epitaxial structure was also examined by TEM. The transmission electron diffraction pattern, as shown in

Fig. 3.16, indicates homo-epitaxial growth. The sets of small spots around the major ones indicate that twin structures are included in the deposited layer. The crystalline structure is rather defective and contains a lot of dislocation loops.

In silicon deposition, surface contamination from oxygen or carbon plays an important role in epitaxial growth[36,37]. In this study, surface contamination on a silicon substrate was not completely removed before deposition. In a previous report[20], silicon ion beam deposition was carried out at a vacuum pressure of 1×10^{-5} Torr. At that pressure the impinging rate of residual gas atoms on the silicon surface was two orders higher than the bombarding ion flux. Therefore, the as-deposited films were always amorphous. However, in these experiments, the impinging rate of Si^+ ions is two orders or more higher than the residual gas atom flux. The epitaxial growth of silicon is thought to result from these improvements in vacuum pressure and ion current flux.

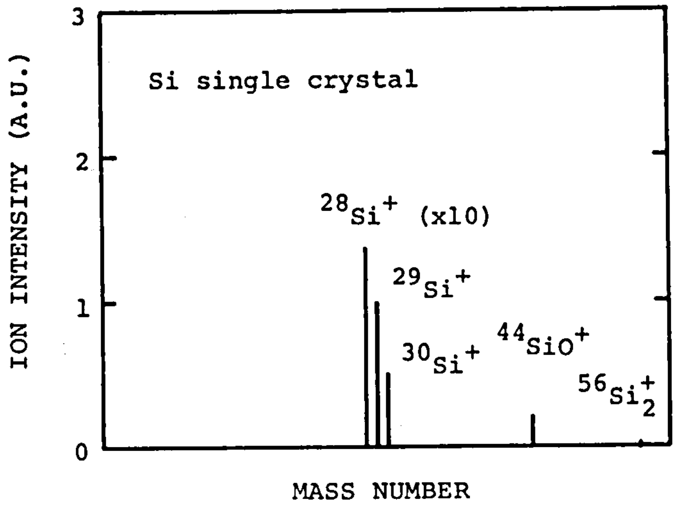

SIMS MASS SPECTRUM OF SILICON SUBSTRATE

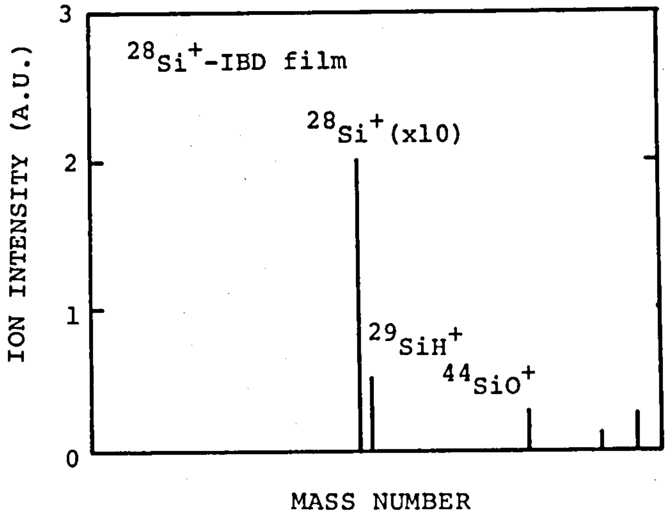

SIMS MASS SPECTRUM OF Si-IBD FILM

Fig. 3.13 SIMS mass spectra of (a) a $^{28}Si^{+}$ ion beam deposited fil

and (b) a silicon substrate.

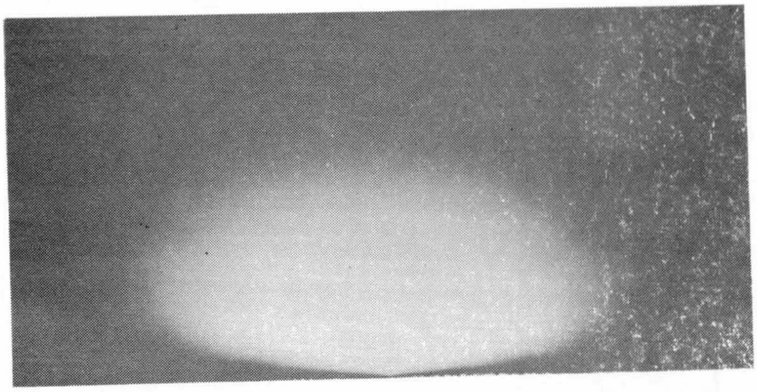

Fig. 3.14 RHEED pattern of a Si^+/Si IBD film deposited at room temperature.

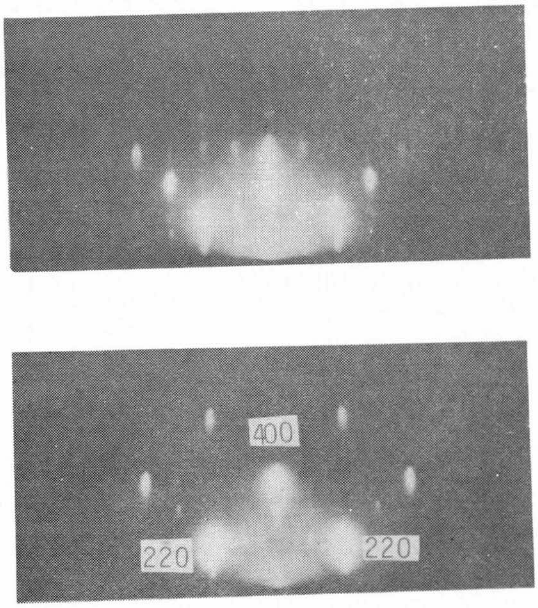

(b)

Fig. 3.15 RHEED patterns of Si^+/Si IBD films deposited at 740°C. The ion kinetic energy was 200 eV and azimuthal direction of the probe electron beam was (a) <001> and (b) <011>.

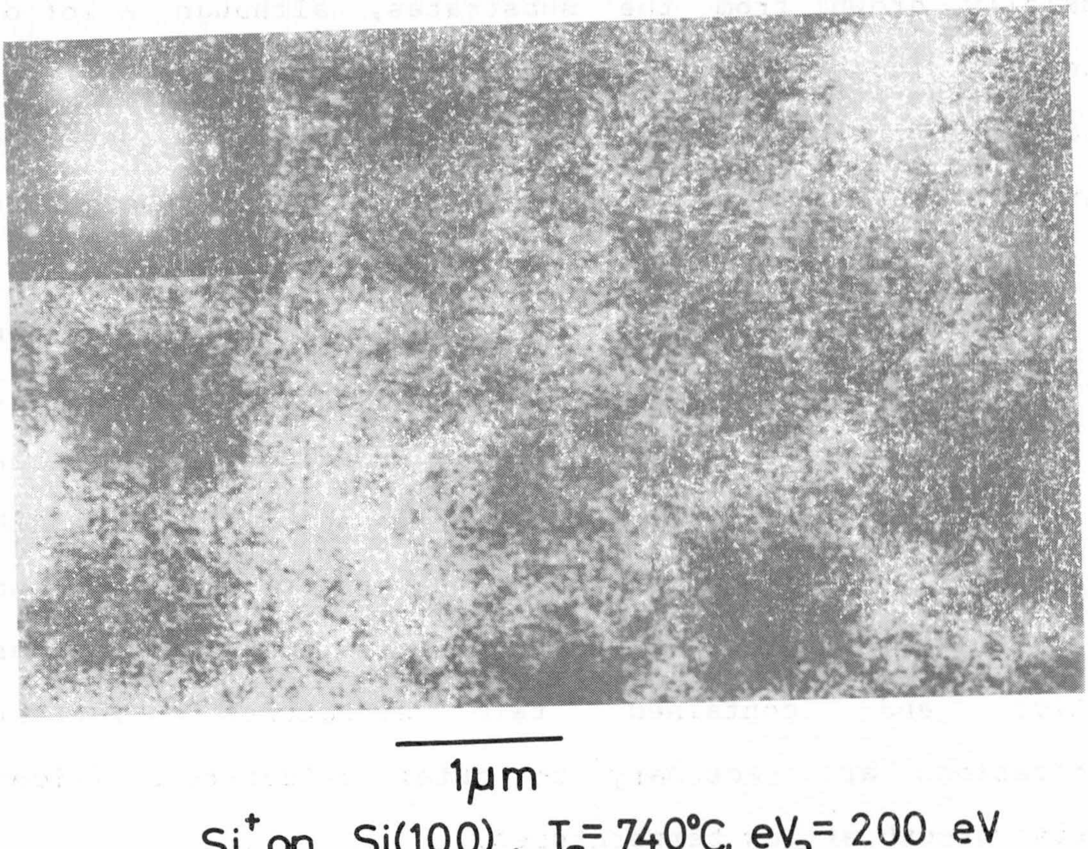

Fig. 3.16 Transmission electron micrograph for a Si$^+$/Si(100) IBD film deposited at 740 C where ion kinetic energy is 200 eV.

3.4.4 Conclusions

Germanium and silicon films were epitaxially grown on Si(100) substrates by low-energy, mass-separated ion beam deposition. Germanium films deposited at 300 °C were epitaxially grown from the substrates, although a lot of dislocation loops were found in the deposited layer. Large lattice mismatching between Ge and Si, and low substrate temperature for solid phase epitaxial growth are thought to have resulted in those defects.

Silicon films, composed of $^{28}Si^{+}$ ions deposited at an ion energy of 200 eV and a substrate temperature of 740 °C, were isotopically enriched with a single species of ^{28}Si. The crystalline structure, observed by means of RHEED and TEM measurements, indicated that the films were epitaxially grown on Si(100) substrates. However, the films were rather defective and contained twin structures. Further investigations are necessary to obtain defect-free silicon epitaxial growth at low temperatures.

3.5 Summary

In this chapter the fundamental aspects of deposition of low-energy, mass-separated metal ions were discussed. It was shown that irradiation of low-energy metal ions causes simultaneous deposition, sputtering and implantation. The relative contribution of these three to thin film growth was shown to depend on the bombarding ion energy.

The strong adhesiveness of the ion beam deposited films was shown to be related to the thick interdiffused interface layer. This layer, whose thickness is in the order of several hundred angstroms, is formed by ion induced atomic mixing.

It was demonstrated that relatively low-temperature epitaxial growth is possible using this ion beam deposition method. Hetero-epitaxial growth of germanium on a silicon singly crystalline substrate was obtained at an ion energy of 100 eV and a substrate temperature as low as 300° C. Homo-epitaxial growth of silicon was also possible at an ion energy of 200 eV and a substrate temperature of 740° C. The crystalline structure of these ion beam deposited films were also discussed in detail.

88 項欠

Chapter 4. REACTIVE ION BEAM ETCHING

4.1 Introduction

Plasma etching has commonly been recognized as an essential technology for the fabrication of highly integrated semiconductor devices. In particular, reactive ion etching (RIE) and microwave plasma etching have been successfully utilized in microfabrication processes due to their anisotropic etching characteristics[1,2]. However, little theoretical or quantitative knowledge has been available on the plasma etching mechanisms.

Many attempts[2-4] have been carried out to determine the plasma etching mechanisms by exploiting the plasma or reactive ion beam etching apparatus. However, in plasma etching, it is not so easy to independently control the individual etching parameters. Such parameter include the species of reactive particles (ions or radicals) and their kinetic energies and fluences, etc.. This is because these parameters are complicated functions of the discharge conditions (gas species, pressure, power, etc.). Therefore, the "beam method", which is familiar in atomic and molecular physics, seems more promising than the "plasma method" for the study of etching mechanisms.

Recently, Coburn et al.[5] investigated the etching mechanisms for silicon and silicon dioxide using fluorocarbon ion beams in a UHV apparatus. They bombarded non-mass-analyzed reactive fluorocarbon ions onto Si and/or SiO_2 surfaces and observed the ion-irradiated surface layers using AES (Auger Electron Spectroscopy) and XPS (X-ray Photoemission Spectroscopy). They pointed out that the ion-bombarded silicon surface is covered with carbon, the amount of which depends on the ion kinetic energy, ion dose, and the existence of oxygen in the target.

Coburn also pointed out that an ion-assisted chemical reaction occurs when silicon is exposed to XeF_2 gas and simultaneous argon ion bombardment[6]. Y.Y. Tu reported that 25 or more silicon atoms are removed per incident argon ion by these ion-assisted chemical reactions[7].

The etching probability for neutral active species has recently been reported by Chen[8] for silicon using F_2 and by Flamm et al.[9] for silicon dioxide using F* radicals. These etching probabilities have been found to be in the order of from 10^{-6}(Chen) to 10^{-4}(Flamm).

In practical applications, reactive ion beam etching(RIE) has been of interest because it produces little undercutting[10]. In RIE, the energetic reactive ions are thought to take a primary role in the etching process. Therefore, it seems necessary to investigate the role of individual reactive ion bombardment during etching.

In this section, a low-energy, mass-analysed reactive ion beam etching(RIBE) apparatus and a mass-spectroscopic method for measurement of the chemical sputtering yields of crystalline silicon are presented. Then, a quartz-oscillator microbalance (QCOM) method for measuring the total sputtering yield of silicon from reactive fluorocarbon ion bombardments is presented. Finally, quantitative discussion on the physical and chemical roles of reactive ion bombardment, especially the energy dependence of these two sputtering yields, is presented.

4.2 Chemical Sputtering Yields of Silicon

4.2.1 A Low-energy, Mass-separated Reactive Ion Beam Etching Apparatus

The low-energy, mass-separated reactive ion beam (RIBE) apparatus used for this study is, in principle, the same as the ion beam deposition (IBD) machine[10] described in Chapter 2. The RIBE system consists of an ion source, a mass-separation magnet and an ultra-high vacuum (UHV) chamber equipped with a quadrupole mass filter (QMF, UTI-100C).

To produce the ion beams (F^+, CF^+, ${CF_2}^+$, ${CF_3}^+$), CF_4 or C_3F_8 gas is fed into a hot-cathode, arc-type ion source. Ions are extracted from the ion source at an extraction energy, eV_{ext}, of 10 keV and mass-analysed using a 60°sector-type magnet. The mass-selected ion beam, for example $^{19}F^+$ at a kinetic energy of 10 keV is decelerated in the UHV chamber by an E x B type ion decelerator[12] and bombards a crystalline silicon target located in the center of the UHV chamber. The ion bombarding energy is determined by the ion acceleration voltage, V_a, and can range from 100 to 3000 eV. The energy spread for the decelerated ion can be as large as 100 eV. The target ion current during etching is simultaneously recorded by a current monitor.

A typical mass spectrum for a decelerated ion beam generated by CF_4 gas discharge is shown in Fig. 4.1. Isotopically pure ion beams, such as $^{19}F^+$, $^{31}CF^+$, $^{50}CF_2^+$, $^{69}CF_3^+$, were obtained with good mass resolution in the current range of 50 to 100 μA. The chemical reaction of CF_4 plasma with the boron nitride insulators used in the ion source produced $^{30}BF^+$, $^{49}BF_2^+$, and $^{28}N_2^+$ ion beams. The area under ion bombardment was about 10 mm in diameter.

The RIBE system was differentially pumped at four pumping ports to keep the etching chamber in a UHV condition. The base pressure in the chamber was 5×10^{-10} Torr after 8 hours of mild bakeout with the isolation gate valve closed. During ion beam etching, the vacuum pressure increased to 10^{-8} Torr because of the gas load from the ion source.

Samples used were n-type, (100) oriented crystalline silicon wafers with a carrier concentration of 1×10^{17} cm^{-3}. As shown in Fig. 4.2, the target was tilted 30° normal to the incident ion beam to protect against the sputtered, high-energy silicon atoms hitting the QMF. The substrate was at room temperature.

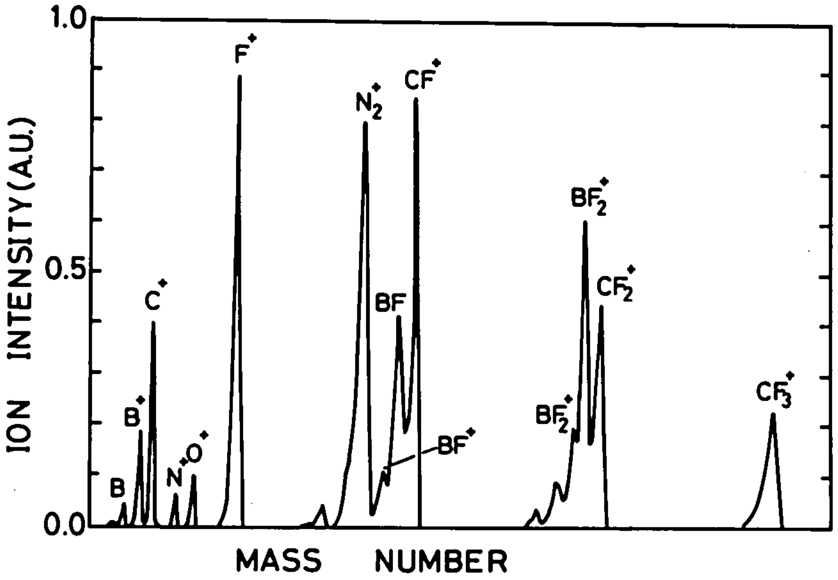

Fig. 4.1 Typical mass spectrum for an ion beam generated by CF_4 gas discharge. The ion extraction voltage is 10 kV and the final kinetic energy of the decelerated ion beam is 1 keV.

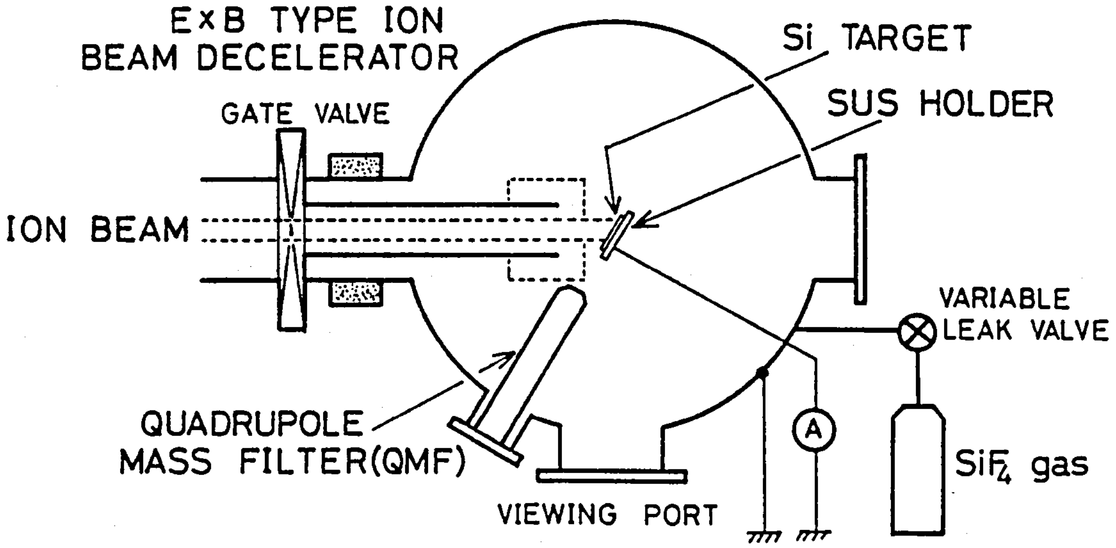

Fig. 4.2 Silicon target arrangement for gas analysis in the UHV chamber.

4.2.2 Principle of Chemical Sputtering Yield Measurement by Mass-spectroscopic Analysis.

In reactive ion beam etching carried out in a UHV environment, total silicon mass reduction can be considered to consist of both physical sputtering and evaporation in the form of a volatile gas through chemical reaction. The quartz crystal microbalance method used by Coburn et al.[5-7] can give the amount of total sputtering. Here, however, the interest is the amount of chemically sputtered silicon. Thus, "mass-spectroscopic analysis" is investigated as a way to detect only the amount of the chemically sputtered silicon.

Here, it is assumed that silicon atoms leave the silicon surface mainly in the form of volatile gas (SiF_4) through a chemical reaction which can be expressed as

$$Si + 4F \longrightarrow SiF_4 \uparrow \qquad (4.1)$$

No other intermediate molecules, such as SiF_n (n=1,2,3) are assumed to desorb from a silicon surface[7]. The product gas, SiF_4, is considered to be rapidly thermalized in the etching chamber. In the steady state, the rate of gas product formation, Φ_{SiF_4} (molecules/sec), can be determined by the partial pressure of SiF_4, p_{SiF_4}, in the chamber through the relationship,

$$\Phi_{SiF_4} = kT \cdot S_p \cdot p_{SiF_4} \quad , \qquad (4.2)$$

where S_p denotes the pumping speed for SiF_4, k, a Boltzmann constant, and T, the gas temperature.

The partial pressure of SiF_4 can be measured from the $^{85}SiF_3^+$ ion intensity, $I_{SiF_3^+}$, at the QMF.

Employing all these assumptions, the chemical sputtering yield, Y_C, for silicon resulting from reactive ion beam bombardment can be obtained

$$Y_C = \frac{\Phi_{SiF_4}}{I_i/e} = \alpha \cdot \frac{I_{SiF_3^+}}{I_i} , \qquad (4.3)$$

where I_i is the incident ion current and e the electronic unit charge. The value of α is 0.25 under the experimental conditions presented here.

The reaction probability for (1) denoted by ε can be defined by considering that one silicon atom is removed by four fluorine atoms as:

$$\varepsilon = \frac{4Y_C}{n} , \qquad (4.4)$$

where n denotes the number of fluorine atoms included in the incident ions.

The partial pressure of SiF_4 was measured using the QMF. The mass pattern for SiF_4 fragmentation was obtained as a function of the SiF_4 partial pressure by leaking a small amount of SiF_4 gas into the chamber through a slow variable leak valve. At the same time, the total amount of the leaked gas was measured using a B-A gauge.

No real distinction between the mass peaks for $^{28}Si^+$ and $^{28}CO^+$ was possible in the quadrupole mass filter due to its limited mass resolution capability (< 300). Therefore, care was exercised during the examination to change irradiation conditions so as to separate the signals originating from $^{85}SiF_3^+$ from those issuing from $^{85}COF_3^+$.

The etching probability of silicon and stainless steel by BF_2^+ and by F^+, CF_2^+ ion bombardments, respectively, were also measured using the same procedure.

4.2.3 XPS Analysis of the Etched Surface.

Silicon surfaces etched by F^+ and CF_2^+ ions were analysed by XPS in a separate apparatus. In order to minimize hydrocarbon contamination, the time the sample was exposed to the atmosphere was made as short as possible. The O_{1s} peak was used to calibrate the XPS spectra.

4.2.4 Experimental Results

(a) SiF_4 Cracking Mass Pattern

The mass spectrum of fragmented SiF_4 ions was measured using a QMF for the pressure range from 10^{-9} to 10^{-6} Torr. Four main mass peaks were observed at m/e= 85, 47, 66, and 104. As shown in Fig. 4.3, all of these ion intensities showed linear dependence on SiF_4 gas pressure. The ratio of the four ion peak intensities to each other is 1 : 0.2 : 0.02 : 0.01. This indicates that these mass peaks represent $^{85}SiF_3^+$, $^{47}SiF^+$, $^{66}SiF_2^+$ and $^{104}SiF_4^+$, respectively. Thus, the partial pressure of SiF_4 can be estimated by monitoring the $^{85}SiF_3^+$ ion intensity, which is the largest of the four.

(b) Separation of the $^{85}SiF_3^+$ Ion Signal from $^{85}COF_3^+$ in the QMF Mass Spectrum

Since the mass resolution of the QMF is not sufficient descriminate between $^{85}SiF_3^+$ and $^{85}COF_3^+$, precautions were taken prior to etching measurement. The principal mass peaks included in the residual gas in the UHV chamber were $^{2}H_2^+$, $^{18}H_2O^+$, $^{28}CO^+$, and $^{44}CO_2^+$ when the UHV chamber was connected to the ion beam line. The introduction of CF_4 gas into the ion source added large amounts of fragmented ions at $^{69}CF_3^+$, $^{50}CF_2^+$, and $^{31}CF^+$ in the QMF mass spectrum. Ignition of the arc discharge in the ion source modified the QMF spectra by reducing $^{69}CF_3^+$ ion intensity by a factor of 0.8.

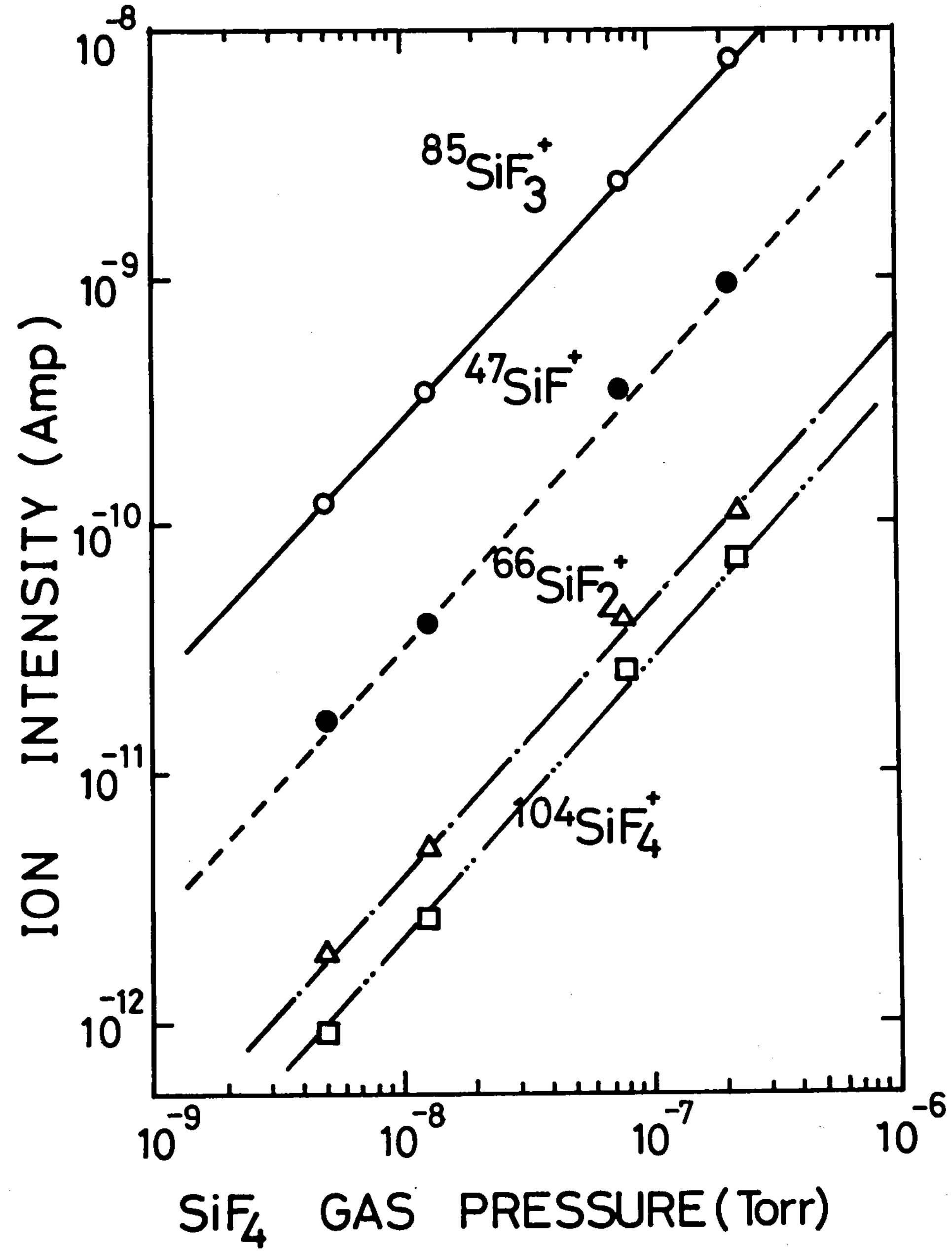

Fig. 4.3 Dependence of the fragmented ion intensities of SiF_4 on gas pressure.

This is a possible indication that some neutral radicals might have been generated in the ion source, and flowed into the etching chamber to react with the solid surface.

The m/e=85 ion intensity was separately compared with ion bombardment on stainless steel(vacuum vessel composition material) and on a silicon surface. Figs. 4.4 and 4.5 show the energy dependence of the m/e=85 ion intensity for F^+, and for CF_2^+ ion bombardments on a stainless steel surface, respectively. At m/e = 85, a constant background level of 10^{-10} Amp. was always detected when F^+ or CF_2^+ ions bombarded the stainless steel surface. On the other hand, in the case of silicon bombardment, the m/e=85 ion intensity linearly depended on the incident ion current for the four ion species: F^+, CF^+, CF_2^+ and CF_3^+, as shown in Fig. 4.6. Here, the ion kinetic energy was 1 keV. Comparing Figs. 4.4 and 4.5 with Fig. 4.6, it can be concluded that the reaction of ^{28}CO molecules adsorbed on a stainless steel surface seems negligible in the measurement of the partial pressure of SiF_4 gas during F^+ or CF_n^+ ion bombardment. This fact enables derivation of the "chemical sputtering yield for crystalline silicon" by formula (4.3).

(c) Energy Dependence of Chemical Sputtering

The energy dependence of the $^{85}SiF_3^+$ ion intensity for the same four reactive ion species are shown in Fig. 4.7. Here the ion current has been adjusted to a constant value (40 μA). It can be seen that these energy dependences differ remarkably

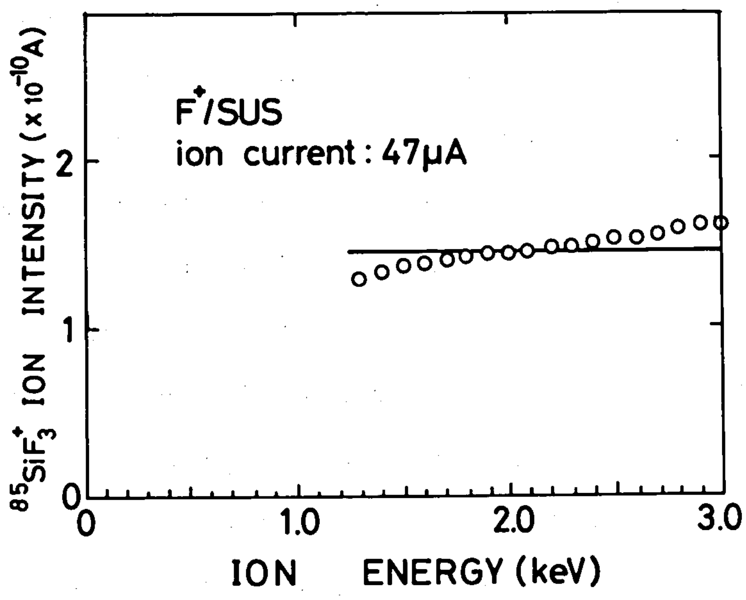

Fig. 4.4 Energy dependence of m/e=85 ion intensity for F^+/SUS ion bombardment.

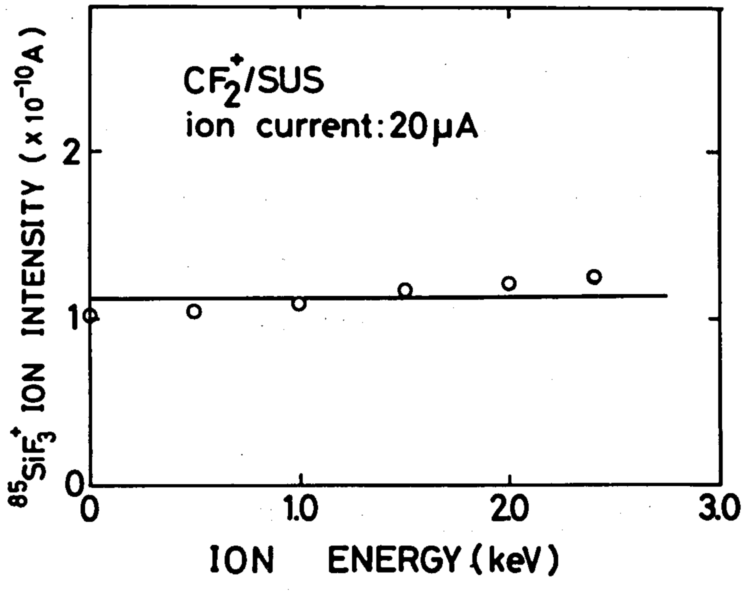

Fig. 4.5 Energy dependence of m/e=85 ion intensity for CF^+/SUS ion bombardment.

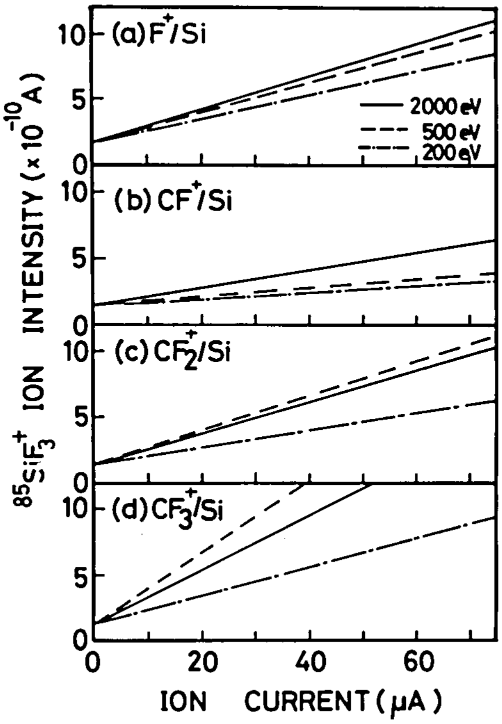

Fig. 4.6 Dependence of $^{85}SiF_3{}^+$ ion intensity on ion current for four types of reactive ions: F^+, CF^+, $CF_2{}^+$, and $CF_3{}^+$. The ion kinetic energy is 1 keV.

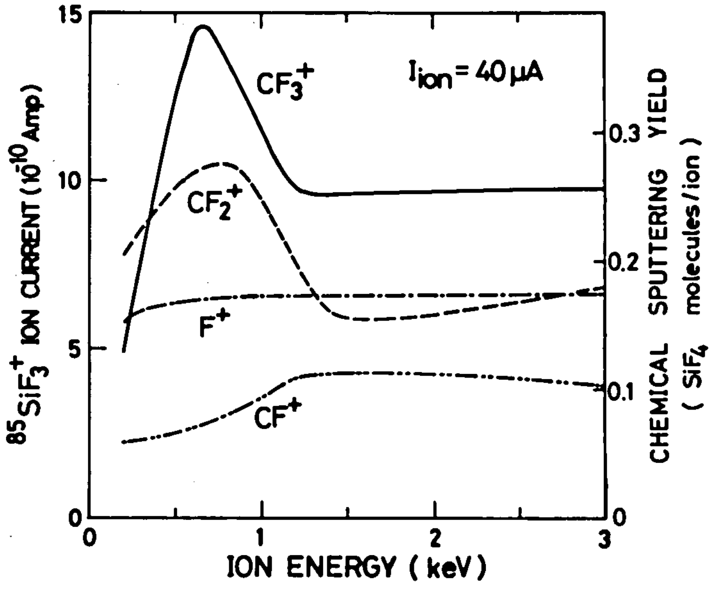

Fig. 4.7 Dependence of $^{85}SiF_3{}^+$ ion intensity on ion kinetic energy for four reactive ions: F^+, CF^+, $CF_2{}^+$, and $CF_3{}^+$. The ion current is 40 μA.

by ion species. By normalizing the $^{85}SiF_3^+$ ion intensity using formula (4.4), Fig. 4.8 can be obtained. Here the arrival rate of fluorine atoms contained in the incoming ion beam is held constant by changing the ion current: F^+(90 μA), CF^+(90 μA), CF_2^+(45 μA) and CF_3^+(30 μA). It should be noted that the probability, ε , of four fluorine atoms reacting with one silicon atom is in the order of 10^{-1} for these fluorine and fluorocarbon ion bombardments.

With fluorine ion irradiation (F^+/Si), the reaction probability increases monotonically as the ion energy increases to 1 keV and then saturates at a value of 0.7. With fluorocarbon ion irradiation (CF_n^+/Si), peak values are obtained well below 1500 eV. The energy level at which this maximum yield occurs shifts towards the low energy side with an increase in the n value: 1200 eV for CF^+, 800 eV for CF_2^+, and 700 eV for CF_3^+. In the energy range above 1.5 keV, the yields saturate at around the same value (0.34) for the three fluorocarbon ion species. Furthermore, this value is close to half that for fluorine ion bombardment (F^+/Si).

The energy dependence of the $^{85}SiF_3^+$ ion intensity for BF_2^+ ion bombardment on a silicon surface is given in Fig. 4.9. It can be seen that the energy dependence for BF_2^+/Si bombardment is quite different from that of CF_n^+/Si (n=1,2,3) ion bombardment. It behaves more like that of F^+/Si.

(d) XPS Analysis

Silicon surfaces bombarded by F^+ or CF_2^+ ions at a kinetic

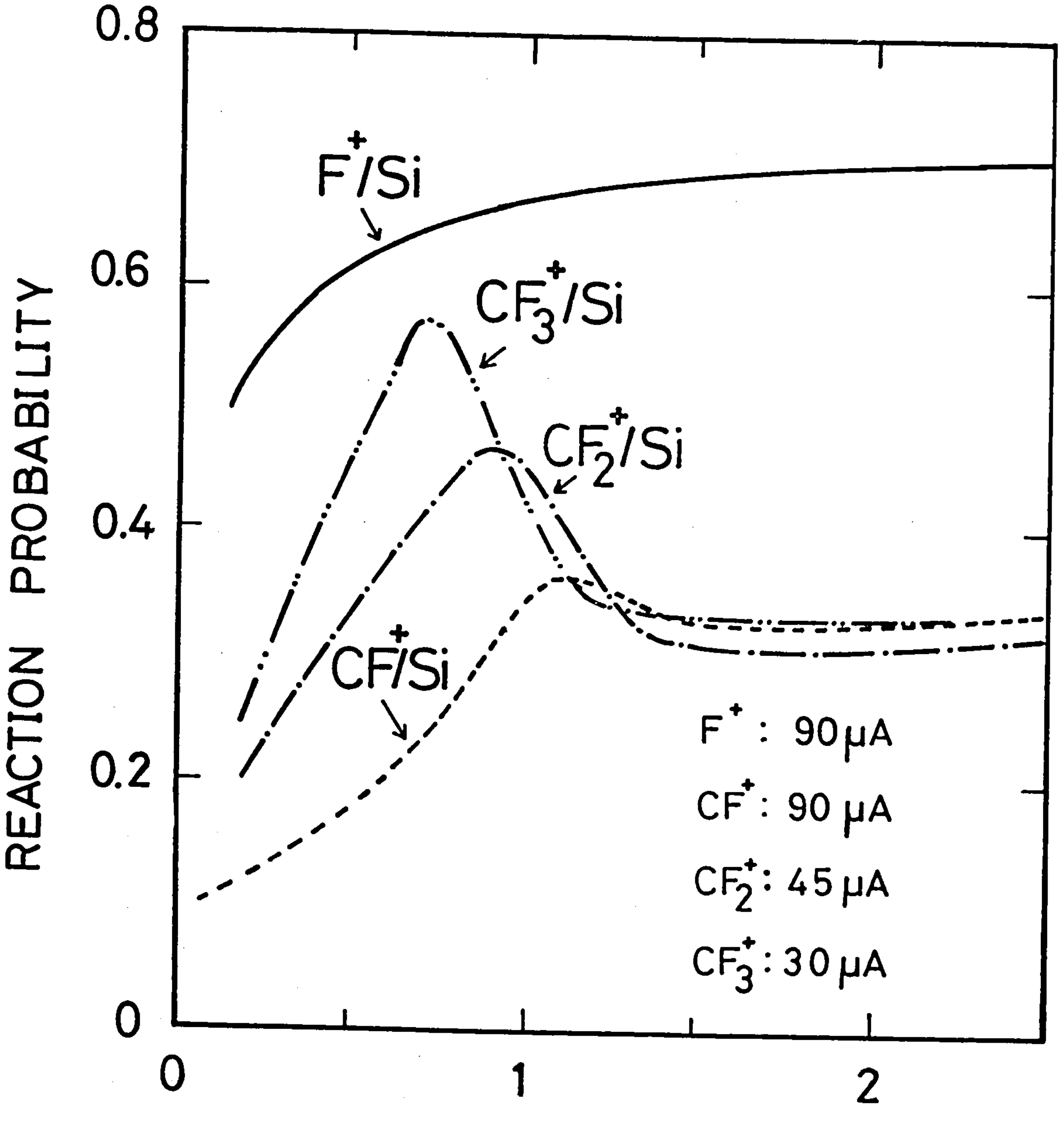

Fig. 4.8 Energy dependence of the etching probability of silicon resulting from reactive ion bombardment with F^+, CF^+, $CF_2{}^+$ and $CF_3{}^+$.

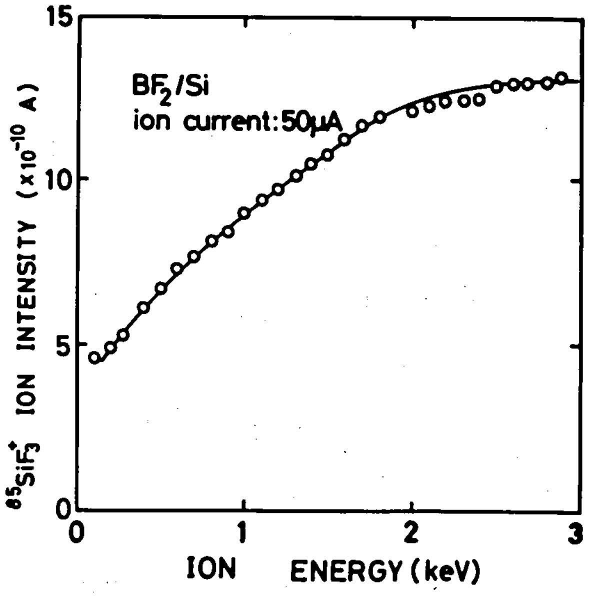

Fig. 4.9 Energy dependence of $^{85}SiF_3^+$ ion intensity for BF_2^+/Si ion bombardment.

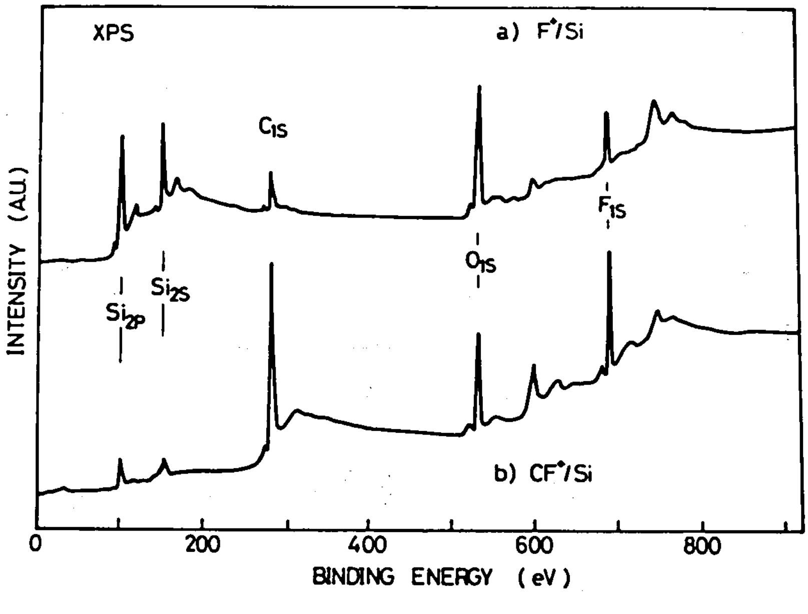

Fig. 4.10 XPS spectra for a silicon surface bombarded by (a) F^+ and (b) CF^+ ions. The kinetic energy of the ion beam is 3 keV.

energy of 1 keV and doses of over 10^{18} ions/cm^2 were analysed by XPS. The results are shown in Fig. 4.10. Although a small amount of carbon contamination is observed for the F^+ ion bombarded silicon surface, a distinct increase in the C_{1s} peak intensity and a decrease in the Si_{2p} and Si_{2s} peak intensities are observed for CF^+ ion bombarded silicon surfaces compared with the F^+ ion bombarded surfaces. This indicates that the silicon surface etched by CF^+ ions is covered with carbon or carboneous polymer film whereas F^+ ion bombardment does not cause such a phenomenon.

4.2.5 Discussion

There have been several reports on the energy dependence of the etching rate for Si and SiO_2 under non-mass-analysed reactive ion beam bombardments, for example, those by Coburn[5], Horiike[4], and Harper[13]. However, their experimental results did not clearly show the pure chemical roles of reactive ion bombardment because of several experimental difficulties. Also, some neutral radicals might have been involved in the etching reactions. The ion current density on an etched surface is subject to the ion extraction energy because of direct extraction[4]. Thus, physical sputtering effects are always mixed with chemical ones. On the other hand, in the present study, the pure chemical nature of reactive ion beam bombardments can be clearly shown using mass-spectroscopic analysis in the mass-separated ion beam system.

The etching experiments for F^+/Si are thought to be the most idealized, since no carbon atoms are transported to the silicon surface by ion bombardment. The energy dependence of the chemical sputtering yields for F^+/Si shown in Figs. 4.8 and 4.9 indicate that etching reactions are apparently enhanced by ion bombardment in the energy range from 100 to 1000 eV. At energy levels above 1000 eV, these enhancement effects remain at a constant level.

The linear dependence of $^{85}SiF_3^+$ ion intensity on ion current shown in Fig. 4.6 indicates that the effect of substrate temperature rise due to ion bombardment is negligible and that the total amount of SiF_4 removed is limited by the incident ion flux.

In the energy range under discussion, physical sputtering occurs simultaneously with ion implantation[14]. Since the penetration depth of F^+ ions at a kinetic energy of 100 - 1000 eV is thought to be in the order of tens of angstroms, the ion implanted layer is steadily sputtered away by subsequent ion bombardment. This complicated removal of the ion implanted region by etching reactions which are enhanced by the enhanced migration effects of fluorine atoms, and the damaged layer formation, might be the reason for the increase in etching probability in the low energy range.

In the higher energy range, the F^+ ions are thought to penetrate deep into the silicon matrix. Therefore, it is possible that the diffusion of fluorine atoms from the implanted layer to the surface layer might determine the etching reaction probability under constant current conditions.

For CF_n^+/Si ion bombardment, the deposition of carbon atoms on the silicon surface has to be taken into account. Incident CF_n^+ ions are thought to undergo charge-neutralization and collisional dissociation with one carbon atom and n fluorine atoms on the silicon surface[15]. In the high ion energy range, these fragmented atoms are thought to be implanted in the silicon lattice resulting in a mixed surface layer of Si, C and F atoms. At steady state, the reaction probability for CF_n^+/Si is independent of the number of fluorine atoms contained in the CF_n^+ ions. Moreover, the value is nearly half of that for F^+/Si. These facts suggest that the deposited fluorine atoms are dissipated to react with the deposited carbon atoms at about the same probability as that for silicon. Of course, the carbon removal effects caused by physical sputtering are thought to have great effect on the removal of deposited carbon.

In the lower energy range, the reaction probability exhibits the very strange energy dependence shown in Fig. 4.8. Even "resonant-type chemical reaction mechanisms" between fragmented atoms and silicon atoms cannot explain these phenomena because the energy at which the yield shows maximum shifts to the low energy side with an increase in the incident ion mass. This contradicts the fact that "resonant-type reactions" should occur at the same kinetic energy as for fragmented atoms from CF_n^+ ions.

According to the recent results of total sputtering yields for silicon under CF^+ and CF_2^+ ion bombardment measured using a quartz microbalance, deposition of some caboneous film has been found in the low energy region[16], whereas the mass-spectroscopic analysis described here proves the appearance of the product gas SiF_4. These facts indicate that the deposited carboneous layers are constantly broken off by physical sputtering.

The etching probablity for silicon by BF_2^+ ion bombardment as shown in Fig. 4.9 exhibits an energy dependence quite different from that for CF_n^+/Si, and is similar to that for

F^+/Si. The different nature of Si-B and Si-C chemical bonding on a silicon surface might be the reason for these phenomena. Further investigation of other types of reactive ions generated from BF_3, SF_6, and PF_5 plasmas are being undertaken.

4.2.6 Conclusions

The energy dependence of chemical sputtering yields for crystalline silicon produced by reactive ion bombardment was investigated using a "low-energy, mass-separated reactive ion beam etching system".

The yields were found to be in the order of 10^{-1} using "mass-spectroscopic analysis" with a quadrupole mass filter. This value is much larger than the reported etching probability for both thermal neutral fluorine atoms with silicon dioxide and fluorine molecules with silicon.

The energy dependences of the yields are quite different for F^+/Si and for CF_n^+(n=1,2,3)/Si. In the former, the yield increases with ion energy up to 1000 eV and then shows a plateau. In the latter cases, maximum values are observed in the energy levels between about 700 to 1500 eV.

These complex energy dependences for fluorocarbon ion beam bombardment may be attributed to the concurrence of carbon deposition and scavenging by physical sputtering as well as to enhanced chemical reaction of the deposited carbon atoms with fluorine atoms.

4.3 Chemical and Physical Roles of Individual Reactive Ions in Si Dry Etching

4.3.1 The Quartz Crystal Oscillator Microbalance Method

The ion beam apparatus used in this measurement is the same as described in Section 4.2. Fig. 4.11 shows the quartz crystal oscillator microbalance (QCOM) arrangement used in this study.

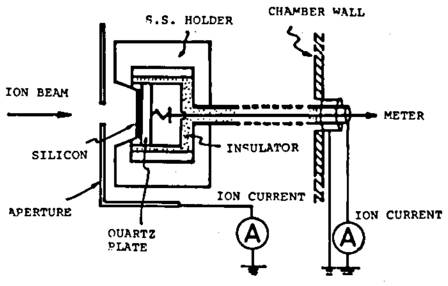

Fig. 4.11 Quartz crystal oscillator microbalance(QCOM).

The decelerated F^+ ion beam was irradiated at an energy of 100 to 3000 eV just in front of the QCOM which was located at the center of the reaction chamber. The QCOM on which Si films were deposited was almost the same as the one commonly used for film thickness monitoring, except for its holding system. The reaction chamber was pumped out to a pressure in the range of 10^{-8}Pa (10^{-10} Torr) and the ambient pressure during ion beam etching was typically 5.3 x10^{-6} Pa (4 x 10^{-8} Torr). The ion current obtained was usually 30 μA. It was necessary, for simultaneous determination of the incident ion current and the resonant frequency, to electrically isolate both the QCOM and its controller from ground level.

Silicon films with thicknesses of up to 2 μm was deposited on quartz crystal discs in another vacuum chamber by electron beam evaporation at a pressure of 2.7 x 10^{-5} Pa (2 x 10^{-7} Torr).

The incident flux of the residual neutral species was calculated from the pressure to be about 2 x 10^{13} (molecules/cm^2 sec). The incident ion flux was 3.7 x 10^{14} (ions/cm^2 sec) at an ion current density of 60 μA/cm^2. This situation differs greatly from that reported by Coburn[6-8]. Moreover, the amount of reactive neutral atoms was found to be one order smaller than for that of an inactive gas. Therefore, the effects of radical species dissociatively generated by ion bombardment on the present measurements could be ignored for first order approxiamtion.

4.3.2 Comparison of the total sputtering yield for F^+/Si and Ne^+/Si.

It was found in the present ion beam etching that the resonant QCOM frequency increased linearly as a function of ion bombardment time under constant ion energy and current conditions. This allowed the influence of QCOM temperature rise attributable to ion bombardment to be disregarded. The resonant QCOM frequency was calibrated by measuring the thickness of the Si films with a conventional Taly-step thickness monitor. With the present apparatus(ANELVA, #983-7109), the total sputtering yield, Y_T, was found to be expressed by the following equation: $Y_T = 0.60 \times \Delta f/I_{ion}$, where I_{ion} is the incoming ion current in μA, and Δf denotes the amountof QCOM frequency shift per one minute(Hz/min).

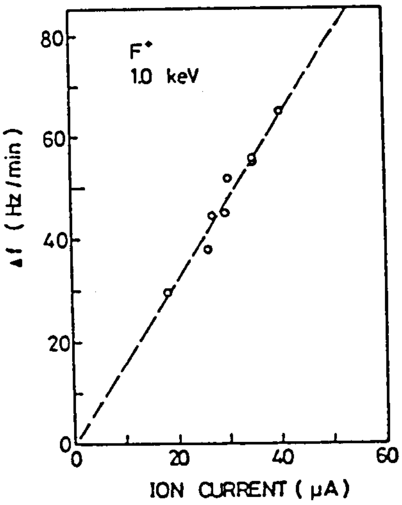

Fig. 4.12 Incident ion current dependence of resonant frequency shift in QCOM during one minute obtained from Si etching by 1 keV F^+ ions.

Frequency shift, Δf, during F' ion irradiation is shown in Fig. 4.12 as a function of the incident ion current with an ion energy of 1000 eV. Since Δf has a linear relationship with ion current, the total sputtering yield can be calculated from the slope of the solid line in Fig. 4.12. The resulting value is 0.96.

The incident ion energy dependence of sputtering yield on F^+ ion bombardment is shown as a solid curve in Fig. 4.13. The sputtering yield for Ne^+ ion bombardment was also measured and is shown as a dotted line in the same figure. The energy dependence of the physical sputtering yield, Y_P, of Si from Ne^+ bombardment was theoretically discussed by Matsunami et al.[17], using a modified Sigmund equation[18]. The present result is in good agreement with the theoreticaly fitted curve.

Though the shapes of both lines in Fig. 4.13. resemble each other, the yield for $^{19}F^+$ ions surpass that for $^{20}Ne^+$ over the whole energy range measured. This result indicates that F^+ ion sputtering involves a yield due to chemical sputtering, Y_C, in addition to Y_P, whereas the sputtering yield of Ne^+ simply involves physical sputtering. This is reasonable because Ne^+ ions are chemically inactive, and the mass difference between $^{20}Ne^+$ and $^{19}F^+$ is small. Therefore, the sputtering yield for F^+ can be expressed by the sum of Y_P and Y_C for first order approximation. The energy dependence of the Y_C for Si under F^+ ion bombardment can be obtained by comparing the Y_T for F^+ to that for Ne^+ in Fig. 4.13. Thus, the Y_C was found to vary from 0.08 to 0.15 in conjunction with an incident ion energy variation of 100 - 3000 eV.

It should be noted that this energy dependence of Y_C agrees well with the chemical reaction probability for F^+ ion derived from mass spectroscopic analysis of the reaction products. (see Section 4.2.) Thus, it can be concluded that the present method is useful in separately determining the Y_C and the Y_P.

Furthermore, it noteworthy that, in the present study, a ratio of chemical sputtering yield to the physical yield was present over the energy region measured. This is shown in Fig. 4.14. The fact that the ratio for a low-energy, such as 100 eV, is about 1.0, and that at 1000 eV is 0.15 shows the importance of chemical sputtering in the low-energy region. This is attributed to the drastic decrease of the Y_P in the low-energy region. Since the physical sputtering yield does not generally change very much from one material to another, it may be that large-selective-etching with a directional etching profile is possible using low-energy, ion bombardment etching.

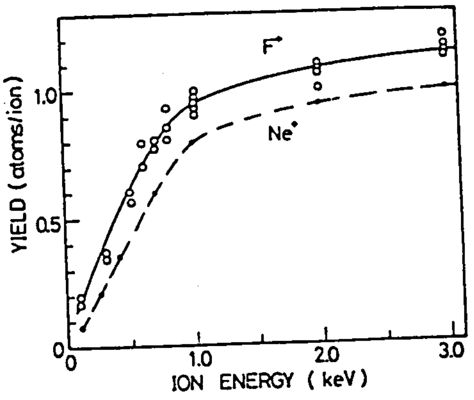

Fig. 4.13 Total sputtering yield for F^+ ion (solid line), and physical sputtering yield for Ne^+ ions (dotted line) obtained as a function of incoming ion energy.

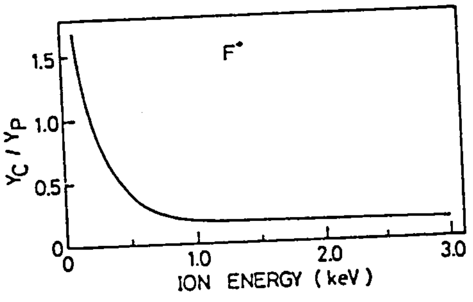

Fig. 4.14 Ratio of chemical to physical sputtering yields derived from the curves in Fig. 4.13.

4.3.4 Total Sputtering Yield of Si from CF_n^+(n=1,2,3) and C^+ Ion Bombardment.

(a) CF^+/Si etching

The total sputtering yield of Si for CF^+ ion bombardment is shown in Fig. 4.15 as a function of the incident ion energy (solid curve). For reference, the chemical sputtering yield, Y_C, obtained from mass-sepectroscopic analysis is shown as a broken line.

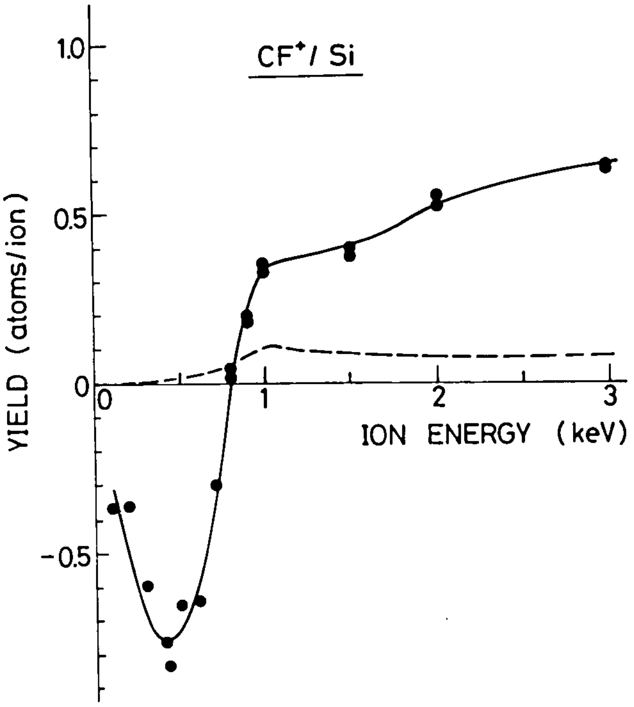

Fig. 4.15 Incident ion energy dependence of the total sputtering yield for Si resulting from CF^+ ion bombardment.

The QCOM results show that Si etching is possible in the energy region from 800 to 3000 eV. However, in the energy region from 100 to 700 eV, carbon or carboneous polymer film deposition took place. The deposition efficiency, Y_d, which is defined here to obtain an absolute value of the QCOM yield, was calculated by assuming the deposited material to be carbon atoms only. As shown in Fig. 4.15, Y_d reaches a maximum in the 400 to 600 eV region with a yield value of 0.7 to 0.8. This value indicates that a large part of the incoming CF^+ ions are dissociatively incorporated as carbon atoms on the Si surface.

In the 600 to 1000 eV region, the situation changes rapidly from deposition to etching and gives a yield from - 0.7 to 0.3. This suggests that energetic (higher than 600 eV) ions can effectively scavenge deposited carbon atoms from the Si surface. The small increase in Y_T beyond 1000 eV can be interpreted as being due to the increase in conventional physical sputtering yield. Although the energy dependence of Y_d in the energy region of 400 to 3000 eV can be explained qualitatively in this way, the decrease in Y_d corresponding to the energy reduction in the energy region below 400 eV cannot be explained in terms of conventional sputtering effects.

(b) CF_2^+/Si etching

Fig. 4.16 shows silmilar measurements for CF_2^+ ions. The Y_T increases monotonically in the 300 - 3000 eV region, but is nearly zero at any energy less than 200 eV. As for the Y_C

values, in the 1500 - 3000 eV region they are almost constant at 0.23. From a comparison of Y_T with Y_C, Y_P was found to be equal to Y_C at an energy of 300 to 400 eV.

It should be noted that deposition was also observed in the 100 to 200 eV region for CF_2^+. Compared with CF^+, it was found that the depositing energy range and deposition efficiency for CF^+ are smaller. Therefore, increasing the fluorine to carbon atom ratio of the incoming fluorocarbon ions is considered to be an effective way to scavenge deposited carbon atoms from the Si surface.

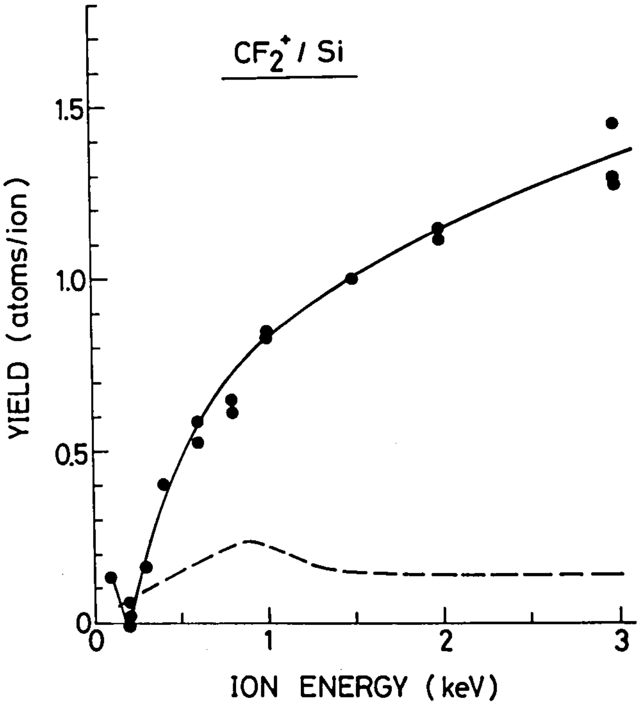

Fig. 4.16 Incident ion energy dependence of the total sputtering yield for Si resulting from CF_2^+ ion bombardment.

(c) CF_3^+/Si etching

For CF_3^+ ion bombardment, no film deposition was observed over the whole energy region measured. Fig. 4.17 shows the incident ion energy dependences of Y_T (solid curve) and Y_C (broken line) resulting from CF_3^+ bombardment. The value of Y_T was found to be larger than for CF_n^+(n=1,2,3) or F^+ ions.

(d) C^+ ion beam deposition onto Si

Carbon deposition on the Si surface was observed for C^+ ion bombardment in the 100 to 2500 eV region. It should be noted that only deposition took place in this case. The energy dependence of Y_d is shown in Fig. 4.18. It was found that the maximum Y_d value was 0.8 - 0.9 in the 600 to 800 eV region and decreased as the energy increased in the 900 to 2500 eV region. Thus, it appears that a large part of the incident C^+ ions at 600 to 800 eV are deposited or implanted onto the Si. The decrease in Y_d in the higher energy region could be due to the increase in C^+ self-sputtering effect. However, the Y_d decrease in the 100 to 600 eV region cannot be explained by conventional sputtering theory, which is the same as for CF^+. It could be speculated that the effective sticking probabilities of incident cabon ions decreases in correspondance to the decrease in ion implantation effects in the low energy region.

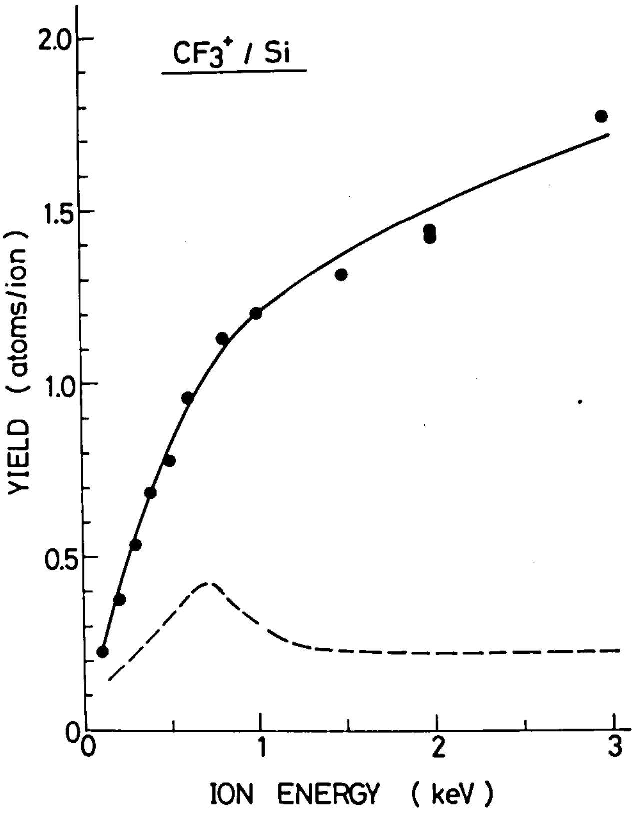

Fig. 4.17 Incident ion energy dependence of the total sputtering yield for Si resulting from CF_3^+ ion bombardment.

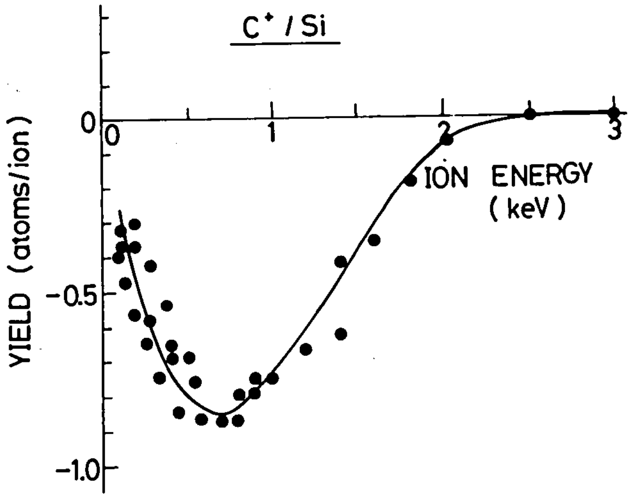

Fig. 4.18 Incident ion energy dependence of carbon atom condensation probability for C^+ ion beam deposition on a Si surface.

(e) F^+/C etching

In the experiments described above, carbon and carboneous polymer deposition onto the Si surface was observed for C^+, CF^+, and $CF_2{}^+$ ion bombardments. Therefore, carbon etching by such reactive species as F atoms might take place simultaneously in conventional Si dry etching with a CF_4 gas plasma. Thus, it would seem necessary to show sputtering yields for carbon resulting from reactive ion bombardment.

Fig. 4.19 shows the energy dependence of Y_T for C resulting from such F^+ ion bombardment. The carbon films were deposited on quartz discs by conventional arc-discharge evaporation or the IBD method described in Chapter 3. It can be seen in that figure that Y_T is less than 1.0 at any ion energy below 700 eV.

As for CF^+, the same number of C and F hits the Si surface. A large number of the incident carbon atoms are deposited on, or implanted into, the Si surface, as is shown in Fig. 4.15. Hence, for CF^+ ion beam etching, the accumulated carbon atoms were scavenged by the simultaneously incident fluorine atoms, the amount of scavenging being equal to that of carbon deposition. Therefore, carbon acculmulation continues during CF^+ ion beam etching, since Y_T for F^+/C is smaller than 1.0.

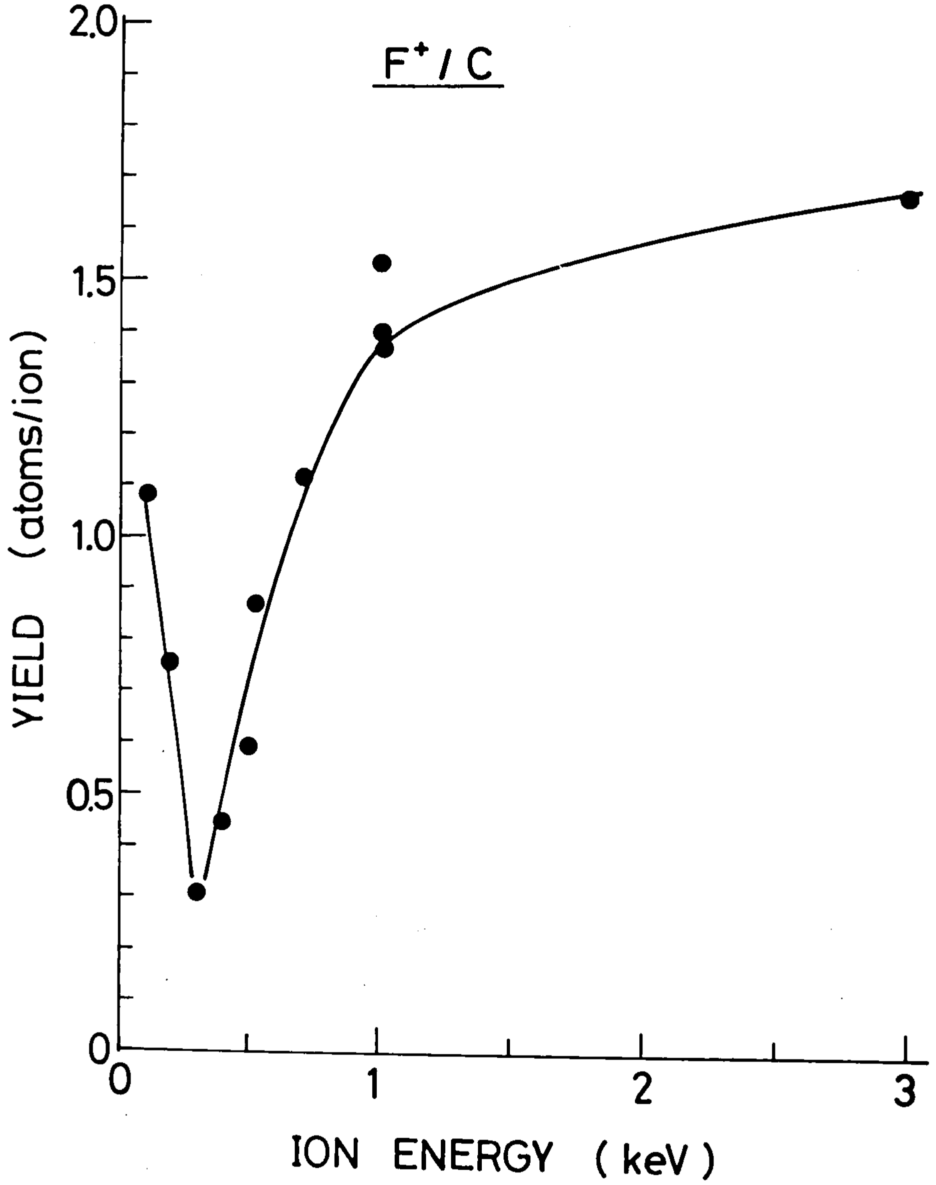

Fig. 4.19 Incident ion energy dependence of the total sputtering yield of carbon resulting from F^+ ion bombardment.

4.4 Summary

The mechanisms of reactive ion beam etching (RIBE) of silicon were investigated using a mass-separated reactive ion beam ething apparatus. Chemical sputtering yields of silicon under F^+ and CF_n^+(n=1,2,3) ion bombardments were found by mass-spectroscopic analysis. The yield was in the order of 10^{-1} and depended strongly on the ion species and their energies. For F^+ ion bombardment, it was shown that an increase in energy up to 1 keV enhances the etching reactions. However, for CF_n^+ ion bombardment, the inclusion of carbon atoms with the impinging ions makes the situation quite difficult to understand within conventional theory.

The relative contribution of physical sputtering and chemical one in RIBE was also investigated using quartz oscillator microbalance. It was shown that the contribution from physical sputtering dominates at ion energies above 1 keV. In the energy range below 1 keV, deposition of carbon atoms on a silicon surface retards etching for CF_n^+ ion bombardment.

Further investigation is necessary to understand these physicochemical effects of ion bombardment on etching reactions.

Chapter 5 CONCLUDING REMARKS

The effects of low-energy ion bombardment on film formation and reactive ion etching were investigated using a low-energy, mass-separated ion beam accelerator specially developed for this study.

In Chapter 1, a historical background of this study was given and the purpose of the study was described.

Chapter 2 was devoted to the discussion on the design and the development of the low-energy, mass-separated ion beam accelerator. Production of a high-intensity metal ion beam, transport of that under fully space-charge neutralization, and formation of low-energy ion beams using crossed-electromagnetic field were successfully utilized in the accelerator.

Investigation of relatively low-temperature epitaxial growth by ion beam deposition was discussed in detail in Chapter 3. It was shown that silicon and germanium films can be epitaxially grown on Si(100) singly crystalline substrates at an ion energy of 100 to 200 eV and substrate temperatures of 740° C for Si and 300° C for Ge. It was also pointed out that the thick interface layer formation due to ion induced atomix mixing is one reason why strongly adherent can be formed by ion/plasma process film formation methods.

The mechanism for reactive ion beam etching of silicon was investigated using the same apparatus. Both mass-spectroscopic and quartz microbalance methods were investigated to do quantitative discussions on individual etching characteristics of various reactive ions. Ion bombardment effects were also discussed in detail.

Some of the surface physical/chemical effects of ion bombardment have been determined in this thesis. However, further efforts involving construction of theoretical models will be necessary in order not only to understand these complicated surface chemical reactions but also to utilize them to reliable industrial applications.

REFERENCES

Chapter 1

1) T. Tokuyama, K. Yagi, K. Miyake, M. Tamura, N. Natsuaki and S. Tachi: Nucl. Instr. Meth. 182/183, Part I(1981)241

2) T.Takagi, K, Matsubara, H. Takaoka and I. Yamada: Proc. Int. Conf. on Ion Plating and Allied Techniques(IPAT'79), London

3) For example, Thin Film Processes, ed. by J.L. Vossen and W. Kern (Academic Press, New York, 1978)

4) T. Itoh, T. Nakamura, M. Muromachi and T. Sugiyama: Jpn. J. Appl. Phys.,16(1977)553

5) Y. Murayama: J. Vac. Sci. Technol., 12(1975)876

6) E.H. Hirsch and I.K. Varga: Thin Solid Films, 52(1978)445

7) D.M. Mattox: J. Vac. Sci. Technol., 10(1973)47

8) H.G. Hughes and M.J. Rand, ed., Etching (The Electrochemical Society, 1976)

9) Y. Horiike, PhD thesis (Waseda University, 1980)

10) R.G. Frieser and C.J. Mogab, ed., Plasma Processing (The Electrochemical Society, 1980)

Chapter 2

1) E. Lindholm: Proc. Phys. Soc. A66(1953)1068

2) A. Fontell and E. Arminen: Ann. Acad. Sci. Fennicae,Ser. A, VI No. 244(1967)

3) K. Chida, K. Kaneko and M. Sakai: Mass Spectroscopy, 14(1969)149

4) T. Tortschanoff and F.P. Viehbock: Proc. of the Int. Conf. on Electromagnetic Isotope Separators and the Techniques of their Applications, Marburg, Sept. 7-10(1970), BMBW-FB K 70-28, p.482

5) K. Yagi, S. Tamura and T. Tokuyama: Jpn. J. Appl. Phys.,

16(1977)245

6) J.H. Freeman, W. Temple, D. Beanland and G.A. Gard: Nucl. Instr. and Meth. 135(1976)1

7) K. Miyake, S. Tamura and K. Yagi: The Professional Group of Electron Devices of IEEJ, EDD-76-30, Tokyo(1976)

8) J. Amano, P. Brice and R.P.W. Lawson: J. Vac. Sci. Technol., 13(1976)591

9) J.S. Colligon, W.A. Grant, J.S. Williams and R.P.W. Lawson: Proc. Int. Conf. on Applicaions of Ion Beams to Metals, Univ. of Warwick, 1975(Inst. Phys. Conf. Ser. No. 28,(1976) p.357

10) T. Tsukizoe, T. Nakai and N. Ohmae: J. Appl. Phys., 48(1977)4770

11) G.E. Thomas and E.E. de Kluizenaar: Proc. 3rd. Int. Congr. on Surface Physics and Chemistry, Grenoble, 1977(Societe Francaise du Vide, Paris,1977) p.136

12) T. Takagi: Proc. of Int. Workshop by Professional Group on Ion-Based Techniques for Film Formation, June 1st-5th(1981) Tokyo(The Inst. Electr. Eng. of Japan) p.449

13) Jahnke, Emde, and Losch: Tables of Higher Function, (6th ed., Dover)

14) M.D. Gabovich, I.A. Soloshenko and A.A. Ovcharenko: Ukr. Fiz. Zh. 16(1971)812

15) R. Bernars: Le J. de Physique et le Radium, 15(1954)273

16) J.H. Freeman, Nucl. Instrum. Meth.,22(1963)306

17) A.W. Hull, Phys. Rev.,25(1925)645

18) B. Cobic, D. Tosic and B. Perovic, Nucl. Instrum. Meth. 24(1963)358

19) H. Hinkel, Nucl. Instrum. Meth., 139(1976)1

20) O. Tsukakoshi, T. Narusawa, M. Mizuno, K. Sone, H. Ohtsuka and S. Komiya: JAERI-M 6331(1975)

21) T. Tokuyama, K. Yagi, K. Miyake, M. Tamura, N. Natsuaki and S. Tachi: Nucl. Instr. and Meth., 182/183, Part I (1981)241

22) B. Elbek, M.C. Olesen and O. Skilbreid: Nuclear Physics, 10(1959)294

23) I. Bergstrom, F. Brown, J.A. Davis, J.S. Geiger, R.L. Graham and R. Kelly: Nucl. Instr. and Meth. 21(1963)249

24) J. Uhler: Arkiv for Fysik, 24(1963)349

25) B.A. Probyn: Brit. J. Appl. Phys.(J. phys. D) Ser. 2, Vol. 1 (1968)457

26) J.S. Dionisio and D.X. de Lima: Nucl. Instr. and Meth. 61(1968)260

27) J. Geerk and O. Meyer: Surface Sci.,32(1972)222

28) G.D. Alton, J.B. Roberto, C.W. White and R.A. Zuhr: Nucl. Instr. and Meth. 177(1980)273

29) S.C. Brown: Basic Data of Plasma Physics, 2nd. ed., (The MIT Press, 1966) pp.47-77

30) K. Kaneko: private communication

Chapter 3

1) T. Tokuyama, K. Yagi, K. Miyake, M. Tamura, N. Natsuaki and S. Tachi: Nucl. Instr. Meth. 182/183, Part I(1981)241

2) K. Miyake, K. Yagi and T. Tokuyama: Ohyo Butsuri, 48(1979)883

3) T.Takagi, K, Matsubara, H. Takaoka and I. Yamada: Proc. Int. Conf. on Ion Plating and Allied Techniques(IPAT'79), London

4) J.M.E. Harper: in Thin Film Processes, ed. by J.L. Vossen and W. Kern (Academic Press, New York, 1978) Chap. II-5, p. 175

5) W.E. Flynt: Proc. of 3rd Symp. on Electron Beam Technology, p.368-379(1961)

6) A.R. Wolter: Proc. 4th Microelectronics Symposium (1965) 2A-1

7) B.A. Probyn: Brit. J. Appl. Phys. (J. Phys. D) Ser. 2, Vol. 1(1968)457

8) S. Aisenberg and R. Chabot: J. Appl. Phys. 42(1971)2953

9) E.G.Spencer,P,H,Schmidt, D.C.Joy and F.L. Sansalone: Appl. Phys. Letts. 29(1976)118

11) J.S. Colligon, W.A. Grant, J.S. Williamns and R.P.W. Lawson: Proc. Int. Conf. Appl. of Ion Beams to Metals, Univ. of Warwick, 1975, Inst. Phys. Conf. Ser. No. 28 (1961) Chap. 9, p. 357

12) K. Miyake, S. Tamura and K. Yagi: The Professional Group of Electron Devices of IEEJ, EDD-76-30, Tokyo(1976)

13) J.H. Freeman, W. Temple, D. Beanland and G.A. Gard: Nucl. Instrum. and Methods 135(1976)1

14) J.H. Freeman: Nature 275(1978)634

15) J. Amano, P. Brice and R.P.W. Lawson: J. Vac. Sci. Technol. 13(1976)591

16) J. Amano and R.P.W. Lawson: J. Vac. Sci. Technol., 14(1977)690

17) J. Amano and R.P.W. Lawson: ibid., 14(1977)695

18) J. Amano and R.P.W. Lawson: ibid., 15(1978)113

19) G.E. Thomas and E.E. de Kluizenaar: Proc. 3rd Int. Congr. Surf. Phys. and Chem., Grenoble,1977(Societe Francaise du Vide, Paris,1977) p.136

20) K. Yagi, S. Tamura and T. Tokuyama: Jpn. J. Appl. Phys.,16 (1977)245

21) K. Yagi, K. Miyake and T. Tokuyama: Proc. Int. Conf. on Low Energy Ion Beams, Salford 1977, Inst. Phys. Conf. Ser. No.38(1978) Chap. 2, p.78

22) K. Miyake and T. Tokuyama: to be published in Thin Solid Films

23) T. Tsukizoe, T. Nakai and N. Ohmae: J. Appl. Phys. 48(1977)4770

24) T. Itoh, T. Nakamura, M. Muromachi and T. Sugiyama: Jpn. J. Appl. Phys.,16(1977)553

25) S. Shimizu and S. Komiya: J. Vac. Sci. Technol. 17(1980)498

26) T. Takagi, I. Yamada and A. Sasaki: Thin Solid Films 45(1975)569

27) P. Sigmund: Phys. Rev. 184(1969)383

28) A. Fontell and E. Arminen: Can. J. Phys. 47(1969)2405

29) I. Yamada, F.W. Saris, T. Takagi, K. Matsubara, H. Takaoka and S. Ishiyama: Jpn. J. Appl. Phys. 19(1980) L181-184

30) D.G. Teer and B.L. Delcea: Thin Solid Films 54(1978)295

31) D.M. Mattox: J. Appl. Phys. 34(1963)2493

32) T. Tsuchimoto: J. Vac. Sci. Technol. 15(1978)70

33) T. Tsuchimoto: J. Vac. Sci. Technol. 15(1978)1730

34) T. Tsuchimoto: J. Vac. Sci. Technol. 17(1980)1336

35) A.E.T. Kuiper, G.E. Thomas and W.J. Schouten: J. of Crystal Growth, 51(1981)17

36) A.G. Cullis and G.R. Booker: J. of Crystal Growth, 9(1971)112

37) K. Itoh and K. Takahashi: Jpn. J. Appl. Phys.,7(1968)821

Chapter 4

1) J.A. Bondur: J. of Electrochem. Soc., 126,226(1979)

2) K. Suzuki, S. Okudaira and I. Kanomata: J. of Electrochem. Soc.,126,1024(1979)

3) R.H. Bruce: Electrochemical Society Meeting, St. Louis, MO, May (1980) p.243

4) Y. Horiike, M. Shibagaki and K. Kadono: Jpn. J. Appl. Phys. Phys., 18(1979) 2309-2310

5) J.W. Coburn, H.F. Winters.,and T.J. Chuang: J. Appl. Phys., 48,3532(1977)

6) J.W. Coburn and H.F. Winters: J. Appl. Phys., 50,3189(1979)

7) Yung-Yi Tu: Proc. of the Symposium on Sputtering, Perchfoldsdorf, Vienna, Austria(1980) April 28-30, ed. by P. Varga, G. Betz and F.P. Viehbock, p.337

8) M. Chen, V.J. Minkiewicz, and K. Lee: J. of Electrochem. Soc., 126,1946(1979)

9) D.L. Flamm, C.J. Mogab and E.R. Sklaver: J. Appl. Phys., 49,3796(1978)

49,3796(1978)

10) R.G. Frieser and C.J. Mogab, ed., Plasma Prcessing, (The Electrochemical Society, 1980)

11) K. Yagi, K. Miyake and T. Tokuyama: Proc. Int. Conf. on Low Energy Ion Beams, Salford 1977, Inst. Phys. Conf. Ser. No.38(1978) Chap. 2, p.78

12) K. Miyake, K. Yagi and T. Tokuyama: Proc. of the 4th Symp. on Ion Sources and Application Technology, p. 131, June 24th - 26th(1980) Tokyo

13) J.M.E. Harper, J.J. Cuomo, P.A. Leary, G.M. Summa, H.R. Kaufman, and F.J. Bresnock: J. of Electrochem. Soc., 128(1981)1077

14) T. Tokuyama, K. Yagi, K. Miyake, M. Tamura, N. Natsuaki and S. Tachi: Nucl. Instr.and Meth.,182/183(1981) 241-250

15) J.A. Taylor, G.M. Lancaster, A. Ignatiev, and J.W. Rabalais: J. Chem. Phys. 68(1978)1776

16) S. Tachi, K. Miyake and T. Tokuyama: Jpn. J. Appl. Phys. 20(1981) L411-413

17) N. Matsunami, Y. Yamamura, Y. Ichkawa, N. Itoh, S. Miyagawa, K. Morita and R. Shimizu: Energy Dependence of Sputtering Yields of Monoatomic Solids, IPPJ-AM-14, (Institute of Plasma Physics, Nagoya Univ., Nagoya, 1980)

18) P. Sigmund: Phys. Rev. 184(1969)383

LIST OF PUBLICATIONS

1) K. Miyake, K. Yagi and T. Tokuyama: "Discharge characteristics and beam quality of a Freeman-type ion source in low-pressre arc operation: applications to ion beam deposition", Proc. Int. Conf. Low Energy Ion Beams, Salford,1977, Inst. Phys. Conf. Ser. No. 38 (1978) Chap. 2 p.78

2) K. Yagi, K. Miyake and T. Tokuyama: "Low-energy, mass-analysed ion beam deposition", Proc. Int. Conf. Low Energy Ion Beams, Salford,1977, Inst. Phys. Conf. Ser. No. 38 (1978) Chap.3, p. 136

3) K. Miyake, K. Yagi and T. Tokuyama: "New Ion Beam Methods for Thin Film Formation", Ohyo Butsuri, 48(1979) pp. 883 - 889

4) T. Tokuyama, K. Yagi, K. Miyake, M. Tamura, N. Natsuaki and S. Tachi: "Low-energy, mass-analysed ion beam deposition of materials", Nucl. Instrum. Meth. 182/183 Part I(1981) PP. 241 - 250

5) S. Tachi, K. Miyake and T. Tokuyama:"Chemical and physical sputtering yield of silicon", Jpn. J. Appl. Phys. 20(1981) L411 - 413

6) S. Tachi, K. Miyake and T. Tokuyama:"Chemical and physical roles of individual reactive ions in Si dry etching", Proc. of the 13th Conf.on Solid State Devices, 26 Aug.(1981) Tokyo

7) K. Miyake and T. Tokuyama: "Germanium and silicon ion beam deposition", to be published in Thin Solid Films

8) K. Miyake, K. Yagi and T. Tokuyama: "Direct observation of N_2^+ ion beam during deceleration", submitted to Nucl. Instrum. Method

9) K. Miyake, S. Tachi, K. Yagi and T. Tokuyama: "Chemical sputtering yield of silicon by mass-separated reactive ion beam bombardment", submitted to J. Appl. Phys.

LIST OF TECHNICAL REPORTS

1) K. Miyake, S. Tamura and K. Yagi: "Design of a low-energy, mass-separated ion beam deposition system", The Professional group of Electron Devices of IEEJ, Paper No. EDD-76-30, Feb. (1976)Tokyo

2) K. Miyake, K. Yagi and T. Tokuyama: "Production of low-energy, high-current ion beams", Proc. of the Spring Meeting of JSAP Paper No, 29a-F-7, p.484 (1976) Tokyo

3) K. Yagi, K. Miyake, S. Tamura and T. Tokuyama: "Thin film formation by IBD(Ion Beam Deposition)" Proc. of the Fall Meeting of IECEJ, Paper No. CPM76-64 (1976) Fukuoka

4) T. Tokuyama, K. Yagi and K. Miyake: "Thin film formation by IBD(Ion Beam Deposition)" Proc. of the Fall Meeting of IEEJ, p. 3-75 (1976)

5) K. Miyake, N. Natsuaki, K. Yagi and T. Tokuyama: "Ion beam deposition and sputtering", Proc. of the Specialist Meeting of Applications of Heavy Ions to Solid State Physics, pp. 36 - 40, Jan. 26(1977),(Institute of Plasma Physics, Nagoya)

6) K. Miyake, K. Yagi and T. Tokuyama: "Energy dispersion of ion beams in a low-energy ion beam deposition system", Proc. of the Symposium on Ion Sources and Application Technology, p. 103 , Feb. 14-15(1977) Tokyo

7) K. Miyake, K. Yagi and T. Tokuyama: "Ion beam deceleration in an IBD system", Proc. of the Fall Meeting of JSAP, Paper

No. 13a-W-7, p. 373, Oct. 13 - 15(1977)

8) K. Miyake, K. Yagi and T. Tokuyama: "Discharge characteristics of a Freeman-type ion source", Proc. of the Fall Meeting of JSAP, Paper No. 13a-W-8, p. 373. Oct. 13 - 15, (1977)

9) K. Miyake, K. Yagi and T. Tokuyama: "A Modified magnetron-type ion source with a field-compensated filament", Proc. of the 2nd. Symp. on Ion Sources and Application Technology, pp. 49 - 50, Feb. 16 - 17(1978) Tokyo

10) K. Miyake, K. Yagi and T. Tokuyama: "A new magnetron-type ion source with a field-compensated filament", Proc. of the Spring Meeting of JSAP, Paper No. 30a-S-2, p. 303, March 27 - 30(1979)

11) K. Miyake, K. Yagi and T. Tokuyama: "Ion beam deceleration in an IBD system (II)", Proc. of the Spring Meeting of JSAP, Paper No. 1p-N-11, April 1 - 4(1980) Yamanashi

12) K. Miyake, K. Yagi and T. Tokuyama: "Direct observation of a focused N_2^+ ion beam during deceleration", Proc. of the 4th Symp. on Ion Sources and Application Technology, p. 131, June 24th - 26th(1980) Tokyo

13) K. Miyake, S. Tachi, K. Yagi and T. Tokuyama: "Recent studies on the plasma etching mechanism", Proc. of the 4th Symp. on Ion Sources and Application Technology, p. 335, June 24th - 26th(1980) Tokyo

14) K. Miyake, S. Tachi, K. Yagi and T. Tokuyama: "The plasma etching mechanism of silicon (I) --- a low-energy, mass-separated reactive ion beam etching system",

Proc. of the 4th Symp. on Ion Sources and Application Technology, p. 341, June 24th - 26th(1980) Tokyo

15) S. Tachi, K. Miyake, K. Yagi and T. Tokuyama: "The plasma etching mechanism of silicon (II) --- etching probability dependence on ion species (F^+, CF^+, $CF_2{}^+$, $CF_3{}^+$) and ion energies(0 - 3 keV)"
Proc. of the 4th Symp. on Ion Sources and Application Technology, p. 345, June 24th - 26th(1980) Tokyo

16) K. Miyake, S. Tachi and T. Tokuyama: "Plasma chemical reactions in CF_4 plasma in a high temperature ion source", Proc. of the 4th Symp. on Ion Sources and Application Technology, p. 355, June 24th - 26th(1980) Tokyo

17) K. Miyake, S. Tachi, K. Yagi and T. Tokuyama: "The dry etching mechanism of silicon (I)", Proc. of the Fall Meeting of JSAP, Paper 18a-E-6, p. 297, Oct. 17 - 19(1980)

18) S. Tachi, K. Miyake, K. Yagi and T. Tokuyama: "The dry etching mechanism of silicon (II)", Proc. of the Fall Meeting of JSAP, Paper 18a-E-7, p. 298, Oct. 17 - 19(1980)

19) S. Tachi, K. Miyake and T. Tokuyama: "Plasma chemical reactions in CF_4 and C_3F_8 plamsa in a high temperature ion source", Proc. of the Fall Meeting of JSAP,
Paper No. 18a-E-9, p. 299, Oct. 17 - 19(1980)

20) K. Miyake, S. Tachi, K. Yagi and T. Tokuyama: "Etching chemical reactions of silicon surface atoms under reactive ion beam (F^+, $CF_x{}^+$) bombardment", Proc. of the Fall Meeting of ECS in Japan, A107 p. 165, Oct.(1980)

21) K. Miyake and T. Tokuyama: "Material modification and fabrication by ion beam deposition", The Specialist Meeting of Electron Device Materials of IEEJ, Paper No. EFM-80-26, Nov. 28 (1980) Tokyo

22) K. Miyake and T. Tokuyama: "Ion mixing effects in ^{28}Si/Al ion beam deposited films", Proc. of the Spring Meeting of JSAP, Paper No. 31a-E-6, p. 278, March 29 - April 1(1981)

23) S. Tachi, K. Miyake and T. Tokuyama: "The dry etching mechanism of silicon (III)", Proc. of the Spring Meeting of JSAP,Paper No.31a-X-3, p. 348, April(1981) Tokyo

24) K. Miyake and T. Tokuyama: "Germanium and silicon ion beam deposition", Proc. of Int. Workshop by Professional Group on Ion-Based Techniques for Film Formation, pp. 443 - 448, June 1st - 5th(1981) Tokyo

25) S. Tachi, K. Miyake and T. Tokuyama:"The dry etching mechanism of silicon (IV)", Proc. of the Fall Meeting of JSAP, Paper No. 7p-H-11, p. 377, Oct(1981) Fukui

*IEEJ(The Institute of Electrical Engineers of Japan)

*JSAP(The Japan Society of Applied Physics)

*IECEJ(The Institute of Electronics and Communication Engineering of Japna)